

**Light-matter interactions for quantum simulation and  
quantum memory experiments**

by

Anindya Rastogi

A thesis submitted in partial fulfillment of the requirements for the degree of

Master of Science

Department of Physics

University of Alberta

©Anindya Rastogi, 2018

# Abstract

The tools of atomic physics enable researchers to explore rich quantum mechanical phenomena by way of light-matter interactions. In some applications, light is used to manipulate or modify the properties of a material medium, for instance, laser-cooling and optical trapping of neutral atoms and ions; electromagnetically-induced-transparency (EIT); and Bose-Einstein-Condensation (BEC). Likewise, there are applications where matter is used to manipulate the properties of light, as for example, non-linear optical processes; atomic quantum memories; and quantum-information-processing. This thesis explores two routes towards manipulating light using matter and vice versa in our lab. The work presented in this thesis falls under two categories, one is the experimental side where we have designed and built a laser system to cool a thermal gas of  $^{39}\text{K}$  atoms to sub-Doppler temperatures, using the ‘*Gray Molasses*’ technique. This work is motivated by the long-term goal of performing quantum simulation experiments with degenerate quantum gas of K. The second category is on the theoretical (numerical) side, where we introduce a novel quantum memory protocol for coherent storage and processing of broadband light pulses, based on a fundamental physical process in atomic physics, called the ‘*Autler-Townes*’ effect.

Ultracold quantum gases are one of the most versatile systems in the field of cold atom physics; these atomic systems can be experimentally controlled and manipulated with high degree of precision and are thus, widely used to model the behavior of other complex quantum mechanical systems. Laser-cooling is the first and indeed a crucial stage towards creating an ultracold gas of atoms. In this thesis, we describe an optical setup for producing a laser-cooled and trapped gas of bosonic  $^{39}\text{K}$  atoms, using D1 and D2 atomic transition-lines. The optical setup is built to generate appropriate laser frequencies for implementing various stages of the experiment: red-detuned

two and three-dimensional magneto-optical traps (MOT) on the D2-line; a blue-detuned gray molasses phase on the D1-line; as well as optical pumping, imaging and push beams on the D2-line. We also highlight the underlying physics behind the blue-detuned gray molasses cooling and the advantages it offers in cooling species like K and Li. We also discuss in detail, the techniques used for frequency locking our lasers, namely, saturated absorption spectroscopy (SAS) and beatnote locking.

The second part of the thesis describes a new atomic quantum-memory scheme for storing broadband pulses of light, which we call the ‘Autler-Townes Splitting (ATS)’ protocol. We show the light storage and retrieval operation in three different configurations, via numerical simulation of Maxwell-Bloch equations. We also discuss the strategies for getting high storage and retrieval efficiency in the ATS memory in terms of only two phenomenological parameters, both of which are experimentally accessible. We have shown that a near-unity efficiency is achievable for a wideband signal, under moderate values of atomic density and laser powers; this significantly relaxes the technical requirements of our protocol when compared to other broadband storage schemes.

# Preface

The design of the optical setup (§. 3.2) was conceptualized by Dr. Lindsay LeBlanc and later modified by Logan Cooke and me, under the supervision of Dr. LeBlanc.

The optical-alignment for frequency stabilization of D1 and D2 diode-lasers (§. 3.4) was done by L. Cooke and myself.

An electronic amplifier cum filter circuit (not described in the thesis) for removing excessive pump beam modulations from the saturated-probe spectrum of our D1-laser was built by me. The estimation of correct polarities of the PID-controllers (§. 3.4.1) and optimization of the PID-gains (§. 3.4.2) for frequency locking the D1 and D2-lasers was done by me.

The beat-note locking system (§. 3.5) was originally designed and implemented by Dr. LeBlanc on the Rb-laser setup. On similar lines, a closed-feedback control circuit was assembled and characterized by me for frequency stabilizing the  $^{39}\text{K}$  trap / cooling laser. I am also thankful to Taras Hrushevskiy for helping me troubleshoot this system in the initial stage.

I and Logan worked together on building the optics for exciting various transitions on the D1-D2 lines (§. 3.1 and 3.6) namely, cooling; repump; optical-pumping; push-beam and absorption-imaging. I am thankful to Dr. Erhan Saglamyurek for his guidance that helped a lot in overcoming some of the roadblocks we faced while building the setup.

I performed frequency calculations in §. 3.5, 3.6.1 and 3.6.2 based on discussions with Dr. LeBlanc and L. Cooke.

I designed, constructed and characterized an FPGA-based laser power servo system (§. 3.8) for intensity control of our lasers. I am grateful to Allan Stummer at UofT (retired) for valuable discussions regarding this sub-project.

The idea of a light storage scheme based on Autler-Townes absorption was proposed by Dr. Saglamyurek with feedback from Dr. LeBlanc and Dr. K. Heshami. The experimental demonstration of this storage (not described in this thesis) was performed by Dr. Saglamyurek and T. Hrushevskiy. The initial modeling of the ATS scheme was done by Dr. Heshami with inputs from Dr. Saglamyurek. I, under the guidance of Dr. Saglamyurek, contributed towards the theoretical understanding of the ATS-protocol by performing numerical simulations of Maxwell-Bloch equations in the ATS-regime and relating the ATS-memory dynamics to certain phenomenological parameters. I have also done a detailed theoretical comparison (not reported in this thesis) of the ATS memory with some of the established memory protocols (EIT

and Raman memories) so as to find optimal regimes suited to each memory. Finally, the work presented in Chapter. 4 on the 'ATS light storage protocol' forms part of the recently submitted manuscript [Saglamyurek *et al.* arxiv.org:1710.08902 (2017)] which was accepted for publication in Nature Photonics on August 25, 2018.

*Dedicated to Amma-Baba, Maa-Papa ...*

# *Acknowledgements*

I would like to express my sincere gratitude to my supervisor Dr. Lindsay LeBlanc for her support, guidance and motivation throughout my masters' program and for giving me the opportunity to continue working in her group as a PhD student. She has always been accessible to me in addressing any issues or queries that I might have regarding the experiments. I am also thankful to her for meticulously proofreading my thesis and suggesting corrections and improvements wherever necessary. In the years to come, I am hopeful of absorbing at least some of her practical insights, experience and intuitions for solving research problems.

I would also offer my heartfelt thanks to Dr. Erhan Saglamyurek, the person with whom I have been working with, since last ten months, for giving me the opportunity to work in the quantum memory project, for the cheerfulness, enthusiasm and optimism he brings to the lab and for his great practical experience regarding lasers, fiber-optics and quantum memories. In the last couple of months, we have spent more time with each other in the lab, than with our families.

I also wish to offer my appreciation to my committee members: Dr. Frank Marsiglio and Dr. Michael Woodside for their time and consideration.

I wish to offer my sincere thanks to Logan Cooke who was my partner-in-crime in setting up the optics and electronics for the K-system and for making the times we spent together enjoyable by sharing his anecdotes. A special thanks to Taras Hrushevskyi for providing occasional help in the lab and am hopeful that one day he would fulfill his promise of bringing me the 'Banana-cream pie'. Also a note of thanks to my other labmates: Benjamin Smith, Andrei Tretiakov and Jacques Thibault for providing a warm and friendly atmosphere in the group which makes working in the lab really fun and satisfying.

Lest I forget, I must also acknowledge Vel ([www.latextemplates.com](http://www.latextemplates.com)) for creating a wonderful, easy-to-use and professional thesis-style-latex-templates.

A big thank-you to the people of Edmonton and Canada in general, for being one of the most hospitable and polite nations in the world. I must also express my profound regards to all my family members, friends and relatives, back In India: their support and motivation has played an important role in shaping my life and making me what I am today. I especially dedicate this thesis to my parents and grandparents for standing by me in all my decisions and for always being proud of my achievements. Last but not the least,

I am thankful to the Almighty for giving me strength and determination and showing me the way through difficult times.

# Contents

<b>Abstract</b>	<b>ii</b>
<b>Preface</b>	<b>iv</b>
<b>Acknowledgements</b>	<b>vii</b>
<b>1 Introduction</b>	<b>1</b>
1.1 Structure of the thesis . . . . .	2
<b>I Laser Cooling of <math>^{39}\text{K}</math> atoms</b>	<b>4</b>
<b>2 Theory: Laser Cooling</b>	<b>6</b>
2.1 Introduction . . . . .	6
2.2 Cooling in a Two Level Atom . . . . .	7
2.2.1 Optical Molasses . . . . .	9
2.3 Cooling Beyond The Doppler Limit . . . . .	11
2.3.1 The $\text{Lin} \perp \text{Lin}$ Configuration : Sisyphus Cooling (1-D Model) . . . . .	13
2.3.2 The $\sigma^+ - \sigma^-$ Configuration : Sub-Doppler Cooling by Motion Induced Orientation (1-D Model) . . . . .	18
2.4 Laser Cooling by Velocity-Selective Coherent Population Trapping (VSCPT) . . . . .	21
2.4.1 1-D Model for VSCPT . . . . .	22
2.4.2 Coherent superposition of ground states and population trapping . . . . .	24
2.4.3 Populating Atoms into near zero velocity non-coupled states . . . . .	26
2.5 Sub Doppler Laser cooling of $^{39}\text{K}$ . . . . .	26
2.5.1 Hyperfine Structure of Alkali Atoms and Laser Cooling	27
2.5.2 Difficulty In Laser Cooling $^{39}\text{K}$ . . . . .	29
2.5.3 The Gray Molasses Cooling Scheme . . . . .	30

<b>3</b>	<b>Experimental Setup</b>	<b>35</b>
3.1	Atomic Transitions Needed In Our Experiment . . . . .	36
3.2	Overview of Optical Setup . . . . .	37
3.3	Frequency Stabilization of our Diode Lasers . . . . .	39
3.3.1	Saturated Absorption Spectroscopy . . . . .	40
3.3.2	Ground and Excited Crossover Transitions in saturated spectroscopy . . . . .	42
3.3.3	Saturated Spectrum for D1 and D2 lines in $^{39}\text{K}$ . . . . .	43
3.3.4	Using SAS for laser frequency locking . . . . .	46
3.4	Locking the D1 and D2 diode lasers . . . . .	53
3.4.1	PID Controllers: Polarity Selection . . . . .	55
3.4.2	Choosing PID Parameters . . . . .	56
3.5	Beat Frequency Stabilization of the Tapered- Amplifier Laser . . . . .	58
3.6	Optical Setup Revisited . . . . .	69
3.6.1	Generation of D2-beams . . . . .	69
3.6.2	Generation of D1-beams . . . . .	72
3.7	Magneto-Optical Traps . . . . .	74
3.7.1	Operating Principle: One-Dimensional Model . . . . .	75
3.7.2	Getting the cooling beams into the MOT chambers . . . . .	78
3.8	AOM based Laser Power Stabilization . . . . .	80
<b>II</b>	<b>A Novel Quantum Memory Protocol</b>	<b>87</b>
<b>4</b>	<b>A broadband ATS-based atomic quantum memory protocol</b>	<b>89</b>
4.1	Quantum Memories . . . . .	90
4.2	Popular Quantum Memory Protocols . . . . .	94
4.2.1	Electromagnetically Induced Transparency (EIT) based memory . . . . .	94
4.2.2	Off-resonant Raman memory . . . . .	95
4.2.3	Photon-echo memory . . . . .	95
4.3	Getting Started with Our Memory Scheme: The Autler-Townes Effect . . . . .	96
4.4	The ATS Memory protocol . . . . .	101
4.4.1	Maxwell-Bloch Equations . . . . .	102
4.4.2	ATS Memory Operation . . . . .	103
4.4.3	ATS memory efficiency . . . . .	109
<b>5</b>	<b>Summary and Future Directions</b>	<b>119</b>

**Bibliography**

# List of Tables

3.1	Saturated absorption transitions on D1-D2 lines . . . . .	44
3.2	Details of D2-line spectroscopy setup . . . . .	59
3.3	Details of D1-line spectroscopy setup . . . . .	60
3.4	A summary of frequencies for exciting various transitions on the D2 and D1 lines. . . . .	81

# List of Figures

2.1	1D Optical Molasses	11
2.2	Optical Molasses Curves	12
2.3	Sisyphus Effect Features	15
2.4	Energy dissipation through Sisyphus mechanism	16
2.5	$\sigma^+ - \sigma^-$ cooling	19
2.6	$\Lambda$ configuration in a VSCPT effect	23
2.7	Hyperfine Structure	28
2.8	Potassium hyperfine levels	31
2.9	Gray Molasses Conceptual	32
3.1	Marked Transitions on D2 and D1 line	36
3.2	Optical Setup	38
3.3	Schematic of SAS	41
3.4	Saturated Absorption Spectroscopy	45
3.5	AOM shifted Pump beam	47
3.6	Derivative of spectral features	49
3.7	Lock-In-Detection Technique	51
3.8	Derivative of spectroscopic features	61
3.9	Choosing correct PID-polarity	62
3.10	D2 laser lock optimization	63
3.11	D1 laser lock optimization	64
3.12	Beat-note frequency stabilization	67
3.13	One-dimensional MOT	76
3.14	4 by 4 beam-splitter	79
3.15	4 by 6 beam-splitter	80
3.16	AOM based laser power stabilization	82
3.17	FPGA based feedback design	83
3.18	PCB layout for laser-power servo	86
4.1	EIT and Raman Memory Scheme	92
4.2	EIT absorption and dispersion profiles	93
4.3	Bare and dressed atomic state picture	98

4.4	EIT and ATS Profiles . . . . .	99
4.5	Delaying the signal pulse by a fixed period in ATS memory . . . . .	105
4.6	On-demand storage and recall operation in ATS memory . . . . .	107
4.7	Pulsed Operation of ATS memory . . . . .	108
4.8	Memory efficiency conceptual block diagram . . . . .	112
4.9	Total memory efficiency in forward propagation . . . . .	114
4.10	3D plots showing the evolution of spin and photonic modes for an efficient broadband storage in forward propagation . . . . .	116
4.11	Total memory efficiency in backward propagation . . . . .	117
4.12	3D plots showing the evolution of spin and photonic modes for an efficient broadband storage in backward propagation . . . . .	118

# Chapter 1

## Introduction

An ultracold gas is a dilute gas of atoms ( $10^{14}/\text{cm}^3$ ) at temperatures on the scale of tens of nanokelvin. At such low temperatures, the de Broglie wavelength of each atom becomes comparable to the interatomic separation such that the atoms become indistinguishable, with their individual wavefunctions overlapping to form a collective, macroscopic wavefunction. The distribution of atoms in the energy landscape is governed by either the Bose-Einstein statistics (eg,  $^{87}\text{Rb}$ ,  $^{39}\text{K}$  and  $^{23}\text{Na}$ ) or Fermi-Dirac statistics (eg,  $^{40}\text{K}$  and  $^6\text{Li}$ ).

Ultracold Bose and Fermi gases offer great opportunity to experimentally model many-body interactions that occur in strongly correlated condensed matter systems [1, 2]. In these systems, one can not only customize / engineer interactions that occur in real solid state systems using experimentally controllable parameters (laser field intensity, laser-detuning, rf-fields), but also create many-body order which is not yet known to exist in conventional solid-state materials [3]. From this perspective, potassium is an important alkali metal candidate due to the existence of both fermionic and bosonic isotopes. Moreover, these isotopes have been studied to reveal broad, magnetically tunable Feshbach resonances in a number of hyperfine states [4]. These easily accessible resonances, when combined with spin-orbit coupling effects in an ultracold potassium gas, offer a rich interplay between superfluid and magnetic phases.

Laser-cooling is the first experimental step towards making an ultracold atomic gas, and is an elegant illustration of *light manipulating matter*. Lasers can be used to slow down atoms from their typical thermal velocities to velocities that could be few orders of recoil limit (recoil velocity of an atom is a fundamental quantity and is discussed more in the subsequent Chapter). The work discussed in the first half of this thesis is related to laser-cooling a gas of bosonic  $^{39}\text{K}$  atoms and the associated experimental setup. This work is a part of a long term experimental goal of creating many body order in

an ultracold  $^{39}\text{K}$  gas. A major challenge in cooling K lies in the fact that it has a narrow hyperfine structure in the D2-excited state (the preferred laser cooling transition), which limits the minimum temperature achievable using standard laser-cooling techniques, such as those based on gradient of polarization of the optical fields. This difficulty is circumvented by using an additional cooling cycle on the better-resolved D1 line, in a scheme known as ‘Gray-Molasses’ cooling. Enhanced cooling comes from the formation of long-lived ‘dark states’ as a result of quantum coherence between the hyperfine ground levels. In Chapter. 2, we present a detailed review of various laser-cooling mechanisms and also discuss the physics behind ‘Gray-Molasses’ scheme and its advantages in laser cooling species of potassium (as well as lithium). Chapter. 3 then gives a detailed description of the laser system and associated optical setup that we built, which at a later stage would be used to laser cool  $^{39}\text{K}$ .

The remaining half of this thesis focuses on a novel quantum memory protocol that facilitates the storage and manipulation of broadband pulses of light and hence can be used in the realization of high-speed quantum optical devices. The light storage is based on the resonant absorption of photons through dynamic ‘Autler-Townes’ split lines. Hence we have named the protocol as the ‘ATS Protocol’. This protocol can principally be implemented in any three-level system. As a proof-of-principle, we have stored nanoseconds long light pulses inside a cold Rb vapour upto a storage time of 1 microsecond [5]. In essence, this serves as a beautiful example of *matter manipulating light*. In this thesis, we will only touch upon the basic storage and retrieval mechanism of the ATS memory. Details of the experimental setup, comparison with other established quantum memories, high-speed manipulation of optical signals, bandwidth scaling, the ability to store single photon pulses, etc. will be the published in future work. A brief introduction of quantum memories followed by a detailed description of the ‘ATS-protocol’ is presented in Chapter. 4 of this thesis.

## 1.1 Structure of the thesis

The thesis is organized as follows:

**Chapter. 2** discusses in detail, the theory behind laser cooling. In particular, we describe the following models: Doppler-cooling; polarization gradient cooling (also known as sub-Doppler cooling) and the more subtle velocity selective population trapping. While discussing these models, we move

from a simple two-level atom picture to one that represents the multi-level structure of real atoms and their interaction with varying light fields. We also discuss the difficulty in laser cooling  $^{39}\text{K}$  on the basis of its energy level diagram. Finally, we describe the (simplified) operation of the recently developed ‘Gray-Molasses’ based sub-Doppler cooling that we intend to implement in our setup.

**Chapter. 3** contains a detailed description of our laser system. Schemes of the main blocks of the optical setup are presented: we identify and calculate the laser frequencies to excite specific atomic transitions in K within one cycle of the experiment and describe the associated lasers, optics and electronics. This chapter also includes a detailed account of two useful techniques for the frequency stabilization of our lasers.

In **Chapter. 4**, we introduce the ATS memory protocol for storing broadband light pulses, which is based on the coherent absorption of signal photons inside a (storage) medium via dynamically controlled ‘Autler-Townes’ splitting. The chapter begins with an introduction to atomic quantum memories in general together with a brief overview of some already existing light-storage protocols. We then describe the light storage and on-demand retrieval operations of our ‘ATS memory’, through the numerical modeling of light-matter interactions for a three-level atomic system. A detailed analysis of the factors determining the overall memory efficiency is also presented.

**Chapter. 5** concludes this thesis with planned experiments for future stages.

## Part I

# Laser Cooling of $^{39}\text{K}$ atoms

# List of Symbols

Symbol	Meaning	Units if applicable
$F_{\text{scatt}}$	Scattering force	N
$\hbar k$	Single photon recoil momentum	Ns
$k$	Wave-vector of light field	$\text{m}^{-1}$
$\Omega$	Rabi frequency of laser field	$2\pi \times \text{MHz}$
$\delta$	Detuning of laser field	$2\pi \times \text{MHz}$
$ g\rangle$	Atomic ground state	
$ e\rangle$	Atomic excited state	
$\Gamma$	Spontaneous decay rate between $ g\rangle$ and $ e\rangle$	$2\pi \times \text{MHz}$
$s_0$	On-resonance saturation parameter	
$\rho_{ee}$	Excited state atomic population	
$\gamma_P$	Photon scattering rate off a two-level atom	
$K_B$	Boltzmann constant	$\text{JK}^{-1}$
$T_D$	Doppler cooling limit	K
$v_r$	Recoil velocity	$\text{ms}^{-1}$
$\beta$	Damping coefficient	$\text{kg s}^{-1}$
$\omega_0$	Atomic transition frequency	$2\pi \times \text{MHz}$
$\omega_L$	Laser frequency	$2\pi \times \text{MHz}$
$\omega_D$	Doppler-shift	$2\pi \times \text{MHz}$
$C_{ge}$	Clebsch-Gordan coefficient for a given dipole transition	
$\Psi_C$	Coupled (bright) state	
$\Psi_{NC}$	Non-coupled / weakly coupled state	
$\Delta$	Two-photon Raman detuning	$2\pi \times \text{MHz}$
$\sigma^\pm$	Right and left circular polarizations of the light field	

## Chapter 2

# Theory: Laser Cooling

### 2.1 Introduction

In Chapter 1, the importance of quantum degenerate gases in simulating many body interactions was discussed. The very first phase towards making an ultracold gas of any atomic species is the laser cooling and trapping of the atomic ensemble. By carefully tuning the laser frequency, one can exert velocity dependent, dissipative forces to decelerate an atomic beam, resulting in cooling that leads to an increased phase-space density [6]. This increased phase-space density is crucial for the future stages of evaporative cooling required to achieve quantum degeneracy .

Sub-Doppler laser cooling is quite efficient in cooling down alkali atoms such as  $^{23}\text{Na}$  ,  $^{133}\text{Cs}$  and  $^{87}\text{Rb}$  [7, 8, 9, 10]. In these atoms, the cooling cycle is principally implemented on the D2 line that has a broad excited state hyperfine manifold. However, isotopes of atoms as K and Li have a narrow hyperfine structure in their D2 excited state due to low values of the corresponding hyperfine splitting coefficients [11, 12]. The relative closeness of the hyperfine levels in the excited state makes the standard sub-Doppler cooling inefficient and, thus, an additional cooling cycle on the D1 line is used. The advantages of the D1 cooling cycle and its subtle differences with regards to the D2 counterpart are addressed in this Chapter.

This Chapter is organised as follows, first, the cooling force based on the scattering of photons from a simple two-level atom is described (§. 2.2). This model exploits the Doppler shift of moving atoms and hence is aptly termed ‘Doppler cooling’. The actual cooling mechanisms (which give sub-Doppler temperatures) are more subtle and can only be accounted for by extending the simple two-level atom picture to include both the multiplicity of the atomic ground state levels and optical pumping processes among the ground state sublevels induced by the laser fields. Two sub-Doppler cooling models

are discussed based on the gradient of polarisation of the light fields: Sisyphus cooling, based on  $lin \perp lin$  polarization of laser beams (§. 2.3.1), and motion-induced orientation cooling, based on  $\sigma^+ - \sigma^-$  polarization (§. 2.3.2). Although both these models result in the same order-of-magnitude of friction coefficients, the cooling mechanisms are somewhat different [13]. We then describe another intricate cooling mechanism based on a strong interplay between an atom's internal (spin) and external (centre-of-mass motion) degrees of freedom, called velocity-selective coherent population trapping (VSCPT)[14]. VSCPT is discussed in (§. 2.4). We finally show that implementing an additional D1 cooling cycle benefits from both polarization-gradient cooling and VSCPT, thereby leading to lower temperatures (§. 2.5.3). This is particularly useful for the case of  $^{39}\text{K}$ ,  $^{40}\text{K}$ ,  $^6\text{Li}$  and  $^7\text{Li}$ , which otherwise cannot be efficiently cooled using the standard D2 cooling cycle [15, 16, 17].

## 2.2 Cooling in a Two Level Atom

We consider the picture of an atom having only two states: a ground state and an excited state, and an external perturbation given by a classical laser field. The semiclassical Optical Bloch Equations (OBE) describing the time-evolution of this two level atom in the presence of the near-resonant laser field have been described in [6, 18] and those results shall be directly used here.

The use of light forces to decelerate an atomic beam relies on the momentum exchange between the atoms and photons resonant with an atomic transition. Each photon carries a momentum  $\hbar k$  with it. Let us consider an atom in the ground state and moving opposite to a photon's direction of propagation  $\vec{k}$ . Upon absorption, the atom transits to the excited state and receives a momentum kick in the direction opposite to that of its motion. Each 'kick' reduces the atomic velocity by  $\vec{v}_r = \hbar \vec{k} / M$ , known as the recoil velocity, where  $M$  is the mass of the atom. A typical recoil velocity for an atom is orders of magnitude less than the r.m.s. thermal velocity of an atomic ensemble. As an example, the r.m.s. velocity of atoms in a potassium vapour is  $\approx 560$  m/s at 500 K, whereas the recoil velocity is only 13 mm/s. However, multiple absorption events over a long timescale would result in a large number of 'kicks', thereby reducing the atomic velocity significantly. Note that each excited atom eventually decays to the ground state through spontaneous emission. Each spontaneous decay event changes the atom's momentum in a 'random' direction and thus many such events result in a zero

net momentum transfer. Thus, the net effect is slowing down of atoms in the direction of the laser beam. The force that results from absorption followed by spontaneous emission is called the scattering force.

A formal expression for the scattering force is obtained using:

$$\begin{aligned} F_{\text{scatt}} &= (\text{Momentum exchanged per event}) \times (\text{No. of events / time}) \\ &= \hbar k \times (\text{Photon scattering rate}) \end{aligned}$$

In steady-state light-atom interaction, the excitation rate equals the decay rate. Thus, the total scattering rate of photons from the atoms can be given by:

$$\gamma_p = \Gamma \rho_{ee}, \quad (2.1)$$

where  $\rho_{ee}$  is the density matrix element corresponding to the excited-state population and  $\Gamma$  is the natural linewidth of the excited state or the spontaneous decay rate. The excited-state population in the steady state is given by [6]:

$$\rho_{ee} = \frac{s_0/2}{1 + s_0 + \left(2(\delta + \omega_D)/\Gamma\right)^2}. \quad (2.2)$$

Here  $\delta$  is the laser detuning from the atomic transition,  $\omega_D$  is the Doppler shift seen by the moving atoms, and  $s_0$  is the on-resonance saturation parameter, defined as  $s_0 = 2\Omega^2/\Gamma^2$ , where  $\Omega$  is the Rabi frequency defining the coupling strength between the laser electric field and atomic dipole moment.

Therefore, the scattering force can be written as :

$$F_{\text{scatt}} = \hbar k \left( \frac{s_0 \Gamma / 2}{1 + s_0 + \left(2(\delta + \omega_D)/\Gamma\right)^2} \right) \quad (2.3)$$

Some remarks about this force:

- The effective detuning component in the denominator of Eqn. 2.3 includes the laser detuning as well as the Doppler-shifted frequency seen by moving atoms. The Doppler shift is given by  $\omega_D = -\hat{k} \cdot \hat{v}$ . Hence, atoms moving in the beam direction would see a smaller laser frequency ( $\omega_L - kv$ ), while those moving in the opposite direction would see a higher laser frequency ( $\omega_L + kv$ ). An obvious implementation of laser cooling would then be to direct a laser beam that is red-detuned with respect to an atomic transition (that is,  $\delta = \omega_L - \omega_{\text{Atom}} < 0$ ), and counter-propagating to the atomic beam. In this case, a positive Doppler-shift will compensate the negative detuning such that the laser is nearly resonant (blue shifted) with the atomic transition in the rest frame of the atoms.

- To maximize the light absorption and hence the scattering rate, the effective detuning  $\delta_{\text{eff}} \equiv \delta + \omega_{\text{D}}$  must be small. More precisely,  $|\delta_{\text{eff}} = \delta + \omega_{\text{D}}| \ll \Gamma$
- At very high intensities we have  $\Omega \gg \Gamma$  or equivalently  $s_0 \gg 1$ . Therefore,

$$\begin{aligned}
 \gamma_{\text{p}} &= \frac{s_0 \Gamma / 2}{1 + s_0 + (2\delta_{\text{eff}} / \Gamma)^2} \\
 &= \frac{s_0}{1 + s_0} \times \frac{\Gamma / 2}{1 + \left(\frac{2\delta_{\text{eff}}}{\Gamma \sqrt{1+s_0}}\right)^2} \\
 &\approx \frac{\Gamma / 2}{1 + \left(\frac{\delta_{\text{eff}}}{\sqrt{2}\Omega}\right)^2} \\
 &\approx \Gamma / 2.
 \end{aligned}$$

We see that the maximum scattering rate is limited to half the spontaneous decay rate, which means the scattering force at high intensities saturates to  $F_{\text{scatt,max}} = \hbar k \Gamma / 2$ . Thus, the scattering force does not increase indefinitely with increasing laser intensity. Higher intensities result in increased absorption, however, the stimulated emission also increases. Absorption followed by stimulated emission does not result in any net change in the atomic momentum, thereby, saturating the force to  $\hbar k \Gamma / 2$ . The factor of two occurs because at high intensities, an atom has a 50 percent probability of being either in the ground or in the excited state.

### 2.2.1 Optical Molasses

Let us consider two counter-propagating beams derived from the same laser and having equal intensity and frequency. In the low-intensity limit, the net radiative force on an atom can be calculated simply by linearly superimposing the scattering forces (equation 2.3) due to the two individual beams. Moreover, at low intensities, effects such as simultaneous absorption of a photon from one beam followed by stimulated emission due to the other beam can be neglected. It is, however, worthwhile to mention that for real atoms (which have degenerate ground and excited state levels), such effects give rise to more sophisticated cooling processes, which I will discuss later (§. 2.4).

In the 1-D picture considered here, for an atom at rest, the scattering forces are equal and opposite, and hence balance each other out. However, atoms moving along the beams experience a net force that is proportional to their velocity and whose sign depends on the laser detuning. This is the consequence of the Doppler effect. If the laser frequency is red-detuned, the beam moving opposite to atomic motion is blue-shifted in frequency and hence gets closer to resonance. Likewise, the beam moving in the direction of atoms would be red-shifted in frequency and gets further away from resonance. Thus, atoms scatter more photons from the beam that is opposite to their motion, and this differential scattering results in a net damping force (Fig. 2.1). The resultant damping force can mathematically be expressed as:  $F_D = F_{\text{scatt}}(\delta - kv) - F_{\text{scatt}}(\delta + kv)$ , with the two components being the forces exerted on the atoms by the laser beams that are parallel and anti-parallel to the atomic motion respectively. Substituting Eqn. 2.3 for the scattering forces and considering  $s_0 \ll 1, kv \ll \Gamma$ , we get the total force as [18]:

$$\vec{F}_D = \frac{8\hbar k^2 \delta s_0 \vec{v}}{\Gamma(1 + s_0 + (2\delta/\Gamma)^2)^2} = -\beta \vec{v}, \quad (2.4)$$

where the detuning  $\delta < 0$  so that the friction coefficient  $\beta$  is positive. As shown in Fig. (2.2), the net force is linear over a certain range of velocities ( $\approx \Gamma/k$ ) referred to as the capture velocity range. This range sets the limit on atomic velocities over which the damping is effective. By implementing three pairs of counter-propagating laser beams (at low intensities and red detuning) in an orthogonal configuration, one can effectively cool the atoms in all six directions. This 3-dimensional laser cooling technique was termed ‘Optical Molasses’ [19], by analogy to the viscous forces in fluids.

We next turn to the question of what sets the limit on the minimum achievable temperature in Doppler cooling: each absorption or emission event changes the atomic momentum by one recoil momentum ( $\hbar \vec{k}$ ). We considered the scattering force as the average force from the absorption of photons. Due to the discrete nature of photons, the scattering process is not a continuous one and hence there is always some fluctuation associated with the number of photons absorbed in a given time interval. Similarly, while we consider a zero average force due to spontaneously emitted photons, there exists a finite scatter around this zero due to fluctuations in the emission processes. Hence, such scattering events cause an atom to undergo a random walk in momentum space with a step size equal to the recoil momentum. The net result can be thought of as small oscillations on top of the velocity

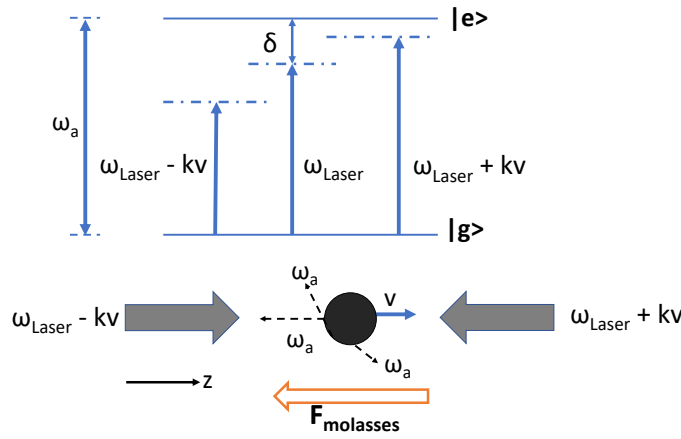


FIGURE 2.1: Optical molasses scheme in one dimension for a two level atom that has a velocity component  $v$  along the  $z$ -axis. The two counter-propagating laser beams are red-detuned from the  $|g\rangle - |e\rangle$  transition. Owing to the Doppler shift, the beam propagating along  $-z$  is closer to resonance and hence would be scattered more than the beam along  $+z$ . The apparent frequencies seen by the atom are shown. Thus, the atom experiences a net force along  $-z$ , which is proportional to the velocity  $v$ . This is analogous to viscous forces in fluids. Each absorption event is followed by a random spontaneous emission (shown as dashed black arrows). Adapted from [18].

change caused by the average scattering force, thereby increasing the velocity spread (which is equivalent to heating). For a 3-dimensional optical molasses, there is a balance between the heating and cooling processes at equilibrium with the steady-state kinetic energy given by  $\hbar\delta/8(2|\delta|/\Gamma + \Gamma/2|\delta|)$  [6]. This kinetic energy is minimum at  $\delta = -\Gamma/2$ , and consequently the minimum temperature, also called the Doppler temperature, can be obtained from  $k_B T_D = \hbar\Gamma/2$ . A remarkable point about the Doppler temperature is that it is solely dependent on the atomic parameter (natural linewidth  $\Gamma$ ) and is independent of laser intensity. Again, the assumption of low laser power is implied here.

### 2.3 Cooling Beyond The Doppler Limit

A careful measurement of the velocity distribution of sodium atoms that were cooled by 3-dimensional optical molasses revealed temperatures much lower than the predicted Doppler limit [20]. In fact, the temperature limit was suggested to be of the order of the recoil limit with the recoil temperature  $T_r$  given by  $k_B T_r = \hbar^2 k^2 / 2M$ . In this section, we discuss two models

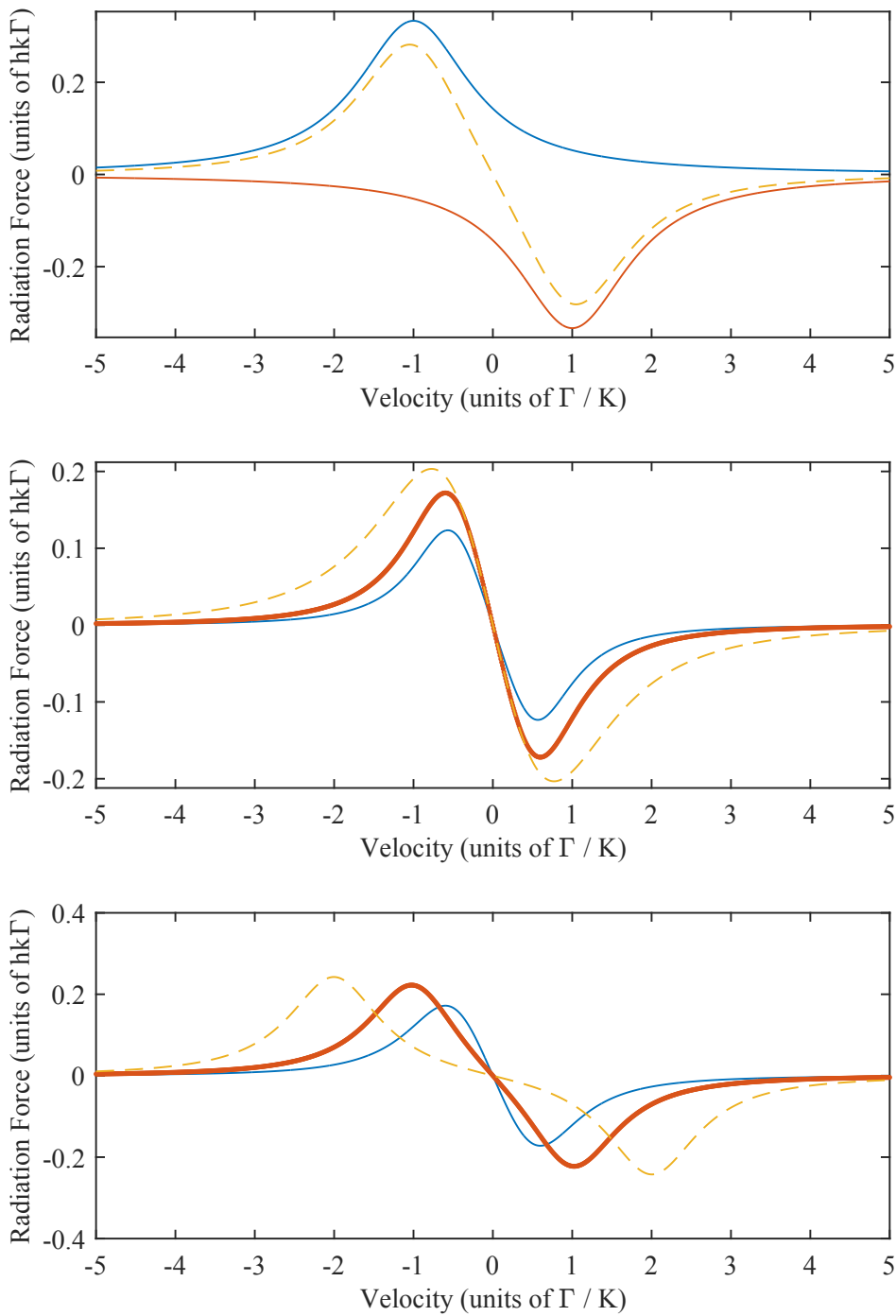


FIGURE 2.2: **(Top)** Velocity dependent damping force in 1 dimension. The solid curves are the forces from individual beams while the dashed curve is the sum. Here  $\delta = -\Gamma, s_0 = 2$ . **(Center)** Total scattering force at  $\delta = -\Gamma/2$  and different laser intensities :  $s_0 = 1$  (blue), 2 (solid brown) and 4 (dashed brown) respectively. **(Bottom)** Total Scattering force at fixed intensity ( $s_0 = 1$ ) and different laser detunings corresponding to  $\delta = -\Gamma/2$  (blue) ,  $-\Gamma$  (solid brown) and  $-2\Gamma$  (dashed brown) respectively.

which describe a more realistic picture of cooling mechanisms that lead to sub-Doppler temperatures [13]. The salient features of these models include:

- Hyperfine levels and magnetic sublevels present in multilevel atoms.
- Light-induced energy shifts of the atomic states.
- Polarization gradients that cause spatially dependent optical couplings.
- The non-adiabatic response of the internal atomic state to the variations in laser fields that a moving atom ‘sees’.

The spatial dependence of light fields due to polarization gradients is discussed in the subsequent sections. Here, an internal atomic state refers to the ground state population among the various Zeeman sublevels. The non-adiabatic response comes from the fact that this ground state population is strongly dependent on the position of the atom in the laser fields: as the atom moves through a spatially varying light-field, the internal state tries to adiabatically follow the local ground state. It does so by optically pumping the population among the ground state sublevels. However, in the low-intensity regime (where laser cooling is generally implemented), these pumping processes are weak (i.e.  $\Omega \ll \Gamma$  which leads to  $\Gamma_p \ll \Gamma$  where  $\Gamma_p$  is the optical pumping rate). Hence, long pumping times result in a lag between the internal atomic response and the atomic motion, thereby causing non-adiabatic effects. We now discuss two cases of polarization gradients in a 1-dimensional optical molasses:

### 2.3.1 The $Lin \perp Lin$ Configuration : Sisyphus Cooling (1-D Model)

We consider two counter-propagating, plane waves at frequency  $\omega_L$  and equal electric field amplitudes  $E_0$  and orthogonal linear polarizations. We choose the propagation direction along  $\hat{z}$  and the transverse polarization vectors along  $\hat{x}$  and  $\hat{y}$ . Let  $\vec{k}$  denote the wave vector of the laser beams. The resultant electric field can then be given by:

$$\begin{aligned} \vec{E} &= E_0 \hat{x} \cos(\omega_L t - k_z z) + E_0 \hat{y} \cos(\omega_L t + k_z z) \\ &= E_0 [(\hat{x} + \hat{y}) \cos \omega_L t \cos k_z z + (\hat{x} - \hat{y}) \sin \omega_L t \sin k_z z] \end{aligned} \quad (2.5)$$

The axis of the resultant polarization vector remains fixed, however, its ellipticity changes with a periodicity of half the laser wavelength as shown in Fig. 2.3 (a):

- At  $z = 0$ ,  $\vec{E} = E_0(\hat{x} + \hat{y}) \cos \omega_L t$ . The electric field is linearly polarized at an angle of  $\pi/4$  with respect to  $x$ -axis .
- At  $z = \lambda/8$ ,  $\vec{E} = E_0(\hat{x} \sin(\omega_L t + \pi/4) + \hat{y} \cos(\omega_L t + \pi/4))$ . Light is  $\sigma^-$  polarized around the  $z$  axis.
- At  $z = \lambda/4$ ,  $\vec{E} = E_0(\hat{x} - \hat{y}) \sin \omega_L t$ . The electric field is linearly polarized at an angle of  $-\pi/4$  with respect to  $x$ -axis .
- At  $z = 3\lambda/8$ ,  $\vec{E} = E_0(\hat{x} \cos(\omega_L t + \pi/4) + \hat{y} \sin(\omega_L t + \pi/4))$  : Light is  $\sigma^+$  polarized around the  $z$  axis.
- At  $z = \lambda/2$ ,  $\vec{E} = -E_0(\hat{x} + \hat{y}) \cos \omega_L t$ , and the ellipticity repeats.

We consider the simplest case of a  $J_g = 1/2 \rightarrow J_e = 3/2$  transition in an atom whose ground and excited state Zeeman sublevels are shown in Fig. 2.3 (b). The shift in the ground state atomic energies due to applied laser fields (in the low-intensity regime of  $s_0 \ll 1$ ) is given as [6]:

$$\Delta E_g = \frac{\hbar \delta s_0 (C_{ge})^2}{1 + (2\delta/\Gamma)^2}. \quad (2.6)$$

Here  $C_{ge}$ 's are the Clebsch-Gordan coefficients that represent the coupling strength between a ground state sublevel and the external laser field. An important thing to notice is that the direction of the light-induced energy shifts depend on the sign of the laser frequency detuning (i.e. the atomic levels are shifted downwards in energy with respect to the unperturbed levels for  $\delta < 0$  and upwards for  $\delta > 0$ ). As a side note, this is one of the major differences between the conventional sub-Doppler schemes such as those described here ( $\delta < 0$ ) and the 'Gray molasses' scheme ( $\delta > 0$ ) discussed in §. 2.5.3. Moreover, for a given electric field polarization,  $C_{ge}$  values are different for different transitions (Fig. 2.3 (b)). The  $m_j = 1/2$  has a stronger optical coupling when polarization is  $\sigma^+$  (larger light shift), while the  $m_j = -1/2$  couples more strongly to light when polarization is  $\sigma^-$ . Both levels are equally shifted for linear polarization. Thus, when we have a periodic, spatially-varying polarization, the light shifts also oscillate in space (Fig. 2.3 (c)) with the same period ( $\lambda/2$ ). The gradient of the spatially modulated energies give rise to the dipole force.

For stationary atoms exposed to such polarization gradients in the steady-state, the ground state population is also position dependent. As an example, atoms at  $z = \lambda/8$  would be optically pumped to the  $m_g = -1/2$  level since the polarization is  $\sigma^-$ . This could be explained using Fig. (2.3 (b)): If an

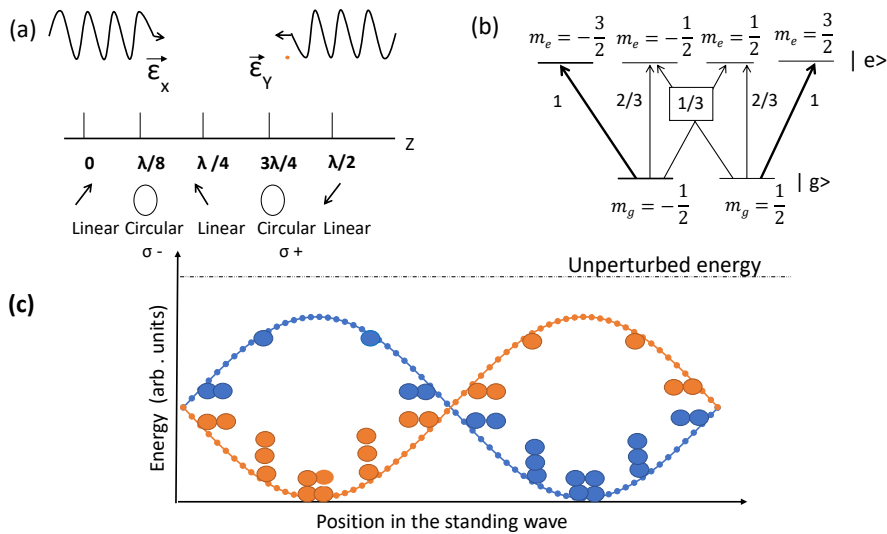


FIGURE 2.3: Features of a  $lin \perp lin$  configuration. (a) Two counter-propagating laser beams in orthogonal linear polarization. The polarization vectors,  $\vec{\epsilon}_x$  and  $\vec{\epsilon}_y$  are chosen along the  $x$  and  $y$  axes respectively. The resultant polarization vector changes on the sub-wavelength length scale with a periodicity of  $\lambda/2$ . (b) Ground and excited state sublevels for a  $J_g = 1/2 \rightarrow J_e = 3/2$  transition, along with the transition probabilities given by the squares of Clebsch-Gordan coefficients. Adapted from [13]. (c) Spatial variation in light shifted ground state energies for the  $m_g = -1/2$  level (orange) and  $m_g = +1/2$  level (blue). Also shown is the steady state population distribution as a function of position of stationary atoms in the laser field.

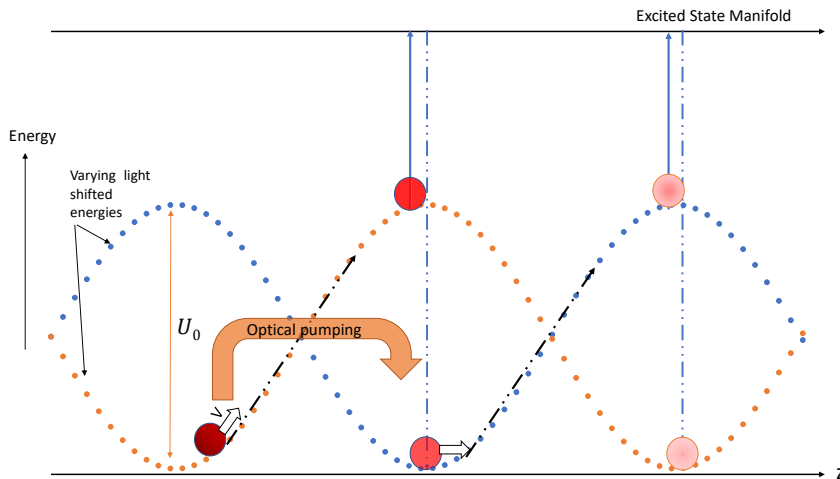


FIGURE 2.4: Kinetic Energy dissipation via Sisyphus mechanism. The ‘hills and valleys’ represent the potential energy of the light shifted ground state atomic levels in space. An atom moving along the  $z$ -axis has to travel up and down these hills and valleys. Kinetic energy is lost during the ‘uphill motion’ and gained during the ‘downhill motion’. An atom that starts at  $z = \lambda/8$  climbs up the potential hill corresponding to the  $m_g = -1/2$  state till it reaches  $z = 3\lambda/8$  where the polarization changes to  $\sigma^+$  and it gets optically pumped to the  $m_g = 1/2$  state. It then starts climbing up another hill and the same sequence is repeated again. The kinetic energy is lost as the atom does more ‘uphill motion’ than the ‘downhill motion’. The process is effective over a range of velocities given by  $v\tau_p = \lambda/4$ , where  $\tau_p$  is the pumping time.

atom is initially in the  $m_g = +1/2$  state, it absorbs a  $\sigma^-$  photon and is excited to  $m_e = -1/2$  state. Selection rules allow it to decay to either of the ground substates, however, the  $|\frac{3}{2}, \frac{-1}{2}\rangle \rightarrow |\frac{1}{2}, \frac{-1}{2}\rangle$  transition is twice as strong as the  $|\frac{3}{2}, \frac{-1}{2}\rangle \rightarrow |\frac{1}{2}, \frac{1}{2}\rangle$  transition. Once in  $m_g = -1/2$  state, it can only be coupled to the  $m_e = -3/2$  state shown by the thick line in the figure. A similar description applies to atoms at  $z = 3\lambda/8$ , where they are optically pumped to the  $m_g = 1/2$  state by virtue of the light polarization being  $\sigma^+$ . The population transfer between the two ground state sublevels is called optical pumping and plays a crucial role in laser cooling. In this configuration, since  $m_g = -1/2$  has a larger light shift for a  $\sigma^-$  polarization and vice versa for  $m_g = +1/2$ , optical pumping processes end up transferring the atoms to the lowest energy state. At positions such as  $z = 0, \lambda/4, \lambda/2$ , where the light is linearly polarized, light shifts of the two ground sublevels are equal and the atoms equally populate the two levels.

Next we consider an atom moving along the positive  $z$ -direction with  $z = \lambda/8$  as the initial position where it is in the  $m_g = -1/2$  Zeeman sublevel. As it moves, it climbs up the potential hill corresponding to the light shift of the

$m_g = -1/2$  state, at the expense of its kinetic energy. If the atomic velocity  $v$  is such that the atom remains in the same potential hill as it traverses a distance of  $\lambda/4$  over a time interval  $\tau_p$  (i.e.  $v\tau_p = \lambda/4$ ), then the atom would reach the top of the hill before being optically pumped to the other sublevel at  $z = 3\lambda/8$ . Here  $\tau_p$  is known as the optical pumping time and we can define the optical pumping rate as  $\Gamma_p = 1/\tau_p$ . In the optical pumping process, an atom absorbs a photon of lower frequency and spontaneously emits a photon of higher frequency with the difference equivalent to the height of the light-shifted potential. Thus, an atom loses kinetic energy twice: first while climbing up the potential hill and second due to optical pumping when it reaches the top of the hill. This process is repeated over multiple cycles until the atom has a kinetic energy smaller than the height of the potential hill itself (as shown in Fig. 2.4). This allows a rough estimation of the equilibrium temperature as [18]:

$$k_B T_s \simeq U_0 \propto \Omega^2 / |\delta|. \quad (2.7)$$

Here,  $T_s$  is the final temperature,  $U_0$  is the height of the light-shifted potential hill, and the remaining symbols have their usual meanings. This shows that low final temperatures can be obtained by reducing the laser intensity ( $\Omega^2 \propto I$ ) and/or increasing the laser detuning. While this is true upto a certain extent, the temperature does not decrease indefinitely with  $I/|\delta|$ . As mentioned earlier, for the pumping process to be effective, atoms must be localized within  $\sim \lambda/4$ . This gives them a momentum spread of  $\sim \hbar k$ , which is the single photon recoil momentum. Thus, the lowest sub-Doppler temperature is set by the recoil energy and is indeed, much lower than what was predicted in initial Doppler cooling.

The time lag or non-adiabaticity (§. 2.3) in the following of internal atomic state to the changing laser field comes due to long pumping times between the ground state sublevels. This means that optical pumping occurs at timescales much longer than the excited state lifetime;  $1/\tau_p = \Gamma_p \ll \Gamma$ . A consequence of the long pumping times is a stronger friction force, whose coefficient  $\beta$  was derived in [13] as:

$$\beta = -\hbar k^2 \frac{\delta}{\Gamma}. \quad (2.8)$$

The result of Eqn. 2.8 was obtained for  $\Omega \ll \Gamma, \Gamma_p \ll \Gamma$  and  $|\delta| \gg \Gamma$ . The maximum coefficient of friction for two-level Doppler cooling can be obtained by applying similar conditions to Eqn. 2.4 and it comes out as  $\hbar k^2 / (\frac{\delta}{\Gamma})^3$ . Thus, with this new mechanism at work, the damping is higher by a factor of  $(\frac{\delta}{\Gamma})^4$ .

However, the capture velocity for the sub-Doppler cooling ( $\sim \Gamma_p/k$ ) is much smaller than the corresponding Doppler cooling mechanism ( $\sim \Gamma/k$ ).

### 2.3.2 The $\sigma^+ - \sigma^-$ Configuration : Sub-Doppler Cooling by Motion Induced Orientation (1-D Model)

The authors of [13] described another laser-cooling mechanism based on the atomic motion in a standing wave formation arising from the superposition of two counter-propagating laser beams having opposite circular polarizations. Although the physical cooling mechanism in this configuration is different from Sisyphus cooling (sec. 2.3.1), the effective capture velocity and the equilibrium temperature are of the same order of magnitude.

To start with, it can be shown that in the  $\sigma^+ - \sigma^-$  configuration, the resultant electric-field polarization rotates as one moves along the standing wave; however, it maintains its ellipticity in space. Let us consider two counter-propagating laser beams that have equal amplitudes  $E_0$ , frequency  $\omega_L$ , and that the beam travelling along  $z > 0$  is  $\sigma^+$  polarized (and vice versa for the second beam). As before,  $\hat{x}$  and  $\hat{y}$  are unit vectors along the transverse direction. The resultant electric field can then be written as:

$$\begin{aligned}\vec{E} &= E_0[\hat{x} \sin(\omega_L t - kz) - \hat{y} \cos(\omega_L t - kz)] \\ &\quad + E_0[\hat{x} \sin(\omega_L t + kz) + \hat{y} \cos(\omega_L t + kz)] \\ &= 2E_0 \sin \omega_L t [\hat{x} \cos kz - \hat{y} \sin kz].\end{aligned}\tag{2.9}$$

Hence, the total electric field is linearly polarized with the unit polarization vector  $\epsilon = \hat{x} \cos kz - \hat{y} \sin kz$  (Eqn. 2.9). The polarization remains linear, however, it rotates by an angle  $\theta = -kz$ , as one moves along the standing wave in the  $z$ -direction (see Fig. 2.5), with a periodicity of the laser wavelength  $\lambda$ . Comparing equations (2.9) and (2.5), we see that for a  $\sigma^+ - \sigma^-$  scheme, the light shift in the ground states remains constant for all  $z$  and as such no gradient of potential exists, thereby dismissing any possibility of a Sisyphus like effect.

We first look at the steady-state population distribution in the ground state when the atoms are stationary, by considering the following picture: We consider the  $J_g = 1 \rightarrow J_e = 2$  transition, with ground and excited sublevels along with their transition probabilities shown in Fig. 2.5 (b). It is convenient to work in the angular momentum basis such that we chose the quantization axis along the direction of the local polarization. Then the Zeeman sublevels

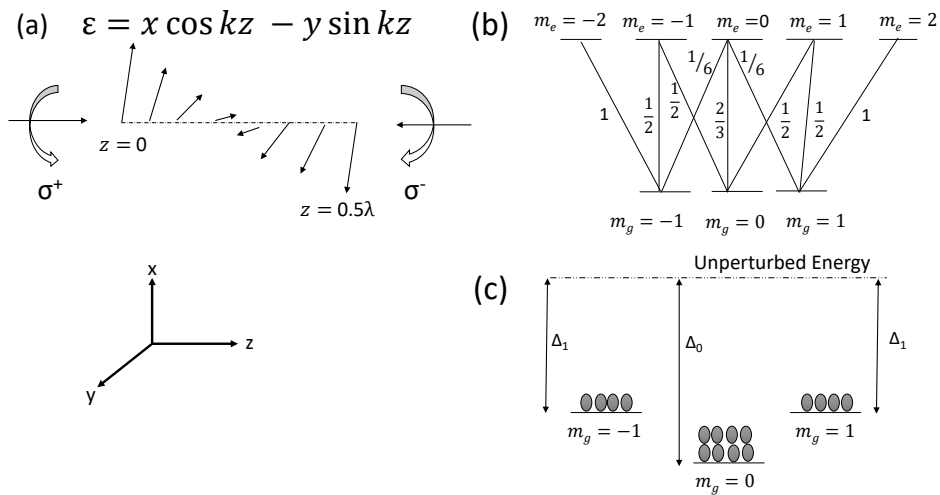


FIGURE 2.5: Features of a  $\sigma^+ - \sigma^-$  configuration. (a) Two counter-propagating laser beams in opposite circular polarizations. The resultant electric field is linearly polarized, but rotates along  $z$ -axis with a pitch  $\lambda$ . (b) Ground and excited state sublevels for the  $J_g = 1 \rightarrow J_e = 2$  transition along with the transition probabilities given by the squares of Clebsch Gordan coefficients. Adapted from [13]. (c) Light-shifted ground state sublevels corresponding to  $J_g = 1$  state. These energies do not oscillate in space as the polarization is linear everywhere. The  $m_g = 0$  sublevel has a stronger light shift than the  $m_g = \pm 1$  sublevels. The quantization axis is chosen along the local polarization axis and thus, the Zeeman sublevels are the eigenstates of the projection of the total angular momentum  $\hat{J}$  along the rotating polarization defined by Eqn. (2.9). Also shown are the steady state atomic distribution at any position  $z$  for atoms at rest. Optical pumping tends to populate the  $m_g = 0$  sublevel more than other sublevels. Adapted from [13].

are simply the eigenstates of the component of the angular momentum ( $\hat{j}$ ) along the direction of the local polarization. As an example, at  $z = 0$  the polarization  $\epsilon$  is along  $\hat{x}$ , implying that the ground and excited states of the atom at  $z = 0$  are the eigenstates of  $\hat{j}_x$ . Since, the polarization and hence, the quantization axis, rotates along  $z$ , the eigenstates change and hence, we have a wavefunction that varies in space. With atoms at rest, optical pumping with a  $\pi$ -polarization populates more atoms in the  $m_g = 0$  state than  $m_g = \pm 1$  states. This is true for any position  $z$  along the laser standing wave and can be understood using simple probability arguments. The population transfer from  $m_g = \pm 1$  levels to  $m_g = 0$  level is more probable ( $\frac{1}{2} \times \frac{1}{2} = \frac{1}{4}$ ) than the transfer from  $m_g = 0$  to  $m_g = \pm 1$  levels which is ( $\frac{2}{3} \times \frac{1}{6} = \frac{1}{9}$ ) (Fig. 2.5 (b)). Similarly, as the light is coupled more strongly to the  $m_g = 0$  state than the  $m_g = \pm 1$  states (the Clebsch-Gordan coefficient is higher for  $m_g = 0$  state), the associated light shift for  $m_g = 0$  is also higher. As in Sisyphus cooling, the ground state is shown (Fig. 2.5 (c)) to experience a downward energy shift due to the red-detuned laser beams.

In the above description, the steady-state-distribution resulted in the following observations: more atoms populate  $m_g = 0$  sublevel; and the other two sublevels  $m_g = \pm 1$  have an equal population. Non-adiabaticity arises when atomic motion causes the atoms to traverse a region of rotation of quantization axis such that the atoms need to be optically pumped so as to have a steady state distribution in the ground state that is appropriate to the local electric field. Again at low laser powers when  $\Gamma_p \ll \Gamma$ , pumping times are long and hence, there is a time lag between the actual ground state distribution of atomic population to the expected steady state distribution at a given point in space. This lag results in a population imbalance between the two otherwise equally populated  $m_g = \pm 1$  states [13]; atoms moving towards the  $\sigma^+$  beam tend to populate the  $m_g = 1$  sublevel more than  $m_g = -1$  sublevel and vice versa. This effect is known as *motion-induced-orientation*, in the sense that ground state alignment of an atom is sensitive to its motion (whether it is towards the  $\sigma^+$  beam or the  $\sigma^-$  beam). Moreover, an atom in the  $m_g = 1$  sublevel has a six times higher probability (Fig. 2.5 b) to scatter a  $\sigma^+$  photon than a  $\sigma^-$  photon. The spontaneous emission that follows sends it back to the  $m_g = 1$  sublevel (the only allowed transition Fig. 2.5 (b)) and thus, many scattering cycles can occur, effectively damping its velocity. A similar description applies for atoms traveling towards the  $\sigma^-$  beam thereby populating the  $m_g = -1$  sublevel.

It must be reiterated that while the cooling does occur due to the differential scattering of photons, this differential scattering itself results from the imbalance in the ground state populations caused by the non-adiabaticity of the internal atomic state in following the steady state population (appropriate to the local laser field). As such, this is entirely different from Doppler cooling that occurs due to the differential scattering of photons caused by the difference in Doppler shift. Further, in practical experiments, the laser cooling stage is often preceded by a magneto-optical trapping (MOT) stage (see §. 3.7) that can work only when the counter-propagating beams are in a  $\sigma^+ - \sigma^-$  configuration. Since the same MOT beams can be used for sub-Doppler cooling, the motion-induced-orientation cooling is the mechanism at work in most of the real experiments involving cold atoms.

## 2.4 Laser Cooling by Velocity-Selective Coherent Population Trapping (VSCPT)

So far we have seen two energy scales in the context of laser cooling that defined the lowest achievable temperatures: the Doppler cooling limit ( $\hbar\Gamma/4$ ) and the recoil limit ( $\hbar^2k^2/2M$ ). In this section, we discuss a cooling mechanism known as velocity-selective coherent population trapping (VSCPT), that can surpass the single photon recoil limit via the formation of a velocity selective dark state into which atoms could remain indefinitely trapped. These ‘dark’ or nearly dark states are characterized by a narrow velocity spread around  $v = 0$  and the basic idea is to pump a large number of atoms into such states. Since temperature is defined as the width of velocity / momentum distribution, atoms accumulated into near zero velocity states can have sub-recoil temperatures. The first experimental demonstration of VSCPT was done in [14] where metastable helium was cooled to half of its recoil temperature.

The term ‘dark state’ requires some clarification; dark states refer to those atomic states that are not coupled to light, that is, atoms in these states are invisible to light fields. Some states are trivially dark, that is, they cannot be excited because the light has either a wrong frequency or the polarization is such that selection rules do not allow a transition to higher state. Such trivial dark states, for example, occur on the D1 line in alkali atoms ( $F \rightarrow F' = F$  and  $F \rightarrow F' = F - 1$  transitions). However, the more interesting case is when Dark states are ‘created’ as a coherent superposition of states through

processes like the two-photon Raman coupling. The zero coupling to light in these states occurs due to destructive interference between the excitation amplitudes of individual states that make up the superposition. That said, a distinction must be made between a state that is ‘dark’ and a state that is ‘non-coupled’: An atom in a non-coupled state cannot directly absorb light, however, it can evolve into an absorbing state through motional coupling. This motional coupling comes from the external momentum of the atom’s center of mass. Once in the bright state, it can be excited by the laser field. Therefore, a non-coupled state is not a true trapping state. Dark states, on the other hand, are characterized by near zero velocities and hence, motional coupling to other bright states does not exist. Hence, a dark state is a perfect trapping state in that atoms can stay there indefinitely. In the following subsections, we describe how such states can be created; what causes population trapping and how that amounts to cooling.

### 2.4.1 1-D Model for VSCPT

We consider the three-level  $\Lambda$  configuration on a  $J_g = 1 \rightarrow J_e = 1$  transition as considered in [14] and [21]: two degenerate ground state sublevels ( $g_{-1}$  and  $g_1$ ) are coupled to an excited level ( $e_0$ ) by two counter-propagating beams that are  $\sigma^+ - \sigma^-$  polarized (Fig. 2.6). The suffix ‘g’ and ‘e’ refer to ground and excited states while notations  $g_{rm\pm 1}$  and  $e_0$  indicate  $|g, m_g = \pm 1\rangle$ ,  $|e, m_e = 0\rangle$  respectively. Further, to give a quantum mechanical treatment to the atomic motion (this becomes necessary at low velocities), the atomic states are labeled with quantum numbers that specify both internal and external degrees of freedom. As an example,  $|g_1, p\rangle$  refers to an atom in the ground state with spin  $m_g = 1$  and a momentum with the value  $p$  for its  $z$ -component (we set the propagation axis of the laser beams along  $z$ ). The change in momentum would only be due to absorption or emission of photons and hence is specified in terms of  $\hbar k$ .

To understand the formation of dark states, we need to know what causes a coherent superposition among the ground state sublevels. As seen in Fig. 2.6, the ground and excited magnetic sublevels can be coupled in four different ways ( $g_1 \rightarrow e_0, g_0 \rightarrow e_1 : \sigma^+; g_1 \rightarrow e_0, g_0 \rightarrow e_{-1} : \sigma^-$ ). As  $g_0 \rightarrow e_0$  is a forbidden transition, optical pumping empties the  $g_0$  level, thereby rendering only  $g_{\pm 1}, e_0$  levels important for the analysis that follows. We chose the direction of  $\sigma^\pm$  beams along  $\pm z$ . An atom in a ground state  $|g_{-1}, p - \hbar k\rangle$  can be

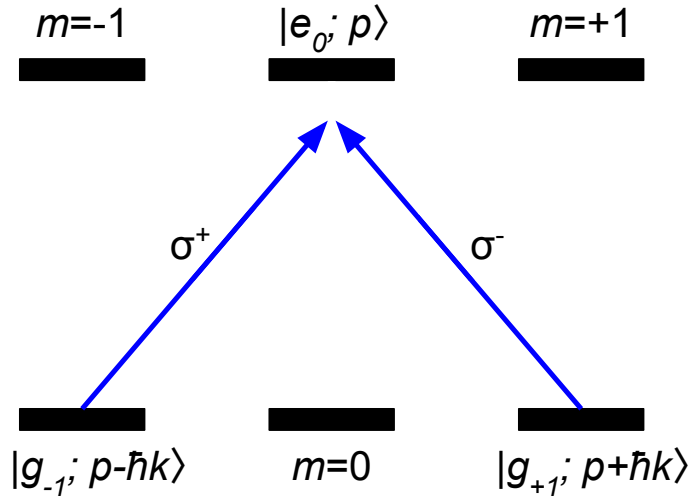


FIGURE 2.6: Magnetic sublevels for a  $J_g = 1 \rightarrow J_e = 1$  transition. The atomic states are labeled using two quantum numbers: magnetic quantum number that specifies the internal spin and the  $z$  component of the external momentum. Two-photon Raman transitions induced by the  $\sigma^+ - \sigma^-$  beams couple the two ground levels  $|g_{\pm 1}, p \pm \hbar k\rangle$  using the excited level  $|e_0, p\rangle$  thereby creating a closed momentum family of three states (see text). As the  $m_g = 0 \rightarrow m_e = 0$  transition is forbidden, the  $g_0$  sublevel is quickly emptied by optical pumping and thus, is not included in the cooling process.

transferred to another ground state  $|g_1, p + \hbar k\rangle$  via two-photon Raman processes that involve simultaneous absorption from one beam (in this case  $\sigma^+$ ) followed by emission stimulated by the other beam ( $\sigma^-$  for this case). This transfer occurs through the intermediate excited level  $|e_0, p\rangle$ . Thus, for each value of  $p$ , a closed momentum family  $F(p)$  can be defined that includes the three states coupled by absorption-stimulated emission cycles [14, 21]. For the case discussed above, we have:

$$F(p) = \{|g_{-1}, p - \hbar k\rangle, |e_0, p\rangle, |g_1, p + \hbar k\rangle\} \quad (2.10)$$

The coupling between the two ground states via an excited state results in formation of new states that are linear combinations of  $|g_1, p + \hbar k\rangle$  and  $|g_{-1}, p - \hbar k\rangle$  (Eqns. 2.16 and 2.17). One of these combinations yields a state that has a finite dipole moment with the excited state and hence is coupled to light. The other combination yields a state with a zero dipole moment and hence is non-coupled. The non-coupled state can be a true dark state when its components are characterized by a certain momenta and hence, is velocity-selective.

## 2.4.2 Coherent superposition of ground states and population trapping

Considering a classical description for the counter-propagating laser fields, the total electric field vector  $\vec{E}(z,t)$  is given by:

$$\vec{E} = E_0\epsilon_+ \left( \exp(i(kz - \omega_L t)) + c.c. \right) + E_0\epsilon_- \left( \exp(-i(kz + \omega_L t)) + c.c. \right) \quad (2.11)$$

where  $\epsilon_{\pm}$  represent  $\sigma^{\pm}$  circular polarizations along  $\pm z$  direction respectively. The laser beams are of same frequency  $\omega_L$  and amplitude  $E_0$ . The Hamiltonian for the atom-light system can be written as:

$$\hat{H} = \hat{H}_A + \hat{H}_{\text{Kin}} + \hat{H}_{\text{int}} \quad (2.12)$$

In the above equation,  $\hat{H}_A$  represents the bare atomic Hamiltonian and gives the internal atomic energies. Assuming the ground spin states  $|g_1\rangle$  and  $|g_{-1}\rangle$  have the same energy and choosing this energy as zero for convenience,  $H_A = \hbar\omega_0|e_0\rangle\langle e_0|$ , where  $\omega_0$  is the resonant frequency between  $|g_{\pm 1}\rangle$  and  $|e_0\rangle$ . The term  $\hat{H}_{\text{kin}} = \hat{P}^2/2M$  is the kinetic energy operator that describes the atom's center-of-mass motion.  $\hat{H}_{\text{int}}$  is the interaction term describing the atom-laser coupling and the associated light shifts:

$$\hat{H}_{\text{int}} = -\hat{D} \cdot \vec{E}(z, t) \quad (2.13)$$

where  $\hat{D}$  is the electric dipole moment operator that connects  $|g_{\pm 1}\rangle$  and  $|e_0\rangle$ . The coupling strengths are expressed in terms of Rabi frequencies  $\Omega_{\pm}$  given by:

$$\Omega_{\pm} = -\frac{\langle e_0|\epsilon_{\pm} \cdot \hat{D}|g_{\pm 1}\rangle}{\hbar} \quad (2.14)$$

Since the Clebsch-Gordan coefficients for  $\sigma^{\pm}$  beams are equal, we have  $\Omega_{\pm} = \Omega$ . The final expression for the interaction Hamiltonian including the external degree of freedom (momentum  $\mathbf{P}$ ) is given by [21]:

$$\hat{H}_{\text{int}} = \frac{\hbar\Omega}{2} \sum_{\mathbf{p}} \left( |e_0, \mathbf{p}\rangle \langle g_{-1}, \mathbf{p} - \hbar\mathbf{k}| + |e_0, \mathbf{p}\rangle \langle g_1, \mathbf{p} + \hbar\mathbf{k}| \right) + H.c. \quad (2.15)$$

Here the summation operates over the  $z$  component values of external momentum operator ( $\hat{P}$ ). The atom-laser coupling term includes only those transitions that occur within a closed momentum family of states, as given by

equation (2.10). The superposition states resulting from the coupling between ground states of a particular momentum family  $F(p)$  can be written as:

$$\Psi_C(p) = \frac{1}{\sqrt{2}}[|g_{-1}, p - \hbar k\rangle + |g_1, p + \hbar k\rangle] \quad (2.16)$$

$$\Psi_{NC}(p) = \frac{1}{\sqrt{2}}[|g_{-1}, p - \hbar k\rangle - |g_1, p + \hbar k\rangle] \quad (2.17)$$

Eqn. (2.16) describes an absorbing state that has a non-zero coupling to the excited state via laser photon:  $\langle e_0, p | H_{\text{int}} | \Psi_C(p) \rangle = \frac{\hbar\Omega}{\sqrt{2}} \exp(-i\omega_L t)$  whereas equation (2.17) describes a state that cannot be coupled to light since  $\langle e_0, p | H_{\text{int}} | \Psi_{NC} \rangle = 0$ . The excitation vanishes for the non-coupled state due to the destructive interference between the transition amplitudes of the component states. To examine the situation when a non-coupled state becomes a perfect dark state, we first consider the time evolution of an atom that was initially in a  $|\Psi_{NC}(p)\rangle$  state. Denoting  $\rho$  as the density matrix operator,  $\langle \Psi_{NC}(p) | \rho | \Psi_{NC}(p) \rangle$  represents the population in the state  $|\Psi_{NC}(p)\rangle$ . The time-dependence of the population can be obtained following the equation of motion  $i\hbar \frac{\partial \rho}{\partial t} = [\rho, H]$  and is given as [21]:

$$\frac{d}{dt} \langle \Psi_{NC}(p) | \rho | \Psi_{NC}(p) \rangle = -i \frac{kp}{M} \langle \Psi_{NC}(p) | \rho | \Psi_C(p) \rangle + c.c. \quad (2.18)$$

We see that an atom in  $|\Psi_{NC}(p)\rangle$  state can couple into an absorbing state  $|\Psi_C(p)\rangle$  with coupling strength proportional to  $kp/M$ . This motional coupling is the result of evolution of free atomic Hamiltonian ( $H_A + H_{\text{kin}}$ ). Hence, although  $|\Psi_{NC}(p)\rangle$  does not directly couple to an excited state, it can evolve into an absorbing state at a rate proportional to its velocity and is thus not a stationary state. However, for  $p = 0$ , the motional coupling vanishes and atoms prepared in  $|\Psi_{NC}(0)\rangle$  remain in this state. In other words,  $|\Psi_{NC}(0)\rangle$  represents the true dark state. Another way to look at it is that the components  $|g_{\pm 1}, \pm \hbar k\rangle$  of  $|\Psi_{NC}(0)\rangle$  have the same internal and kinetic energies and thus,  $|\Psi_{NC}(0)\rangle$  is the stationary state of Hamiltonian  $H$ . On the other hand, the kinetic energies of  $|g_{\pm 1}, p \pm \hbar k\rangle$  that make up  $|\Psi_{NC}(p)\rangle$  differ by  $2\hbar kp/M$ , and hence, this is not a stationary state and it can evolve in time. In nut shell, an atom in state  $|\Psi_{NC}(p)\rangle$  would oscillate between  $|\Psi_{NC}(p)\rangle$  and  $|\Psi_C(p)\rangle$  at the frequency  $2kp/M$ . This suggests that smaller the value of  $p$ , the more decoupled  $|\Psi_{NC}(p)\rangle$  is and more is the time an atom would spent in this state. Hence by accumulating atoms into non-absorbing states that have narrow momentum distribution ( $\pm \delta p$  around  $p = 0$ ), we achieve velocity-selective atom trapping. The final temperature is dependent on the width

of momentum distribution, which, itself depends upon how much time an atom spends in a non-coupled state and thus, the single photon recoil-limit is not the fundamental limit in this process.

### 2.4.3 Populating Atoms into near zero velocity non-coupled states

The factor responsible for accumulating atoms into non-coupled states with near zero velocity is spontaneous emission. A series of spontaneous emission events can lead to distribution of atoms among different momentum families by random walks in momentum space. These random walks continue until atoms are pumped into such states that are strongly or completely decoupled to light, where they remain trapped. An example of an atom jumping from one momentum family  $F(p)$  to another  $F(p')$  is as follows: consider an atom in  $|e_0, p\rangle$  state. In these notations,  $p$  refers to the eigenvalue of  $z$ -component of momentum operator. Upon spontaneous decay, let us assume that atomic momentum along  $z$  direction changes by an amount  $p'$  such that  $p'$  lies within the range  $(-\hbar k, \hbar k)$ . Therefore, the atom would end up being either in  $|g_1, p - p'\rangle$  or in  $|g_{-1}, p - p'\rangle$  state. Both the ground states belong to different momentum families:  $|g_1, p - p'\rangle$  is a part of  $F(p - p' - \hbar k)$  while  $|g_{-1}, p - p'\rangle$  belongs to  $F(p - p' + \hbar k)$  (see Eqn. 2.10). Spontaneous emission can thus shift atoms from a family  $F(p)$  to  $F(p')$  such that  $p - \hbar k \leq p' \leq p + \hbar k$ . The diffusion in momentum space over sufficiently long times, would, in theory, distribute atoms into states belonging to  $F(p = 0)$ , where the optical excitation ceases. In that case, the final momentum distribution along  $z$  would show two resolved peaks at  $\pm \hbar k$  showing the signature of a coherent dark state trapping [14]. The time an atom spends in a non-coupled state is inversely proportional to the decay rate of that state. Higher the interaction time, larger will be the height of momentum distribution and narrower the width ( $\delta p$ ). For  $\delta p \ll \hbar k$  at large interaction times ( $\gg \Gamma^{-1}$ ), sub-recoil temperature can be obtained.

## 2.5 Sub Doppler Laser cooling of $^{39}\text{K}$

One of the long term goals in our lab is to create and explore many-body order in a gas of ultracold  $^{39}\text{K}$  atoms. A fully functional apparatus for producing BEC of  $^{87}\text{Rb}$  atoms is already in place [22] and incorporating a BEC of K atoms in the same apparatus would provide an opportunity to study the

phase space of a two-species BEC. This can be done by using tunable interactions provided by established techniques of Feshbach resonances and spin-orbit coupling [23]. Laser Cooling would be the first step towards making a quantum degenerate  $^{39}\text{K}$  gas. However, the hyperfine energy level structure in K makes it difficult to laser cool using conventional sub-Doppler schemes. To understand this, we first look at the hyperfine structure of alkali atoms in general from the purview of laser cooling.

### 2.5.1 Hyperfine Structure of Alkali Atoms and Laser Cooling

The electronic configuration of an alkali atom can be written as:  $(1s)^2(2s)^2(2p)^6 \dots (ns)^1$ , where  $n$  is the principal quantum number for the outermost shell. Since the outermost shell of an alkali atom has one valance electron, the contribution to orbital and spin angular momentum of the atom ( $\hat{L}$ ,  $\hat{S}$ ) comes only from the momenta of this valance electron ( $\hat{l}$ ,  $\hat{s}$ ). The total angular momentum of the atom ( $\hat{J} = \hat{L} + \hat{S}$ ) is then the same as that of the valance electron ( $\hat{j} = \hat{l} + \hat{s}$ ). The  $\hat{L} \cdot \hat{S}$  coupling splits the energy states giving rise to the fine structure in an atom. In Russel - Saunders notation, an electronic state can be represented by  $n^{2S+1}L_J$  where the value of  $J$  varies from  $|L - S|$  to  $|L + S|$  in integer steps. It is noted that without the hat notation, the symbols  $J, L, S$  etc. represent the eigen values of their respective momentum operators. The interaction of the angular momentum  $\hat{J}$  with the nuclear spin  $\hat{I}$  further lifts the degeneracy in atomic states giving rise to the hyperfine energy structure, with the total angular momentum  $\hat{F}$  now given as  $\hat{J} + \hat{I}$ . As before,  $F$  can take eigenvalues between  $|J - I|$  to  $|J + I|$  in integer steps. The electronic state is now designated as  $|n^{2S+1}L_J, F\rangle$ . A schematic energy diagram showing the coarse, fine and hyperfine levels for an atom with  $I = 3/2$  is shown in Fig. 2.7.

To laser cool a thermal gas of some alkali atoms, a cooling transition between a ground and an excited hyperfine level must be established. Whether or not an external laser field can induce some coherence between such levels is dictated by the selection rules: as an example, for electric dipole transitions, selection rules for both excitation and spontaneous emission are given by:  $\Delta F = 0, \pm 1$  [6]. Hence, the choice of a cooling transition is limited by selection rules. Effective cooling requires a large number of photon scattering events and thus, the coupling strength between the two chosen levels must be high. Further, the spontaneous decay from the excited level must be to

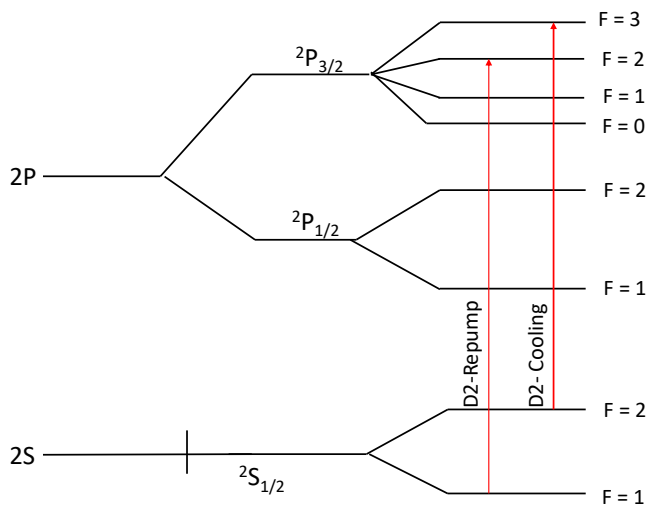


FIGURE 2.7: Conceptual schematic showing coarse, fine and hyperfine energy levels in an atom with  $I = 3/2$ . The fine structure is attributed to the spin-orbit interaction while hyperfine splitting occurs due to the interaction between total angular momentum and nuclear spin. Also shown are the typical cooling and repump transitions on the D2 line. The arrangement of cooling-repump beams ensure that atoms remain in the cooling cycle.

the level that is coupled by light so that an atom remains in the cooling cycle. In view of these considerations, the cooling transition in an alkali atom is chosen between the highest ground and excited levels on the D2 line. From a technical standpoint, lasers corresponding to D2-wavelengths are available for a variety of atoms. An example is shown in Fig. 2.7, with  ${}^2S_{1/2} \rightarrow {}^2P_{3/2}$  as the cooling transition. In this case, the radiative decay from  $F_e = 3$  can only occur at  $F_g = 2$  and thus, atoms always stay within the cooling cycle. There is, however, a finite off-resonant excitation probability for an  $F_g = 2$  to  $F_e = 2$  transition<sup>1</sup>. Atoms that are excited to  $F_e = 2$  then have a good chance to decay to  $F_g = 1$  state and would hence, be lost from the cooling cycle. Thus, almost all laser cooling schemes use an additional ‘repump’ laser beam (which in the shown figure couples  $F_g = 1$  and  $F_e = 2$  levels). The use of a repump transition ensures that escaped atoms return back the cooling cycle. Most practical experiments implementing laser-cooling in three dimensions, use three orthogonal pairs, each consisting of counter-propagating cooling beams (an extension of the 1-D optical molasses scheme) and at least one pair of the repump beam.

<sup>1</sup>The probability for such excitation to occur is related to the detuning with respect to the off-resonant excited level. Greater the detuning, lesser is the transition probability.

## 2.5.2 Difficulty In Laser Cooling $^{39}\text{K}$

Historically, among the popular alkali atoms that have been laser cooled, such as  $^{23}\text{Na}$ ,  $^{133}\text{Cs}$  and  $^{87}\text{Rb}$ , cooling is usually implemented on the D2 line with the cooling transition being an  $F \rightarrow F' = F + 1$  (Fig. 2.7). One of the advantages of implementing laser cooling on the D2 line is that the same  $F \rightarrow F + 1$  transition can also be used in the implementation of the Magneto-Optical-Trapping (MOT) stage. The capture velocity in a MOT is significantly higher than in the sub-Doppler techniques and therefore, loading warm atoms first into a MOT followed by sub-Doppler cooling enhances both the atom number and phase space density. Practical experiments therefore implement a D2 line MOT which is followed by the sub-Doppler cooling on the same line. Such an arrangement is less technologically demanding since the cooling and repump transitions in both the stages are the same with the corresponding beams differing only in their intensity and detuning: parameters that can be easily tuned.

The reason why conventional sub-Doppler cooling on the D2 line works so well in the aforementioned species has to do with the wide energy separation among the hyperfine levels in the D2 excited manifold. This makes it possible to isolate the cooling and repump transitions such that the cooling cycles are not affected due to the presence of other levels. Thermal energies of atoms are dissipated via either Sisyphus effects or motion induced orientation effects. However, alkali isotopes of both K and Li have closely spaced hyperfine levels in their D2 excited state. Looking at the energy levels in  $^{39}\text{K}$  (Fig. 2.8), the D2 manifold has narrowly spaced energy levels such that the frequency separation between two consecutive levels is of the order of natural linewidth in  $^{39}\text{K}$  ( $\Gamma/2\pi \approx 6$  MHz). In such cases, it is rather difficult to resolve a single cooling transition: (1) As the levels are so closely spaced, it is not possible to have a cooling transition detuned from just one level. Since, sub-Doppler cooling requires large detunings (see equation 2.7), the cooling laser gets effectively detuned from the entire manifold instead of the single  $F' = 3$  level. (2) Off-resonant excitation to other levels increase the effective linewidth of the cooling transition. This is equivalent to increasing the minimum temperature (in analogy with the Doppler limit which is proportional to the transition linewidth. Precise tuning of D2 lasers close to resonance have achieved temperatures around 25 - 35  $\mu\text{K}$  in  $^{39}\text{K}$  [24, 25]. Similarly, operating an additional MOT stage on a transition with a smaller linewidth has achieved temperatures close to 33  $\mu\text{K}$  and 63  $\mu\text{K}$  for  $^6\text{Li}$  and  $^{40}\text{K}$  respectively [26, 27].

A new sub-Doppler cooling scheme, called *Gray Molasses* has recently been uncovered that involves cooling and repump transitions blue-detuned to the D1 line. Such transitions are shown for  $^{39}\text{K}$  in Fig. 2.8 whereby the cooling transition is between  $^2S_{1/2} F = 2 \rightarrow ^2P_{1/2} F = 2$  and the repump between  $^2S_{1/2} F = 1 \rightarrow ^2P_{1/2} F = 2$ . The excited levels are well separated (if one compares the same among D2 levels) and so off-resonant excitations are less probable. Experimental demonstrations have shown that this D1 line cooling scheme is well suited for atomic species such as  $^{39}\text{K}$ ,  $^{40}\text{K}$ ,  $^6\text{Li}$  and  $^7\text{Li}$  [15, 16, 28, 29] that have a relatively close-packed D2 excited state. A general cooling strategy for these atoms would then involve a D2 MOT stage followed by some combination of red-detuned D2 molasses and blue-detuned D1 molasses. Next, we discuss how cooling using D1 line incorporates the effects of a Sisyphus like cooling as well as those that arise due to the formation of velocity-selective dark states leading to population trapping.

### 2.5.3 The Gray Molasses Cooling Scheme

A Gray molasses scheme operating on the D1 line involves either an  $F \rightarrow F$  or an  $F \rightarrow F - 1$  transition. As shown in Fig. 2.9, for any polarization of the incident field, such transitions involve one or two dark states that are not coupled to the light field. This kind of a situation does not arise for an  $F \rightarrow F + 1$  transition. Here non-coupling to light is only due to the wrong polarization and as such, these dark states are trivial. More interesting ones are those that can be created as a coherent superposition of  $|F, m_F\rangle$  Zeeman sublevels. One such superposition was discussed in sec. 2.4, whereby two counter-propagating laser beams in opposite circular polarizations, led to coherent Raman coupling between degenerate Zeeman sublevels of a ground state. Yet, a more complicated mechanism underlying the formation of non-coupled states arises on the D1-line cooling: (1) Unlike the previous section involving a single laser field that acted on a  $J \rightarrow J' = J$  transition, here we have bi-chromatic fields (cooling and repump) that couple two different ground hyperfine levels ( $F - 1$  and  $F$ ) to a common excited level ( $F'$ ). (2) In a complete picture, all possible dipole transitions among the ground and excited hyperfine levels ( $|F, m_F\rangle \rightarrow |F', m_{F'}\rangle$ ) are to be considered. (3) Dark states are formed due to the superposition involving both  $F$  and  $F - 1$  levels [17] when the special Raman resonance condition is met (discussed later in the text). As the intensity of repump beam is weaker than that of cooling, a

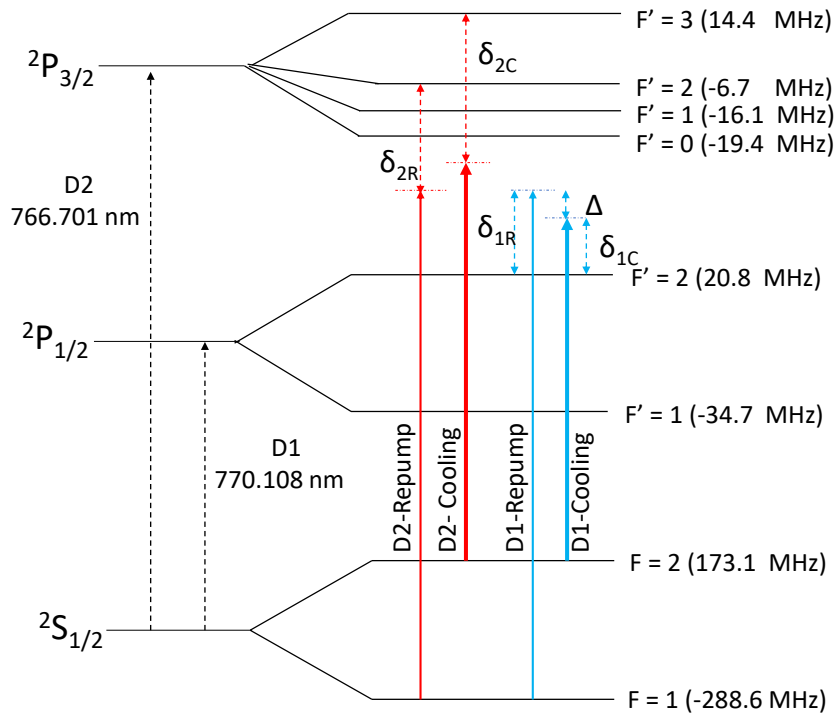


FIGURE 2.8: D1 and D2 hyperfine levels in  $^{39}\text{K}$  [15]. The D2 manifold has a width of  $\approx 33.8$  MHz such that the spacing between two consecutive levels is of the order of the natural linewidth ( $\Gamma/2\pi \approx 6$  MHz). D1 manifold on the other hand is relatively better resolved with the spacing between the two levels  $\approx 56$  MHz. Also shown are the cooling and repump transitions on the D1 and D2 lines. The D2 line cooling and repump beams are red-detuned from resonance by  $\delta_{2C}$  and  $\delta_{2R}$  respectively. The corresponding D1 lasers are blue-detuned by  $\delta_{1C}$  and  $\delta_{1R}$  respectively. The relative strengths of cooling and repump beams are indicated by the line thickness. Also shown is the relative detuning between D1 cooling and repump beams with respect to the  $F' = 2$  level, indicated by  $\Delta$ .

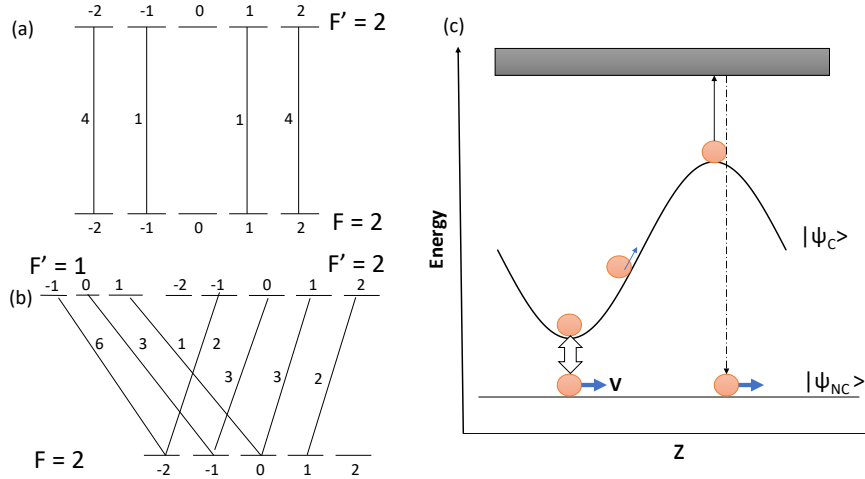


FIGURE 2.9: Transition strengths of various  $m_F$  levels for (a)  $\pi$  and (b)  $\sigma^+$  polarizations respectively, on a D1 line for  $^{39}\text{K}$  ( $I = 3/2$ ). It is evident that there exists one (two) trivial dark state for  $F \rightarrow F$  ( $F \rightarrow F - 1$ ) transition regardless of the incoming polarization. Transition strengths taken from [6]. c: Schematic of a 1-D Gray Molasses cooling [16]. As the lasers are blue-detuned, the bright states ( $\Psi_C$ ) have positive light-shifts with respect to the non-coupled ( $\Psi_{NC}$ ) states. Here we assume a periodic spatial modulation in light shifts similar to Sisyphus mechanism. State  $\Psi_{NC}$  can evolve into  $\Psi_C$  via motional coupling. Once in  $\Psi_C$ , atoms can lose kinetic energy by climbing up the potential hill and then getting pumped to a non-coupled state. This process can continue till atoms are pumped into near zero velocity states where they remain trapped.

dark state possesses more of  $F - 1$  ground level character (as corresponding sublevels are weakly coupled due to low repump power) than the  $F$  level.

In a simplified picture, we consider a three-level,  $\Lambda$ -type system formed using  $|^2S_{1/2}, F = 1\rangle$ ,  $|^2S_{1/2}, F = 2\rangle$  and  $|^2P_{1/2}, F = 2\rangle$  levels (see Fig. 2.8), driven by a strong cooling and a weak repump field. Both beams are considered to be blue-detuned with respect to the excited level  $F' = 2$ . The interaction of bi-chromatic fields with this system forms new eigenstates, two of which are coupled to the light field (bright states) and one is non-coupled [30, 29]. Using the familiar notations  $\Psi_C$  and  $\Psi_{NC}$  for absorbing and non-absorbing states,  $\Psi_C$ 's would be light-shifted upwards in energy with respect to the unperturbed  $\Psi_{NC}$  state, as the detuning is positive (see Eqn. 2.6). Depending on the polarization arrangement of the beams, atoms in  $\Psi_C$  would see either a spatially varying polarization or a rotating linear polarization. The former being simpler to visualize is considered in Fig. 2.9, showing one bright state and the non-coupled state: Spatial gradient of polarization results in spatially varying light-shifted energy in  $\Psi_C$ , the gradient of which

is the dipole force. Kinetic energy is then dissipated through the usual Sisyphus effect: atoms climb up the potential hill and get optically pumped to either a bright state with lower light shift or to a non-coupled state.  $\Psi_{\text{NC}}$  state can evolve into  $\Psi_{\text{C}}$  via evolution of the free atomic Hamiltonian (equation 2.18). This simple 1-D picture therefore combines the cooling effects of both polarization-gradients and VSCPT. The probability of transfer from  $\Psi_{\text{NC}}$  to  $\Psi_{\text{C}}$  is maximum when the energy difference between the states is minimum. The cooling cycles continue until atoms get pumped into near zero-velocity dark states such that evolution into a bright state is not possible. When in such states, they are strongly decoupled to light which can be experimentally detected by reduced fluorescence (hence the name, 'Gray Molasses').

A more rigorous picture would involve considering the dipole interaction among the entire 16 hyperfine levels spanning the ground and excited states of the D1 manifold in  $^{39}\text{K}$ . The authors of [17] considered the position dependent light- shifts among the hyperfine levels of the complete Hamiltonian that are 'dressed' by cooling and repump fields. Essential features included: **(1)** They found a robust correlation between the light-shifts and the decay rates of the corresponding dressed states. Dressed states that experience low light-shifts have long decay times. Hence, slowly moving atoms tend to accumulate in states with low light-shifts as departure rates of these states is small. The  $F = 1$  levels are weakly dressed by the low intensity repump beam and hence dominate the contribution to a non-absorbing / weakly-coupled state. **(2)** An important parameter while implementing Gray molasses is the relative detuning  $\Delta$  between the repump and the cooling beams with respect to the common excited level. As shown in Fig. 2.8,  $\Delta = \delta_{1\text{R}} - \delta_{1\text{C}}$ . It has been shown both theoretically as well as experimentally that, low temperatures are obtained over a certain range of negative values of  $\Delta$ , however, minimum temperature corresponds to the case when  $\Delta = 0$ : this condition is called the 'Raman-resonance condition'. A possible explanation is as follows: for  $\Delta < 0$ , weakly coupled states are formed due to coherence among the  $m_{\text{F}}$  sublevels that belong to the same  $F$  level. When  $\Delta = 0$ , ground hyperfine levels  $F = 1$  and  $F = 2$  split into bright and (nearly) dark manifolds. The dark manifold involves superposition between the  $m_{\text{F}}$  sublevels belonging to the two  $F = 1$  and  $F = 2$  states, that is to say, coherence is induced between the sublevels of different ground hyperfine levels. The coupling strength of this nearly dark manifold is much weaker than those that are formed by individual cooling and repump couplings when  $\Delta < 0$ . Atoms thus tend to accumulate in this manifold. The Raman resonance condition, thus, enhances

the sub-Doppler cooling effects. **(3)** As the Raman resonance requires superposition between  $F = 1, 2$  levels, there must be a fixed phase between the cooling and repump laser beams. In our experiment, we achieve this by generating both the D1 beams using the same laser source. The repump beam is generated as a first order sideband of the cooling beam via an electro-optic modulator (see Chapter. [3](#)).

## Chapter 3

# Experimental Setup

This Chapter describes the laser and optics system needed to cool  $^{39}\text{K}$ . It is important to mention at this point that while we have designed and built the complete setup and characterized the various subsystems, laser cooling sequences using this optical setup are yet to be implemented. This is because we have not yet introduced the K-source inside the vacuum of our experimental chambers. Since the actual cooling has not been performed at the time of writing this thesis, follow-up measurements at the end of the cooling stage which give information on the atomic cloud temperature; atomic density; and phase-space-density could not be taken as well. Therefore, in this chapter we mainly give the details of the various optical and electronic components of our setup that we built keeping in mind the different stages of our experiment, which are briefly discussed in §. 3.1.

As discussed in Chapter. 2, it is not possible to directly implement the sub-Doppler schemes on a gas of thermal atoms due to the low capture velocity range. To enhance the atom number and density, a typical cooling cycle begins with loading warm atoms onto a magneto-optical-trapping (MOT) stage followed by a molasses stage. A typical MOT stage (§. 3.7) consists of first collecting atoms into a two-dimensional MOT (2D-MOT) wherein atoms are slowed down in two directions and move freely along the third. This produces a flux of collimated atomic beam. The collimated atoms are then transferred into a three-dimensional MOT (3D-MOT) generally operated under an ultra-high vacuum environment, wherein cooling occurs in all three directions. After the 3D-MOT stage, the magnetic fields are switched off and atoms are further cooled in the molasses phase. During this phase, the cooling and repump intensities are ramped down while the detunings are increased (Eqn. 2.7). For  $^{39}\text{K}$ : we will implement the 2D - 3D MOT on the D2-line. The gray molasses will be implemented on the D1-line and enhanced cooling is expected under the Raman resonance condition.

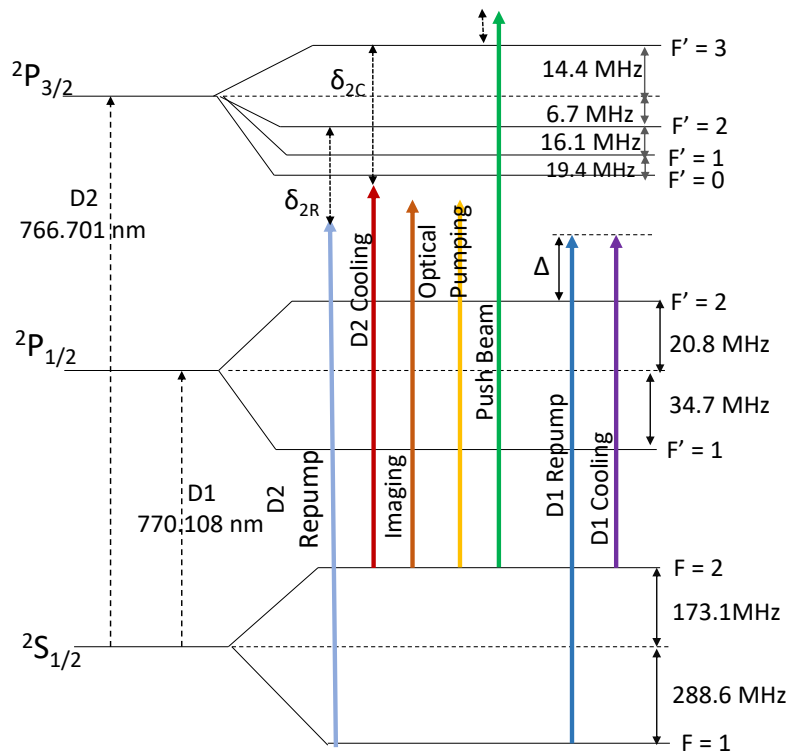


FIGURE 3.1: Energy level Diagram of  $^{39}\text{K}$  with marked transitions over a complete cooling sequence for achieving quantum degeneracy. The MOT, optical pumping and imaging stages are implemented by generating the required frequencies using transitions on the D2 line. D1 line transitions are required to achieve enhanced laser-cooling via Gray Molasses. The optimum detunings associated with each transition would have to be estimated experimentally.

### 3.1 Atomic Transitions Needed In Our Experiment

In Fig. 3.1, we show the energy level scheme of  $^{39}\text{K}$ , with marked transitions on the D2 (767 nm) and D1 (770 nm) lines that are needed during a complete cooling cycle. A complete cycle would include not only the laser cooling stage but also stages that lead to quantum degeneracy such as confining atoms into magnetic or optical dipole traps followed by evaporative cooling in each trap. Magnetic trapping (MT) and Optical dipole trapping (ODT) are done after the atoms have been laser-cooled and as such the optical setup for loading cold potassium atoms into these traps is the same as that described in [22] for  $^{87}\text{Rb}$  atoms and hence, can be directly used. Here, we focus primarily on the optics required for implementing the laser-cooling phase.

The 2D and 3D MOT cooling and repump beams are generated on the D2-line and are both red-detuned from  $F = 2 \rightarrow F' = 3$  and  $F = 1 \rightarrow F' = 2$

transitions respectively. However, due to the narrow spacing among the excited hyperfine levels, it is not possible to be precisely detuned from a single level and hence in a practical setting, the beams are effectively red-detuned from the entire excited manifold. The standard MOT beam configuration of  $\sigma^+ - \sigma^-$  will be used. To transfer the collimated atoms from the 2D-MOT chamber to the 3D-MOT chamber, a ‘push-beam’, blue-detuned to the  $F = 2 \rightarrow F' = 3$  transition will be used. At the end of 3D-MOT stage, a sub-Doppler molasses phase on the D2 line can be implemented using the same cooling and repump beams albeit with different intensities and detunings. To reduce the temperature further from here, the D2 beams can be turned off and the D1 beams turned on thereby implementing a pure Gray molasses phase on the D1 line. Here, the cooling and repump beams are blue-detuned from  $F = 2 \rightarrow F' = 2$  and  $F = 1 \rightarrow F' = 2$  transitions respectively. To estimate the number of trapped atoms in the atomic cloud during the MOT or the molasses phase, an absorption imaging technique will be used. The imaging beam in our case should be nearly resonant to the  $F = 2 \rightarrow F' = 3$  transition on the D2 line and a precise value would need to be determined experimentally. The same imaging technique would also be used to estimate the temperature of the atomic cloud using time-of-flight measurements. Completion of D1 molasses would mark the end of the laser-cooling phase, after which, the atoms would have to be transferred to the magnetically trappable  $F = 2, m_F = 2$  state. This can be achieved by optical pumping, using a  $\sigma^+$  beam nearly resonant to  $F = 2 \rightarrow F' = 2$  transition. Again, the level structure makes it difficult to isolate a single excited level, hence, the effective detuning can be optimized only when the actual cooling sequence is carried out.

## 3.2 Overview of Optical Setup

The layout of our laser system for cooling  $^{39}\text{K}$  is shown in Fig. 3.2. An overview is presented here and further details are given in Sections. 3.3, 3.4, 3.5 and 3.6. Our optical setup has three lasers: two diode lasers (TOPTICA: DL100) at operating wavelengths of 767 and 770 nm, one tapered-amplified laser at 767 nm wavelength (TOPTICA: TA PRO). With each laser comes the associated control circuitry (TOPTICA DLC PRO) for scanning the piezo-transducer, driving the injection current and maintaining the temperature of the laser diode chips. The output power measured from the diode lasers is at 75 mW while that from TA PRO is 1.7 W. These values refer to power after the isolator stage. Repump beams for the 2D and 3D MOT stages on the



D2 line are generated from the corresponding diode laser (hereafter, referred to as **D2-repump**). The TA PRO laser is used for generating cooling beams for 2D and 3D MOT as well as other transitions on the D2 line: push beam, imaging and optical pumping (hereafter, referred to as **D2-cooling**). Both the cooling and repump beams on the D1 line are generated from a single DL 100 laser (hereafter, referred to as **D1-laser**) with the frequency separation obtained using an electro-optic modulator (**QUBIG:EO-K39M3-NIR**). The diode lasers are frequency stabilized using saturated absorption spectroscopy (§. 3.3.1) and the TA PRO laser is frequency stabilized using beat note locking, where the beat frequency is calculated between the two 767 nm lasers (§. 3.5). Additional optical paths are provided for wavelength monitoring and Fabry-Perot Interferometry. In order to have sufficient power, beams from the two diode lasers are first amplified using a tapered amplifier chip (**TOPTICA: BOOSTA**) before each of them is frequency shifted for generating the required transitions (shown in Fig. 3.1). This is done by combining the two wavelengths at the input stage of the BOOSTA using an interference filter (**SEMROCK: LD01-785/10-12.5**). The amplified output then consists of both the wavelengths, which can be separated using another such filter. We use interference filters at several other points in our setup to combine two different wavelengths, as for example, D1-D2 cooling and repump beams; push-beams at 767 nm ( $^{39}\text{K}$ ) and 780 nm ( $^{87}\text{Rb}$ ). The two push beams need to be combined since both Rb and K would share the same 'science chamber' [22]. Frequency shifts for various transitions (Fig. 3.1) is done using acousto-optic modulators (**IntraAction Corp : ATM-801A2**) in either a single or double-pass AOM configurations. To improve the coupling efficiencies of laser beams with fiber-couplers, AOM's etc, beam waists are collimated using telescopic arrangements.

### 3.3 Frequency Stabilization of our Diode Lasers

As in any experiment in atomic physics, locking lasers to a well-defined frequency and minimizing the frequency jitter is crucial to our experiments. Our diode lasers are frequency stabilized using saturated absorption spectroscopy technique (SAS). The absolute frequency reference in each case is chosen from one of the atomic transitions between the hyperfine levels. In the following subsection, a general description of the SAS technique along with its utility in laser frequency stabilization is presented. We illustrate this

technique by presenting the experimentally measured saturated spectrum of both D1 and D2 lines in  $^{39}\text{K}$ .

### 3.3.1 Saturated Absorption Spectroscopy

We consider a gas of atoms inside a vapour cell, which is heated above room temperature (for our experiment, the K vapour cell temperature is  $\approx 62^\circ\text{C}$ ). These warm atoms follow the Maxwell-Boltzmann velocity distribution. If we consider a laser beam propagating along the  $+z$  axis, then an atom that has a non-zero velocity component  $v_z$  in the  $z$  direction would effectively absorb radiation of frequency  $\omega_L$  given by:

$$\omega_L = \omega_0 \left(1 + \frac{v_z}{c}\right) \quad (3.1)$$

where  $\omega_0$  is the resonant absorption frequency for an atom at rest and  $c$  is the speed of light. Since the positive  $z$ -axis points along the direction of laser propagation, we see that atoms moving towards the laser ( $v_z < 0$ ) will resonantly absorb radiation frequency  $\omega_L < \omega_0$ . Thus,  $\omega_L$  is blue-shifted to  $\omega_0$  due to Doppler effect. Likewise, atoms moving away from the laser beam see the frequency red-shifted. If we scan the laser frequency across an atomic resonance, a wide range of laser frequencies will be absorbed due to the random motion of the ensemble of thermal atoms. This effect, which tends to mask the more subtle features of an absorption spectrum (such as hyperfine transitions) is known as Doppler broadening (Fig. 3.4a).

Saturation spectroscopy [31, 18] is a high-resolution spectroscopy to circumvent Doppler broadening. The optical setup implemented in our experiment is shown in Fig. 3.3. Two counter-propagating laser beams derived from a single source are sent through a K-vapour cell. One of the beams is of high intensity, known as the 'pump' beam while the other low intensity beam is called the 'probe' beam. The probe spectrum is measured using a photo-detector. In our experiment, we used a probe beam five to ten times less intense than the pump beam. The frequency of pump beam is shifted using an acousto-optic-modulator (AOM) in a double-pass configuration. The same AOM is also used to dither the frequency of the pump beam, while scanning the laser frequency, so as to obtain 'derivatives' of spectral features that are being scanned. These derivatives contain information about the deviation of laser frequency from resonance and are discussed in §. 3.3.4. To first understand the principle of SAS, we assume for simplicity that both probe and pump beams have the same frequency i.e. the pump beam can be thought

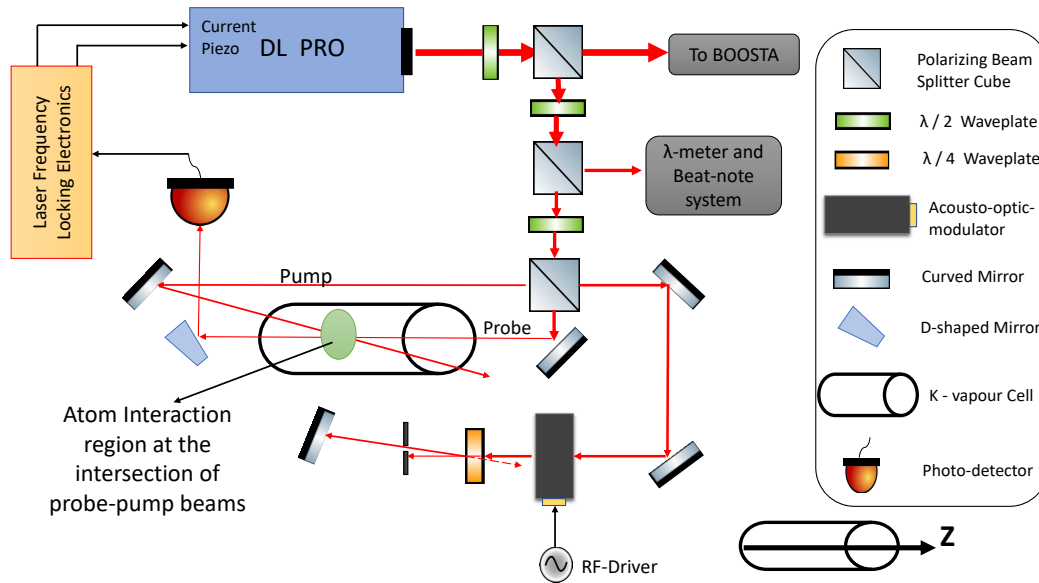


FIGURE 3.3: Schematic of our saturated absorption spectroscopy setup, used to frequency stabilize our D2 repump laser. A similar setup is used for D1 laser (Fig. 3.2). The weak probe and strong pump beams are aligned so as to have maximum overlap inside the vapour cell. The angle between the two beams is exaggerated in this figure. Pump beam is frequency shifted using a double-pass AOM scheme. The same AOM is used to frequency modulate the pump so as to generate derivatives of spectral features while scanning the laser frequency. This derivative signal is electronically processed to generate feedback correction signals for laser frequency.

of as  $0^{th}$  order of the AOM. If the laser is off resonance, then both the counter-propagating probe and pump beams get absorbed by atoms of different velocity classes. However, when the laser is on resonance, they shall interact with the class of atoms whose velocity component along the axis of beams is zero (eg:  $v_z = 0$ ). This is the heart of saturation spectroscopy: when the laser is on resonance with the  $v_z = 0$  class of atoms, there is a sharp decrease in absorption of probe beam (seen as a sharp increase in the signal intensity transmitted to the detector). This happens because many of the atoms in the common velocity class are pumped out of the ground state by the intense pump beam, and hence, do not absorb any photons from the resonant probe beam. Note that this only happens because the pump and probe are interacting with the same velocity class of atoms: in this case those with  $v_z = 0$ . If the laser is off resonance, this feature is not present, and the spectrum will not contain sub-Doppler features. If we slowly scan the laser frequency across the atomic resonance, then we expect to see at the detector, a Doppler

broadened probe absorption with sharp peaks riding on top of the signal corresponding to hyperfine transitions (see figure. 3.4 (b,c)). This is the saturated spectrum !

### 3.3.2 Ground and Excited Crossover Transitions in saturated spectroscopy

Crossover dips are an important feature of a saturated absorption spectrum. **Excited state crossovers** occur when two excited levels (say  $|e_1\rangle$  and  $|e_2\rangle$ ) share a common ground level ( $|g\rangle$ ) and the separation between those excited levels is less than the Doppler linewidth. Let the transition frequencies from  $|g\rangle$  to  $|e_1\rangle$  and  $|e_2\rangle$  be  $\omega_1$  and  $\omega_2$  respectively. For a laser with frequency  $\omega_L$  such that  $\omega_1 < \omega_L < \omega_2$ , there will be atoms with velocity  $v_{z1}$  for which the pump frequency is red-shifted to  $\omega_1$  and atoms with velocity  $-v_{z2}$  for which it is blue-shifted to  $\omega_2$ . Similarly, the probe beam would interact with atoms with velocities  $-v_{z1}$  and  $+v_{z2}$  with probe frequency red-shifted and blue-shifted to  $\omega_1$  and  $\omega_2$  respectively. Hence, each of the probe and pump beams shall interact with two different classes of atoms at the same time. Clearly, there will be some laser frequency  $\omega_C$  for which the same group of atoms are resonant at  $\omega_1$  with the probe and  $\omega_2$  with the pump. There would be another class of atoms resonant at  $\omega_1$  with the pump and  $\omega_2$  with the probe. In both the cases, the intense pump beam depletes the atoms in the ground state thereby leading to dip in the probe absorption. The crossover frequency  $\omega_C$  can be shown to be equal to  $(\omega_1 + \omega_2)/2$ .

Alkali atoms like Rb, Cs and Na have multiple crossover dips in their saturated absorption spectrum with each feature occurring at a crossover frequency lying midway between two excited levels. In these atoms, the ground hyperfine levels lie outside the Doppler linewidth (eg:- In Rb, room temperature Doppler width is 561 MHz whereas the ground hyperfine levels are 6.83 GHz apart). In contrast, isotopes of K and Li have ground state splitting smaller than their Doppler linewidths (eg:-  $^{39}\text{K}$  has a Doppler width of  $\approx 800$  MHz at room temperature while the ground state levels are separated by 461 MHz). As shown in figures. 3.4 (b,c), the D2 and D1 spectra of  $^{39}\text{K}$  exhibit spectral features lying midway between the absorption features that correspond to excited state transitions of the two hyperfine levels. These features are inverted i.e. show an increased absorption of probe beam in the presence of pump. Such spectral features correspond to **crossover transitions between ground states**: they occur when two ground states share a common

excited state and the ground states separation lies within the Doppler width. For  $^{39}\text{K}$ , the crossover frequency in the ground state  $\omega_{\text{CG}}$  can be given as  $(\omega_1 + \omega_2)/2$  where  $\omega_{1,2}$  are the transition frequencies from  $F = 1$  and  $F = 2$  to a common excited level. An explanation for increased probe absorption at this frequency is as follows: at  $\omega_L = \omega_{\text{CG}}$ , there would be a common velocity class resonant at  $\omega_1$  with the pump and  $\omega_2$  with the probe. The pump beam being at higher intensity, optically pumps this class of atoms from the  $F = 1$  to  $F = 2$  ground state. At  $F = 2$ , the atoms interact with the resonant probe and hence there is more absorption. There would be another class of atoms resonant at  $\omega_1$  with probe and  $\omega_2$  with pump. These atoms are optically pumped to  $F = 1$  ground state where they again interact with probe, leading to absorption.

### 3.3.3 Saturated Spectrum for D1 and D2 lines in $^{39}\text{K}$

Possible transitions in the saturated absorption spectrum of  $^{39}\text{K}$  are shown in table 3.1. Based on Fig. 3.1, transitions connecting  $F = 1 \rightarrow F'$  can be used for generating a repump beam while those connecting  $F = 2 \rightarrow F'$  can be used for generating a cooling beam.

Transitions of the form  $2 \rightarrow 12$ ,  $1 \rightarrow 12$  etc. are the excited state crossovers and, if properly resolved, appear as peaks in the probe transmission spectrum on the corresponding cooling and repump lines. On the other hand, transitions of the form  $12 \rightarrow 1$ ,  $12 \rightarrow 2$  indicate ground state crossovers and appear as dips in the probe transmitted intensity. It is worthwhile mentioning that due to narrow hyperfine splitting in the excited states ( $^2P_{3/2}$  and  $^2P_{1/2}$ ), not all peaks shown in the table are resolved using spectroscopy techniques. As shown in Fig. 3.4, our measured D2 spectrum shows two single unresolved peak features corresponding to  $4^2S_{1/2}, F = 2 \rightarrow 4^2P_{3/2}$  (cooling line),  $4^2S_{1/2}, F = 1 \rightarrow 4^2P_{3/2}$  (repump line) and one unresolved dip that corresponds to a ground state crossover at  $4^2S_{1/2}, F = 12 \rightarrow 4^2P_{3/2}$  transition. The individual peaks / dips in each of these features are masked due to narrow separation among various transitions (see table 3.1). *This further supports our claim that individual  $F \rightarrow F'$  transitions are difficult to isolate on the D2 line.* D1 spectrum is better resolved when compared to D2: all three dips of the ground state crossover feature are visible; a strong transition is also observed at  $F = 2 \rightarrow F' = 12$  excited state crossover on the cooling feature. The repump feature, however, is not well-resolved and appears as a single peak in the spectrum.

D1-line transitions		D2-line transitions	
F $\rightarrow$ F'	Detuning (MHz)	F $\rightarrow$ F'	Detuning (MHz)
2 $\rightarrow$ 1'	-207.9	2 $\rightarrow$ 1'	-189.1
2 $\rightarrow$ 1'2'	-180.1	2 $\rightarrow$ 1'2'	-184.45
2 $\rightarrow$ 2'	-152.3	2 $\rightarrow$ 2'	-179.8
12 $\rightarrow$ 1'	22.95	2 $\rightarrow$ 2'3'	-169.3
12 $\rightarrow$ 1'2'	50.75	2 $\rightarrow$ 3'	-158.8
12 $\rightarrow$ 2'	78.55	12 $\rightarrow$ 0'1'	40.15
1 $\rightarrow$ 1'	253.8	12 $\rightarrow$ 1'	41.75
1 $\rightarrow$ 1'2'	281.6	12 $\rightarrow$ 0'2'	44.8
1 $\rightarrow$ 2'	309.4	12 $\rightarrow$ 1'2'	46.4
		12 $\rightarrow$ 2'	51.05
		12 $\rightarrow$ 1'3'	56.9
		12 $\rightarrow$ 2'3'	61.55
		1 $\rightarrow$ 0'	269.4
		1 $\rightarrow$ 0'1'	271
		1 $\rightarrow$ 1'	272.6
		1 $\rightarrow$ 1'2'	277.25
		1 $\rightarrow$ 2'	281.9

TABLE 3.1: Calculated transitions on D1 and D2 lines of  $^{39}\text{K}$ , expected in a saturated absorption spectroscopy. Adapted from [32]. The levels denoted with ' refer to excited states. **Left:** D1-line transitions ( $4^2S_{1/2} \rightarrow 4^2P_{1/2}$ ). The detuning values are with respect to center frequency  $\omega_0$  at 770.108 nm. **Right:** D2-line transitions ( $4^2S_{1/2} \rightarrow 4^2P_{3/2}$ ), where detunings are with respect to  $\omega_0$  at 766.701 nm. As evident, the separation between various hyperfine transitions on the cooling, repump or ground crossover is of the order of natural linewidth and as such quite challenging to individually resolve using SAS.

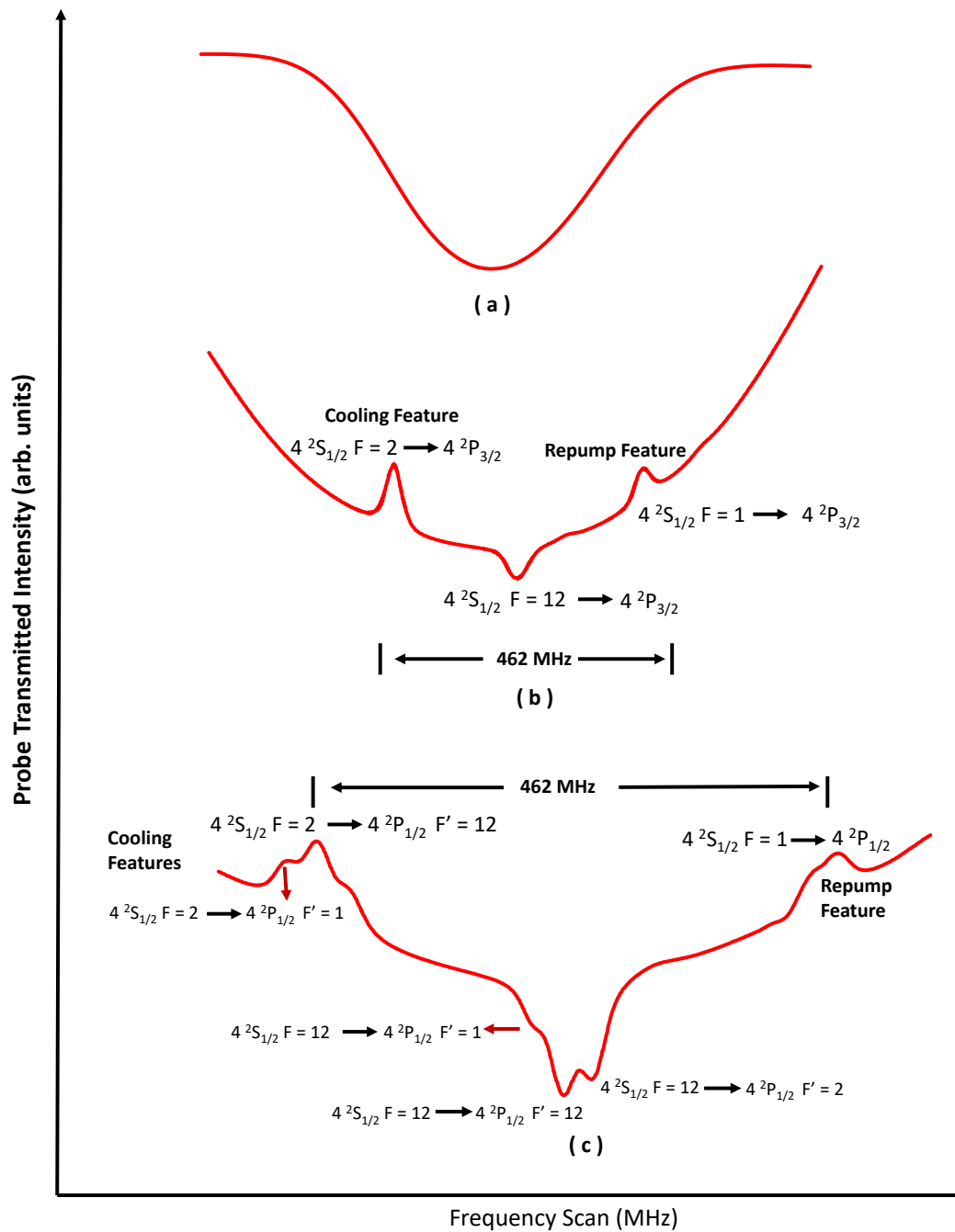


FIGURE 3.4: Measured D2 and D1 spectrum using SAS. **(a)** Doppler-broadened probe absorption. **(b)** Saturated absorption features on the D2 line. Although, cooling, ground crossover and the repump features are visible in the otherwise broadened spectrum, those features by themselves are not resolved into individual peaks and dips. **(c)** Saturated absorption features on the D1 line. D1 features are somewhat better resolved compared to their D2 counterparts: On the cooling feature, the excited crossover transition is clearly visible; All three ground crossover transitions are resolved. The repump transitions remain unresolved.

### 3.3.4 Using SAS for laser frequency locking

1. **Shifting the Pump frequency:** In our SAS setup's, the pump beam passes through a double-pass AOM stage such that it is up-shifted in frequency by an amount equal to twice the AOM frequency. We set our AOM's at carrier frequency of 80 MHz for both our SAS setup's. Therefore, our probe frequency  $\omega_{\text{probe}}$  is set at laser frequency  $\omega_L$  while the pump frequency  $\omega_{\text{pump}}$  is up-shifted to  $\omega_L + 2\omega_{\text{AOM}}$ . In the laboratory frame, there would be some velocity class of atoms that would be resonant to both the pump and probe frequencies, in that, one of them is red-shifted while the other is blue-shifted. With reference to Fig. 3.5, the laser frequency for such a velocity class can be derived as:

Assuming the velocity to be along positive  $z$  direction, probe beam would be resonant if:

$$\begin{aligned}\omega_0 &= \omega_{\text{probe}} + kv \\ &= \omega_L + kv\end{aligned}$$

where  $\omega_0$  is an atomic transition frequency and  $kv$  is the Doppler blue-shift. Similarly, the pump beam would be resonant to the same velocity class if :

$$\begin{aligned}\omega_0 &= \omega_{\text{pump}} - kv \\ &= \omega_L + 2\omega_{\text{AOM}} - kv\end{aligned}$$

This gives the laser frequency as:

$$\omega_L = \omega_0 - \omega_{\text{AOM}} \quad (3.2)$$

Hence, in our saturated spectroscopy setup, diode lasers when 'locked' to a particular transition ( $\omega_0$ ), are red-detuned from resonance by an amount equal to the AOM carrier frequency, which is 80 MHz in our case.

2. **Modulation of Probe Signal:** Besides frequency shifting, the same AOM can also be used to add a frequency dither to the pump beam. This is achieved by frequency modulating the carrier signal of the AOM, with a modulation frequency much smaller than that of the carrier. In our setup, a modulating signal with frequency  $\omega_D$  between 15-25 kHz is

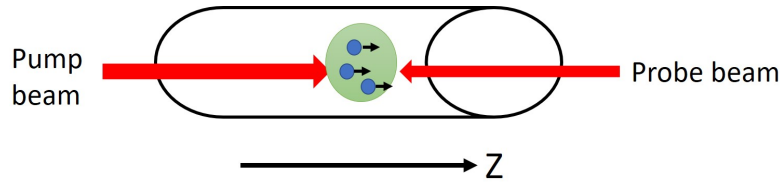


FIGURE 3.5: Conceptual schematic for laser frequency absorbed by a velocity class of atoms that see both probe and a shifted pump beam.

applied on the 80 MHz carrier frequency. This in turn causes a variation in the frequency of the pump beam. The frequency deviation is proportional to the amplitude of modulating signal. Modulation of the pump also changes which velocity class of atoms shall resonantly interact with both the probe and the pump beams. That means, the probe frequency 'resonantly' seen by the atoms also changes, depending on which velocity class is being pumped, and this change occurs at the same rate as  $\omega_D$ . In other words, modulations imposed on the pump, are mapped to the probe spectrum as well.

If we now slowly scan the laser frequency across resonance and monitor the probe absorption on a photo-detector, we would observe the absorption signal to be frequency modulated as well. This is illustrated in Fig. 3.6, whereby a saturated-spectroscopy feature is shown as a function of laser frequency sweep, with a fast modulation superimposed on it. In our experiment, the scan signal is a slowly varying triangular signal (typical frequency: 0.5 Hz) that is applied to the piezo input of the laser. The modulating signal on the other hand is a sinusoid with frequency  $\omega_D$  of the order KHz. Thus, the probe frequency oscillates around a given laser frequency (which is set by the scan voltage), such that the frequency deviation from the laser frequency is proportional to the amplitude of modulating signal while the rate at which it oscillates around this laser frequency is given by the modulation frequency. Now, as absorption of the probe beam is a function of probe frequency, what we observe on the detector is a modulated probe intensity. The amplitude of this intensity modulation depends on how much the absorption changes as a function of probe frequency and thus, is proportional to the slope of the spectroscopic feature. In other words, *the envelope of modulated probe signal is the derivative of the spectroscopic feature*. This derivative contains two important pieces of information: (1) The sign of the derivative signal indicates which side the laser frequency is with

respect to resonance. A positive value indicates a rising slope of absorption curve, implying laser frequency to be on the left side of  $\omega_0$ , that is below resonance. A negative value would indicate a falling slope, implying laser is above resonance<sup>1</sup>. This is also evident from Fig. 3.6, that the modulations in probe amplitude are 180 degrees out of phase on either side of resonant frequency. (2) The magnitude of derivative signal is a measure of the deviation from resonant frequency. At  $\omega_L = \omega_0$ , the derivative equals zero and the modulations in probe intensity are absent. When the laser deviates from resonance, the derivative has a finite value. Far from resonance, the spectroscopic feature itself is absent and thus, the derivative is again zero. Both the sign and magnitude of the derivative can hence be used in locking the laser to a particular frequency of interest. The important part is to be able to extract this signal from the modulated probe signal, which is done electronically.

The key points of the above discussion, in a nut shell are: Modulating the pump frequency using AOM also induces modulations in probe frequency. The envelope of the frequency modulated probe signal is the derivative of the spectroscopic features. By electronically extracting this derivative signal from the modulated probe spectrum, one can generate feedback control signals to get the laser locked onto the frequency of interest. We next describe how, well known techniques such as lock-in detection [33] can be used for this very purpose.

- 3. Demodulation of Probe signal using Lock-In Detection:** Lock-in detection involves demodulation of the probe spectrum so as to extract the amplitude as well as phase of the envelope of the modulated probe signal. The extracted signal is the derivative of the spectroscopic feature which, as discussed before, can be used in laser frequency stabilization. Demodulation is done using a 'lock-in amplifier', also called a phase-sensitive detector. This amplifier primarily comprises of an internal oscillator / signal generator, a mixer circuit and a low pass filter circuit. The internal oscillator generates the modulation signal to dither the carrier frequency of the AOM (the same AOM that shifts the frequency of the pump beam). The atomic response to this dither is in the form of a modulated probe signal, which is one of the inputs to the mixer circuit. The second input applied to the mixer circuit is a phase-shifted version

---

<sup>1</sup>These interpretations are valid for features that give 'peaks' in the saturated spectrum. For ground state crossover transitions, a positive slope shall imply that laser is on right side of resonance and vice versa for negative slope.

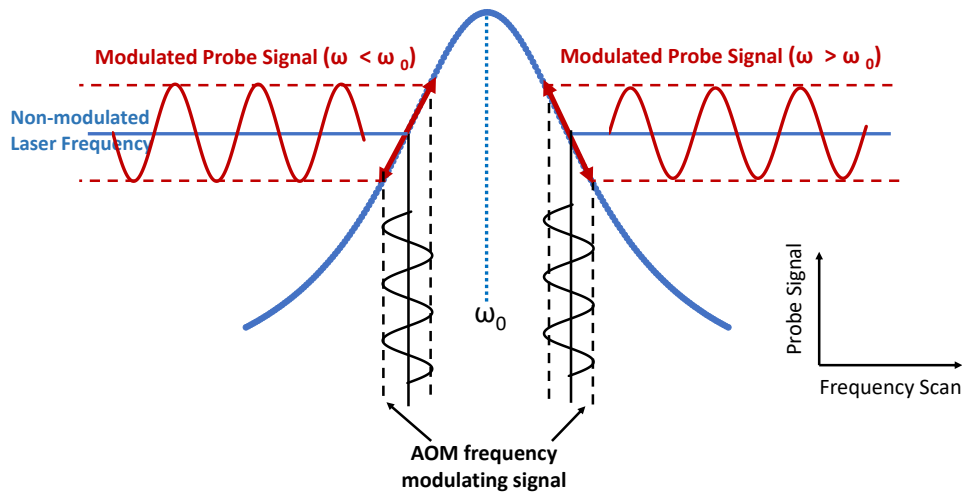


FIGURE 3.6: A conceptual scheme showing modulation of probe signal by frequency dithering the pump beam, in a saturated absorption setup. The blue trace is a theoretical curve corresponding to some spectroscopic feature of the probe and obtained by a slow frequency scan. The black traces correspond to fast modulations in the probe that occur around a given laser frequency. As the probe frequency oscillates up and down around a given frequency, so does the probe intensity, resulting in a frequency modulated probe signal. These are shown by the brown trace. The amplitude of oscillations are proportional to the slope of the spectroscopic feature. As shown, the modulations on either side of the resonant frequency  $\omega_0$  are 180 degrees out of phase. At the resonant frequency, the slope of the absorption line is zero and hence the modulations are also absent.

of the same AOM modulation signal. The second input is called the ‘reference signal’. The reference and the modulated probe signal get multiplied in the mixer and the output is passed through the low pass filter such that only the DC component remains. *The filtered output is the derivative signal of interest.* A block diagram for lock-in detection is shown in Fig. 3.7. With reference to this figure, the modulated carrier frequency of the AOM is given by:

$$\omega_{\text{AOM}} = \omega_C + \beta A_M \sin(\omega_D t)$$

Here  $\omega_C$  is the unmodulated carrier frequency (80 MHz in our setup) and  $\beta$  is the modulation index. The modulating sine wave is generated in the lock-in amplifier unit, with amplitude and frequency given by

$A_M$  and  $\omega_D$  respectively. These modulations appear in the probe absorption spectrum as well, with the frequency-dependent, transmitted probe intensity  $X(\omega)$  given by:

$$\begin{aligned} X(\omega) &= X(\omega_L + \beta A_M \sin(\omega_D t)) \\ &= X(\omega_L) + X'(\omega_L) \beta A_M \sin(\omega_D t) \end{aligned}$$

where first order Taylor expansion was done on  $X(\omega)$  by using the fact that  $|\omega_L| \gg \beta A_M$ . This signal is then multiplied (mixed) with the reference signal. For coherent detection, the reference signal must have the same frequency as the modulating signal. Denoting the reference signal amplitude as  $A_R$  and the phase difference between the reference and modulating signals as  $\Phi$ , the mixer output  $M$  is:

$$\begin{aligned} M &= X(\omega) \times A_R \sin(\omega_D t) \\ &= \left( X(\omega_L) + X'(\omega_L) \beta A_M \sin(\omega_D t) \right) \times A_R \sin(\omega_D t + \Phi) \\ &= A_R X(\omega) \sin(\omega_D t + \Phi) + \beta A_M A_R X'(\omega_L) \sin(\omega_D t) \sin(\omega_D t + \Phi) \\ &= A_R X(\omega) \sin(\omega_D t + \Phi) + \frac{1}{2} \beta A_R A_M X'(\omega_L) \left( \cos(\Phi) + \cos(2\omega_D t + \Phi) \right) \end{aligned}$$

The mixer output contains a DC component and two high-frequency components. Higher terms are filtered out through the low pass filter stage (filter cut-off frequency  $\ll \omega_D$ ). The DC portion that remains, corresponds to the component in the probe spectrum at the modulation frequency, and is given by:

$$Y = \frac{1}{2} \beta A_R A_M X'(\omega_L) \cos(\Phi) \quad (3.3)$$

The final output of the lock-in detection, as seen from Eqn. 3.3, is proportional to the derivative of the absorption feature. Zero crossings of this signal correspond to resonant frequencies. By properly adjusting the laser scan, one can zoom in on a spectral feature that is of interest and observe the corresponding lock-in amplifier output. In the context of electronic control systems, this lock-in output is popularly called an 'error signal', in that it corresponds to the deviation of laser frequency from resonance. The error signal is then taken by electronic controllers to generate appropriate feedback for mechanical (eg: diffraction grating) and / or electrical (eg: current) components of the laser to keep the laser frequency constant.

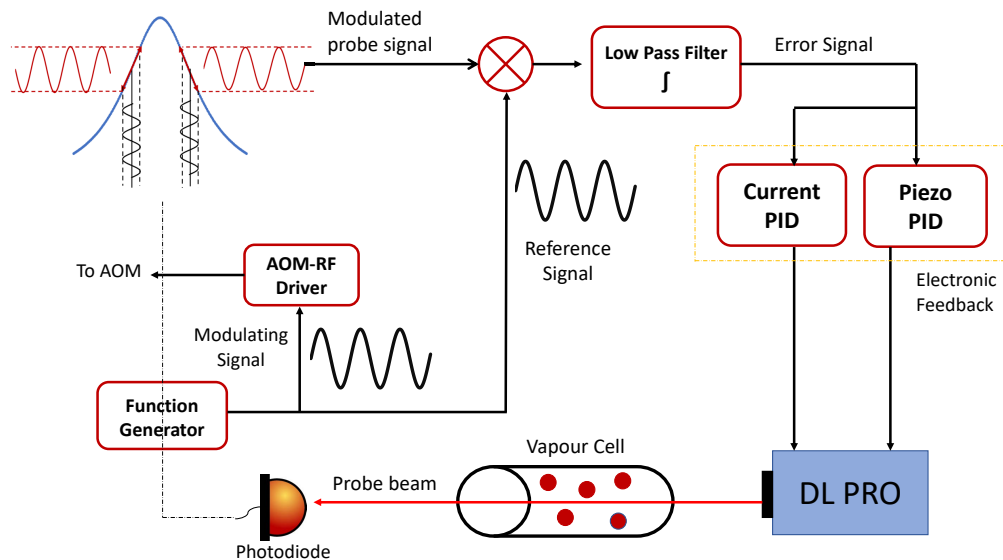


FIGURE 3.7: Demodulation of probe signal to extract the derivative / error signal. Not shown in the figure is the frequency shifting of pump beam, done using an AOM in a double-pass configuration (see Fig. 3.3). The frequency dither of this AOM-carrier frequency is achieved by applying an external signal as an input to the frequency modulation (FM) unit of the RF-driver that controls the AOM. Consequently, this results in the intensity modulation of the saturated features in the probe spectrum, with modulations occurring at the frequency of the external (modulating) signal. By multiplying the modulated probe with a reference signal (which is the phase-shifted version of the modulating signal and has the same frequency as the modulating signal), followed by suitable filtering, we can extract the derivative of spectroscopic features. The derivative is proportional to both the amplitude of modulating signal as well as the phase difference between modulating and the reference signal. Further, the modulating and the reference signals are generated from the same oscillator, hence the detection is coherent. The extracted derivative signal, also called the 'error signal', can be used by active PID based servo controllers to lock the laser frequency onto a chosen spectroscopic feature. Typical frequency control requires both fast and slow correction to the laser frequency. These corrections are applied to laser current and piezo respectively. In this way, a closed feedback loop scheme is achieved.

4. **Active Feedback Frequency Control:** Our D1 and D2 lasers are semiconductor based extended cavity diode lasers (ECDL), with their operating wavelengths set by: (1) the position of the diffraction grating that determines the length of the external cavity. Which longitudinal frequency-modes would be excited inside the cavity, depends upon the length of the cavity itself. The grating position and hence the cavity length can be modified by applying an electrical signal to the piezoelectric transducer (that is attached to the grating), thereby changing the laser frequency. (2) Injection current that flows through the active region (gain medium) of the laser diode. Changing the injection current changes the gain-profile of the active medium. Since the frequency-modes that are sustained inside the laser cavity are the convolution of the gain profile of the laser-current, the external-cavity and the internal-cavity of the laser diode, the laser frequency changes upon change in injection current.<sup>2</sup> An “active frequency stabilization”, therefore, refers to sending appropriate electronic feedback to both the piezo and the current components of the laser so as to maintain the frequency to the desired value (more precisely, keeping jitter around the center frequency as low as possible). The basic idea behind any electronic controller is this: to minimize the deviation of a physical variable, which is the output of the system (temperature, intensity, frequency, displacement.....etc.) with respect to the desired output value (‘reference’) by modifying the actuator (process) that drives the output. In the context of laser frequency stabilization via saturated spectroscopy, the desired output laser frequency (reference) corresponds to the spectroscopic features due to the hyperfine transitions (Fig. 3.4); the lock-in output signal obtained in Eqn. 3.3 is the measure of deviation from the reference frequency; the piezo voltage / current act as actuating signals. The feedback controllers used in our experiment are the ubiquitous proportional-integral-derivative (PID) type [34]. The PID loop generates correction signals in such a way so as to keep the error signal zero or near-zero (the zero crossing corresponds to resonant frequency). The correction to laser frequency using a mechanical piezoelectric transducer is a slow correction (as the piezo has some inertia), while that due to current is a fast correction. Hence, two PID controllers of different bandwidths, one for piezo (slow PID) and the other for current (fast PID) are employed.

---

<sup>2</sup>The operating wavelength is also dependent on the temperature of the laser diode and for stable operations, this temperature must be stabilized.

### 3.4 Locking the D1 and D2 diode lasers

To observe the saturated-absorption features on the D1 and D2 lines, we first set the wavelengths of the two diode lasers close to the corresponding D2 and D1 transition wavelengths. This is done by adjusting both the laser-diode injection-current as well as the DC voltage applied to the piezoelectric transducer, while monitoring the laser wavelength on the wavelength-meter. As mentioned earlier, the former changes the gain-profile of the active medium in the semiconductor diode while the latter changes the length of external cavity. Our wave-meter (**Bristol Instruments**) is precise to one-thousandth of a nanometer. The measured wavelengths and the corresponding current and piezo-voltages are given in tables 3.2 and 3.3. The laser frequency can be ‘scanned’ by applying a triangular ramp signal on top of the DC offset voltage that drives the laser piezo. We measured the frequency to voltage sensitivity of our Toptica lasers to be approximately 400 MHz / V, i.e. a 1 V ramp signal would scan the laser frequency by about 400 MHz around the center frequency that was set by the DC offset voltage.

The optical setup for implementing SAS technique is shown in Fig. 3.3. If we block the pump beam and monitor the absorption of the probe after passing through the vapour-cell by scanning the laser frequency, we see a Doppler-broadened probe absorption, as shown in Fig. 3.4(a). The depth of absorption is related to the density of K atomic vapour which is controlled via the temperature of the vapour-cell, while the linewidth is dictated mainly by the Doppler-broadening. In the presence of the pump beam (having a high intensity relative to the probe beam), SAS features occur on the otherwise Doppler-broadened spectrum. The probe-pump powers optimised for our setups are given in the tables. If the probe power is high, the spectrum can get power-broadened leading to poorly resolved SAS features. Figures 3.8 (a,c) show the measured SAS features on the D1 and D2 lines of  $^{39}\text{K}$  along with the error / derivative signals for each feature.

In order to lock the laser frequency to the feature of interest, we can adjust the DC offset (also called ‘scan offset’) and the scan amplitude values such that only the desired feature is centered within the scan (Fig. 3.8 (b,d)). At this point, the scan is disabled while the PID loops are engaged. The PID controllers force the error signal to zero volts ( $\pm$  few tenths of mV around 0) and try to maintain this value. The zero error signal corresponds to the resonant frequency of the lock feature and hence, laser is ‘locked’ to this resonance.

We lock our D2-repump diode laser to the feature that corresponds to  $|^2S_{1/2}, F = 1\rangle \rightarrow |^2P_{3/2}\rangle$  transition. Similarly, the D1 laser is locked to the  $|^2S_{1/2}, F = 2\rangle \rightarrow |^2P_{1/2}, F' = 12\rangle$  transition which is the excited state crossover feature. The frequencies of the D2-repump and D1 lasers locked to such atomic transitions can be calculated in the following way:

Let  $\omega_R^{D2}$  denote the frequency of the  $|F = 1\rangle \rightarrow |F = 2\rangle$  transition (repump) on the D2 line. From the table 3.1:

$$\omega_R^{D2} = \omega_0^{D2} + 281.9 \text{ MHz} \quad (3.4)$$

Here  $\omega_0^{D2}$  is the center frequency of the D2 line (391 THz) that corresponds to  $\lambda = 766.701 \text{ nm}$ . Denoting the locked D2-repump laser frequency by  $\omega_{R,\text{laser}}^{D2}$  and using equations 3.9 and 3.2, we can write:

$$\begin{aligned} \omega_{R,\text{laser}}^{D2} &= \omega_{2R} - \omega_{\text{AOM}} \\ &= \omega_0^{D2} + 281.9 \text{ MHz} - 80 \text{ MHz} \\ &= \omega_0^{D2} + 201.9 \text{ MHz} \end{aligned} \quad (3.5)$$

where we have setup the AOM carrier frequency at 80 MHz. Eqn. 3.5 implies that the D2 repump laser is locked 80 MHz below the repump transition. However, as the individual hyperfine transition peaks are not resolved in the D2-SAS (Fig. 3.4(b)), our laser is not precisely locked with respect to the repump transition, rather to the excited D2 manifold ( $|^2P_{3/2}\rangle$ ) as a whole. Therefore, a detuning parameter  $\delta$  must also be added to  $\omega_{R,\text{laser}}^{D2}$ , which can be experimentally determined. In other words,

$$\omega_{R,\text{laser}}^{D2} = \omega_0^{D2} + 201.9 \text{ MHz} - \delta \quad (3.6)$$

We apply the same reasoning to the frequency of the D1 laser ( $\omega_{\text{laser}}^{D1}$ ) which is locked to excited crossover transition  $|F = 2 \rightarrow F' = 12\rangle$  on the D1 line:

$$\omega_{2 \rightarrow 1'2'}^{D1} = \omega_0^{D1} - 180.1 \text{ MHz} \quad (3.7)$$

where  $\omega_{2 \rightarrow 1'2'}^{D1}$  is the excited crossover frequency,  $\omega_0^{D1}$  is the center frequency of the D1 line (389 THz) that corresponds to  $\lambda = 770.109 \text{ nm}$ .

$$\begin{aligned}
\omega_{\text{laser}}^{\text{D1}} &= \omega_{1'2'} - \omega_{\text{AOM}} \\
&= \omega_0^{\text{D1}} - 180.1 \text{ MHz} - 80 \text{ MHz} \\
&= \omega_0^{\text{D1}} - 260.1 \text{ MHz}
\end{aligned} \tag{3.8}$$

It is to be noted that this crossover transition is well-resolved and hence  $\omega_{\text{laser}}^{\text{D1}}$  is precisely red-detuned by 80 MHz (AOM carrier frequency) with respect to the resonant crossover frequency.

### 3.4.1 PID Controllers: Polarity Selection

As mentioned before, in order to lock our laser frequency to the desired transition, we use a slow-PID that sends feedback to laser piezo and a fast-PID that feeds back to the laser current. ‘Slow’ and ‘fast’ refer to the bandwidth of the PID controller loops, that is, the range of frequencies over which the controller’s action is effective. In case of laser frequency stabilization, the polarity of a PID controller (positive or negative) refers to the action of the controller on the laser frequency with respect to the direction of the scan [35]. As stated in §. 3.4, we scan our laser frequency via the piezoelectric transducer. Applying a positive (negative) scan signal to the DC-offset voltage increases (decreases) the laser frequency. The correct polarity of a controller is one where an increased controller output acts in the same direction as the direction of the scan. Since, our slow PID also acts on the same piezo transducer, its polarity setting should by default be set to positive. For the case of diode injection-current, an increasing (decreasing) current results in decreasing (increasing) laser frequency (we observed this using the wavelength-meter). This suggests that the current PID polarity should be set to negative. Setting the correct polarity of both the PIDs is crucial to laser locking. The quality of a lock depends upon the slope of the error signal: the more gradual (steeper) the slope is, the easier (difficult) it is for the controller to ‘pin’ the error signal to zero. An incorrect controller polarity distorts both the spectral features and the associated error signals, in that the features get narrower as the error signals get steeper.

To determine the polarity of each controller, we compared the signals that are obtained during the regular scan (PID controller is off) with the signals obtained when the controller is on. This was done for both the controllers. In each case, only the proportional component (P) and the overall gain (G) of the

controller were given a finite value while the integral (I) and the derivative (D) contributions were set to zero. Figure 3.9 shows the effect of polarities of our current and piezo PID on the shape of the spectral feature and the corresponding error signal. The spectral and the error signals correspond to the excited crossover peak on the cooling feature of the D1 line. As can be seen from Fig. 3.9 (a), with the current-PID controller enabled, the saturated-absorption feature gets wider (narrower) with respect to the regular scan feature when the polarity is negative (positive). Correspondingly, the error signal Fig. 3.9 (b), becomes flatter (steeper). This verifies that the correct polarity of the current-PID is negative. Similar approach was followed for the slow PID (Fig. 3.9 (c,d)) whose polarity is determined to be positive.

Alternatively, the polarity of a controller can also be understood in terms of the direction of the controller's output as the error-signal deviates from zero. As an example, we consider the undistorted error-signal of Fig. 3.9(b), around the resonant feature of Fig. 3.9(a). The zero error value corresponds to laser frequency locked to the resonant frequency. If this error-signal becomes greater than zero, the laser frequency falls below resonance and hence the correction signal of the current-PID should be such that it increases the laser frequency. This means the injection current must be decreased. If the error-signal falls below zero, the laser frequency goes to the right of resonance and the applied current correction must decrease the laser frequency, thereby the injection current should increase. In other words, the current correction signal follows the direction opposite to that of the error feature and hence, the current-PID polarity is negative for the considered saturated-feature. Similarly, we can argue that the piezo-PID should have a positive polarity for the same feature. *It is also important to remember that the correct polarity is a function of the spectroscopic-feature to which we intend to lock our laser to.* Had we considered locking to the ground crossover transitions on the D1 or D2 lines, we would have to set our current controller to positive polarity and the piezo controller to negative polarity.

### 3.4.2 Choosing PID Parameters

In addition to the slope of the error-signal, the lock performance of a PID-controller also depends upon the gain settings of the proportional (P), integral (I), derivative (D) and the overall gain (G) parameters. A good quality lock is obtained by iteratively increasing these gains up to the point where

we see no oscillations appearing in the error-signal and thus, in the corresponding modulated-probe signal. The idea behind this is the fact that an error-signal is essentially a DC signal. Oscillations at higher frequencies due to strong correction signals will appear as noise on the slowly varying envelope of this signal, thereby leading to fluctuations in the laser frequency. For our laser locking setups, the lock quality ('good' or 'bad') is mainly affected by the parameter settings of the fast current-PID controller. The slow-PID has a bandwidth of the order 1 KHz [35] and thus the control action is limited in terms of speed: we simply set this PID to moderate parameter gains, that are given in tables 3.2 and 3.3. The current controller, on the other hand has bandwidth of the order 25 KHz (typical of most fast PID's) and responds quickly to any change in its polarity or gain settings. To optimize the lock parameters of the current-PID, we monitored the error-signal both in time and frequency domain using the digital oscilloscope functionality provided in **Toptica DLC PRO software**. Here it is important to mention that using the frequency response of the error-signal is a more reliable way to optimize PID gains than using the frequency response of the modulated-probe signal itself. The reason lies in the fact that the modulated-probe contains frequency components at the the modulation frequency as well as the harmonics, which are generally higher than the controller bandwidth. Since, we are mainly interested in monitoring oscillations that occur within the bandwidth of the current-PID, sampling the modulated-probe signal at frequencies below the Nyquist frequency leads to aliasing effects: hence, we see signals that are actually at other frequencies. To avoid this confusion, it is appropriate to monitor the frequency components of the error-signal, which being a DC signal, is immune to aliasing.

The PID gains should be high enough to compensate for any change in laser frequency due to external disturbances but not so high so as to introduce oscillations in the error-signal. For our D2-repump laser, the optimized parameters for locking to the feature of Fig. 3.8(b) are listed in table 3.2 with the frequency response of the corresponding error-signal shown in Fig. 3.10(a). At this setting, only the DC component is present with no oscillations at high frequencies. To get these optimized values, we started with all parameters being set to unity. Next, the P and G values were gradually increased, in no particular order, till higher frequency components appeared. At this point, we can reduce either P or G till oscillations stop or are significantly diminished. To be able to increase the P and G values further without letting oscillations to appear, we now increase the I and D gains. The integral

and derivative components improve the system's response at low and high frequencies respectively. After increasing I and D, we can again increase P and G values till we see oscillations. Alternatively, we can set the system into oscillation by using a high P or G value, and then increase I or D gains so that the oscillations can stop. By iterating between the two approaches, we zeroed in on the parameter values listed in the table.

For the D1-laser, the PID gains for locking to the feature of Fig. 3.8(d) are listed in table 3.3 with the frequency response of the corresponding error-signal shown in fig. 3.11(a). The frequency responses shown in the figure are different from their D2 counterparts in two aspects: (1) A low frequency component of around 2.8 kHz is present, the peak of which increases at high P and G values. (2) Higher frequencies do get excited at high gain settings, however, their amplitudes are significantly smaller than the 2.8 kHz signal. For the D1-laser SAS setup, the modulated-probe signal from the photodiode is not directly fed into the lock-in amplifier unit of the DLC Pro laser controller. Rather it first passes through an external signal-conditioning circuit that includes an amplifier and a low-pass filter stage. The output of this conditioning circuit then goes to the lock-in amplifier input. The 2.8 kHz happens to be the cut-off frequency of the external low-pass filter.

### 3.5 Beat Frequency Stabilization of the Tapered-Amplifier Laser

As shown in Fig. 3.2, we use a tapered-amplifier laser (TA PRO) to generate the cooling beam on the D2-line. In addition, beams for absorption-imaging (to determine the number of trapped atoms in the cloud as well as the temperature); optical-pumping (to pump the atoms into magnetically trapable  $|^2S_{1/2}, F = 2, m_F = 2\rangle$  state); and pushing the collimated-beam from the 2D-MOT to 3D-MOT chamber are all generated from this TA PRO laser. These transitions are shown in Fig. 3.1.

The laser consists of two main components: a seed laser, which is an extended cavity type diode laser, and a tapered amplifier unit. The seed laser beam goes to the input of the amplifier and the amplified beam is then the final laser output. The optics for directing the seed beam to the amplifier input is all internal. Since the seed laser is the standard diode laser, we adjust its wavelength via the diode injection current as well as the DC voltage that is applied to the piezo-transducer. We stabilize the frequency of

<b>Laser Parameters</b>	
Piezo Voltage <sup>a</sup>	39.127312 V
Set Current	312.32619 mA
Set Temperature <sup>b</sup>	20.000000 °C
Measured Wavelength	766.701 nm
<b>Optical Setup</b>	
Vapour-cell temperature	62 °C
Probe power	0.028 mW
Pump power	0.200 mW
AOM-carrier frequency	80 MHz
Single-pass AOM-diffraction efficiency	0.7
<b>Scan Parameters</b>	
Scan Frequency	0.4 Hz
Scan Offset	39.127312 V
Scan Amplitude	1.880022 V
<b>Lock-in detection parameters</b>	
Modulation Frequency ( $\omega_D$ )	25000 Hz
Modulation Amplitude ( $A_M$ )	0.3 V p-p
Phase Difference ( $\Phi$ )	150 °
Peak-Noise Tolerance	0.01398 V
<b>Current-PID Settings</b>	
Gain	3.0
P	4.5 mA / V
I	10.0 mA / V / ms
D	10.5 mA / V $\times \mu s$
Polarity	Negative
<b>Piezo-PID Settings</b>	
Gain	0.7
P	1.4 V / V
I	2.0 V / V / ms
D	1.0 V / V $\times \mu s$
Polarity	Positive

TABLE 3.2: Details of D2-line spectroscopy setup

<sup>a</sup>Laser wavelength can shift occasionally due to variations in the surrounding temperature, humidity, stray magnetic fields...etc. and thus, when this happens, the current and piezo settings need to be changed to get the desired wavelength back. Thus, the piezo-voltage and current values listed in the table are not permanent and can change when required.

<sup>b</sup>Fine adjustment of laser-wavelength can also be done by increasing or decreasing the temperature of laser diode chip by  $\pm 0.1 - 0.4^\circ$  [35], however, to date, it has not been needed for any of our three lasers.

<b>Laser Parameters</b>	
Piezo Voltage	63.464779 V
Set Current	309.20485 mA
Set Temperature	20.00000 ° C
Measured Wavelength	770.108 nm
<b>Optical Setup</b>	
Vapour-cell temperature	62 ° C
Probe power	0.035 mW
Pump power	0.260 mW
AOM-carrier frequency	80 MHz
Single-pass AOM-diffraction efficiency	0.7
<b>Scan Parameters</b>	
Scan Frequency	0.15 Hz
Scan Offset	63.464779 V
Scan Amplitude	1.453803 V
<b>Lock-in detection parameters</b>	
Modulation Frequency ( $\omega_D$ )	18000 Hz
Modulation Amplitude ( $A_M$ )	0.2 V p-p
Phase Difference ( $\Phi$ )	150 °
Peak-Noise Tolerance	0.15 V
<b>Current-PID Settings</b>	
Gain	0.5
P	2.0 mA / V
I	10.0 mA / V / ms
D	10.0 mA / V $\times \mu s$
Polarity	Negative
<b>Piezo-PID Settings</b>	
Gain	0.4
P	0.7 V / V
I	3.0 V / V / ms
D	0.4 V / V $\times \mu s$
Polarity	Positive

TABLE 3.3: Details of D1-line spectroscopy setup

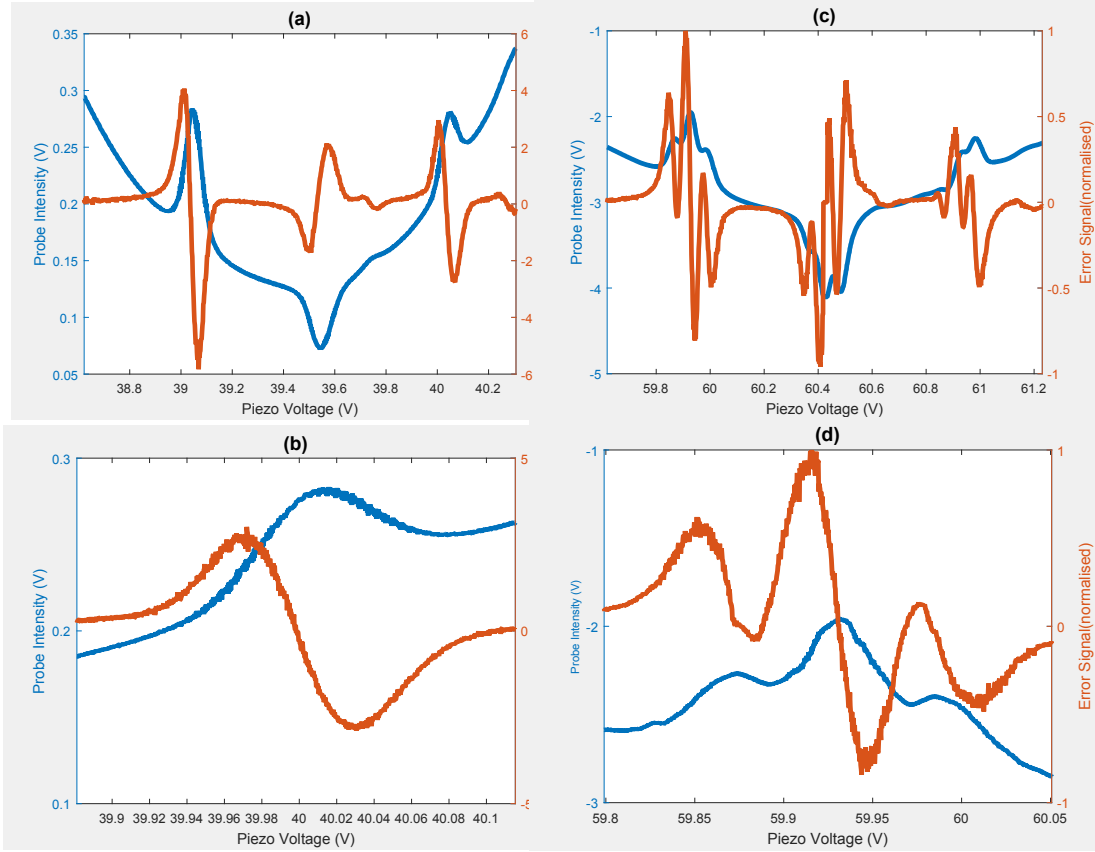


FIGURE 3.8: **(a)**: Measured saturated spectrum on the D2 line (blue) and derivative / error-signals (red) corresponding to each of the three features. The saturated features from left to right correspond to  $|^2S_{1/2}, F = 2\rangle \rightarrow |^2P_{3/2}\rangle$  (**cooling**),  $|^2S_{1/2}, F = 12\rangle \rightarrow |^2P_{3/2}\rangle$  (**ground-crossover**) and  $|^2S_{1/2}, F = 1\rangle \rightarrow |^2P_{3/2}\rangle$  (**repump**) respectively. **(b)**: The scan offset and scan amplitude applied to the laser piezo are adjusted so as to ‘zoom in’ on the repump feature (rightmost in (a)). At this point, the scan is disabled and the PID-controller loops are enabled so that the derivative of the feature gets ‘pinned’ to zero, thereby locking the laser frequency to the repump transition. **(c)**: Measured saturated spectrum features on the D1 line (blue) with the corresponding derivative signals (red). The two resolved transitions on the left are  $|^2S_{1/2}, F = 2\rangle \rightarrow |^2P_{1/2}, F' = \{1, 12\}\rangle$ ; the center feature shows ground-crossover peaks at  $|^2S_{1/2}, F = 12\rangle \rightarrow |^2P_{1/2}, F' = \{1, 12, 2\}\rangle$ ; the feature on the right corresponds to  $|^2S_{1/2}, F = 1\rangle \rightarrow |^2P_{1/2}\rangle$  transition with individual peaks that are not so well-resolved and hence are difficult to be identified explicitly. **(d)**: The scan signal adjusted so as to zoom in on the excited crossover transition at  $|^2S_{1/2}, F = 2\rangle \rightarrow |^2P_{1/2}, F' = 1'2'\rangle$ . Our D1 laser is locked to this transition.

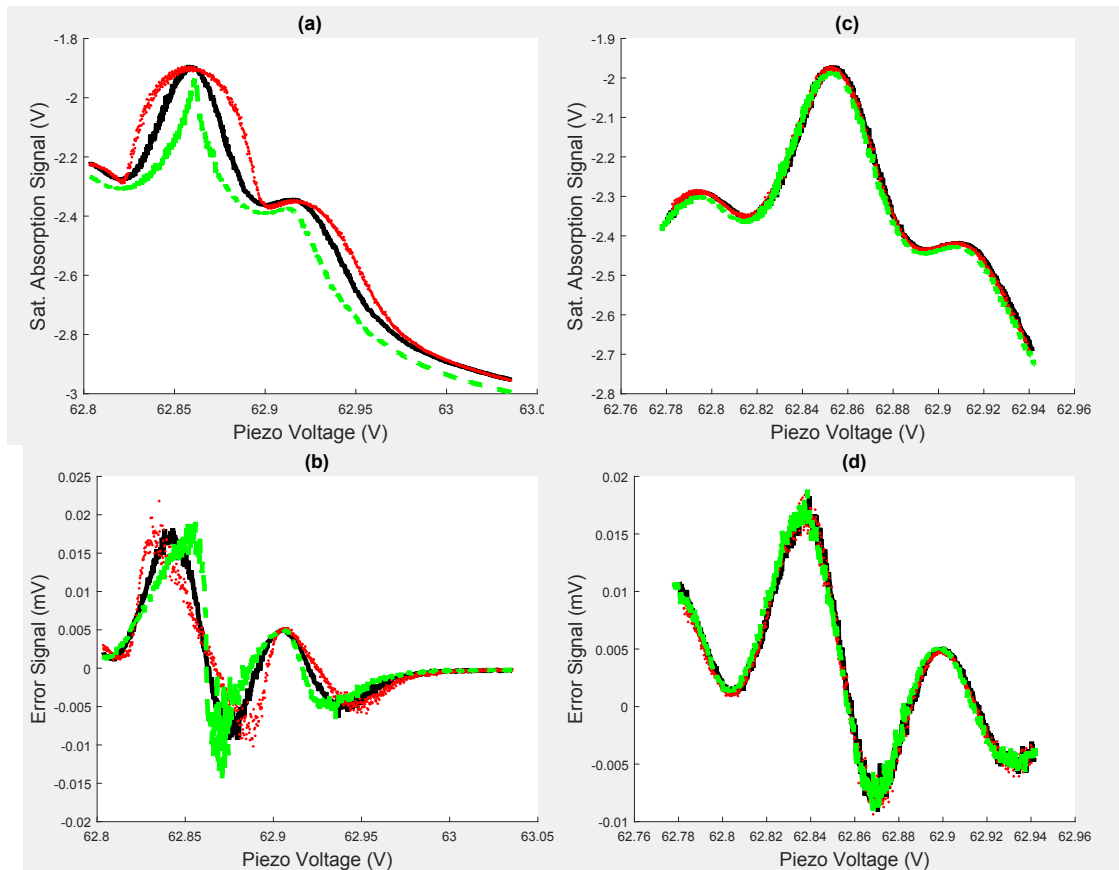


FIGURE 3.9: Determining the correct polarity of our PID controllers: **(a,b)**: Distortion of saturated-absorption feature as well as the error-signal as a function of the current-PID polarity. The signals obtained via regular scan (solid black) serve as reference signals. With respect to them, the saturated feature gets broader and the slope of the error-signal gets flatter (both shown in dotted red) when the polarity is negative. Conversely, for positive polarity, the saturated feature gets narrower and the error-signal steeper (shown in dashed green) indicating the correct polarity is negative. **(c-d)**: Effect of polarity of the piezo PID on the shape of the saturated feature and the corresponding error signal. The correct polarity is positive with the corresponding signals shown in dashed green. Coloring scheme similar to (a) and (b) is chosen.

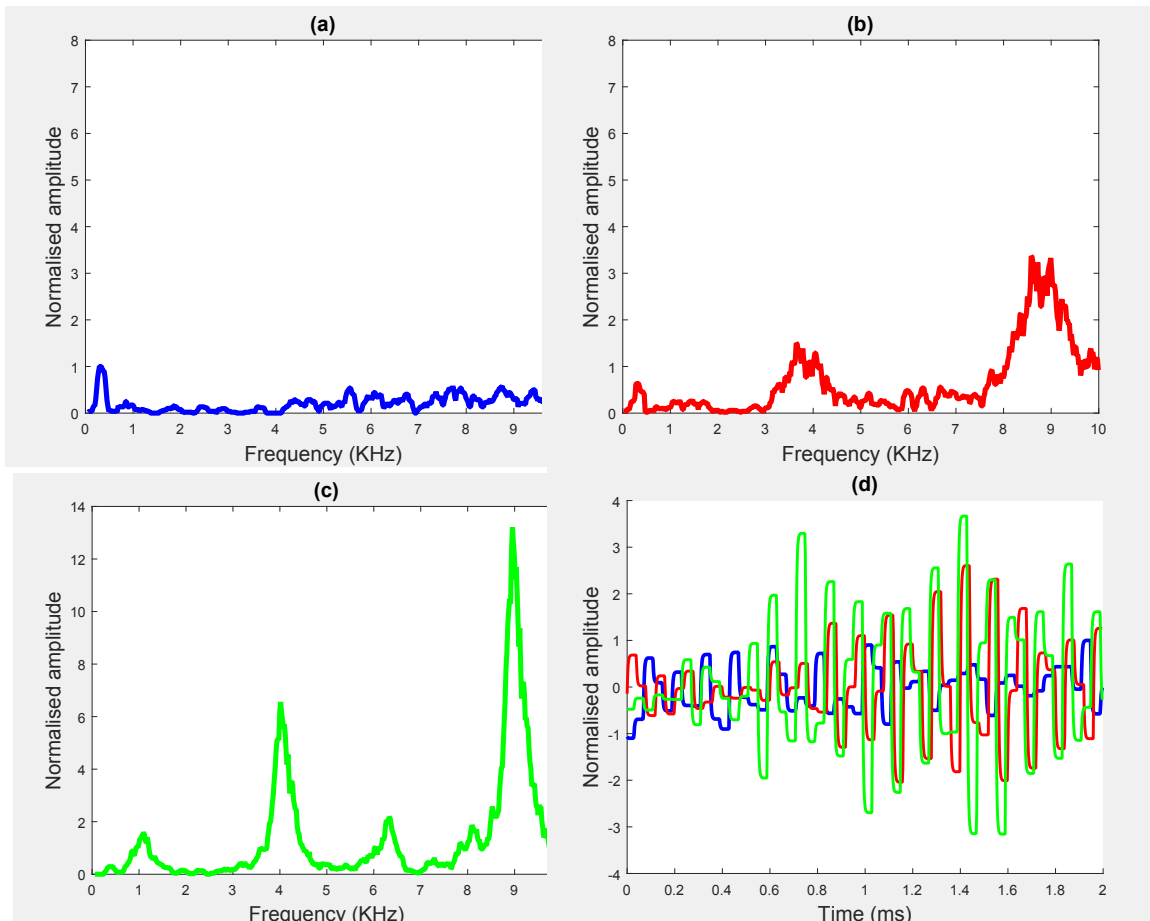


FIGURE 3.10: **(a)-(c)**: Fourier transform of the derivative signal of Fig. 3.8 (b) as a function of the PID settings of the current controller. **(a)**: Only DC component is present for the optimized parameter values listed in table 3.2. We can observe a similar response at lower PID values, however, that could correspond to a ‘weak’ lock. **(b)**: Upon increasing the P value to  $\approx 7.5$  mA / V and keeping all others the same as in (a), oscillations can be seen around 4 and 9 KHz. **(c)**: Keeping I and D same as in (a) and setting  $G = 6.5$ ,  $P = 5.5$  mA / V, the oscillations get stronger and could not be stopped by further increasing I or D values. **(d)**: Time response of the error-signal for PID settings of ((a): blue), ((b): red) and ((c): green) respectively. Note the correspondence of the green curve with the corresponding frequency curve in (c). Due to the presence of multiple frequencies, the time-based error signal is in the form of a wavepacket.

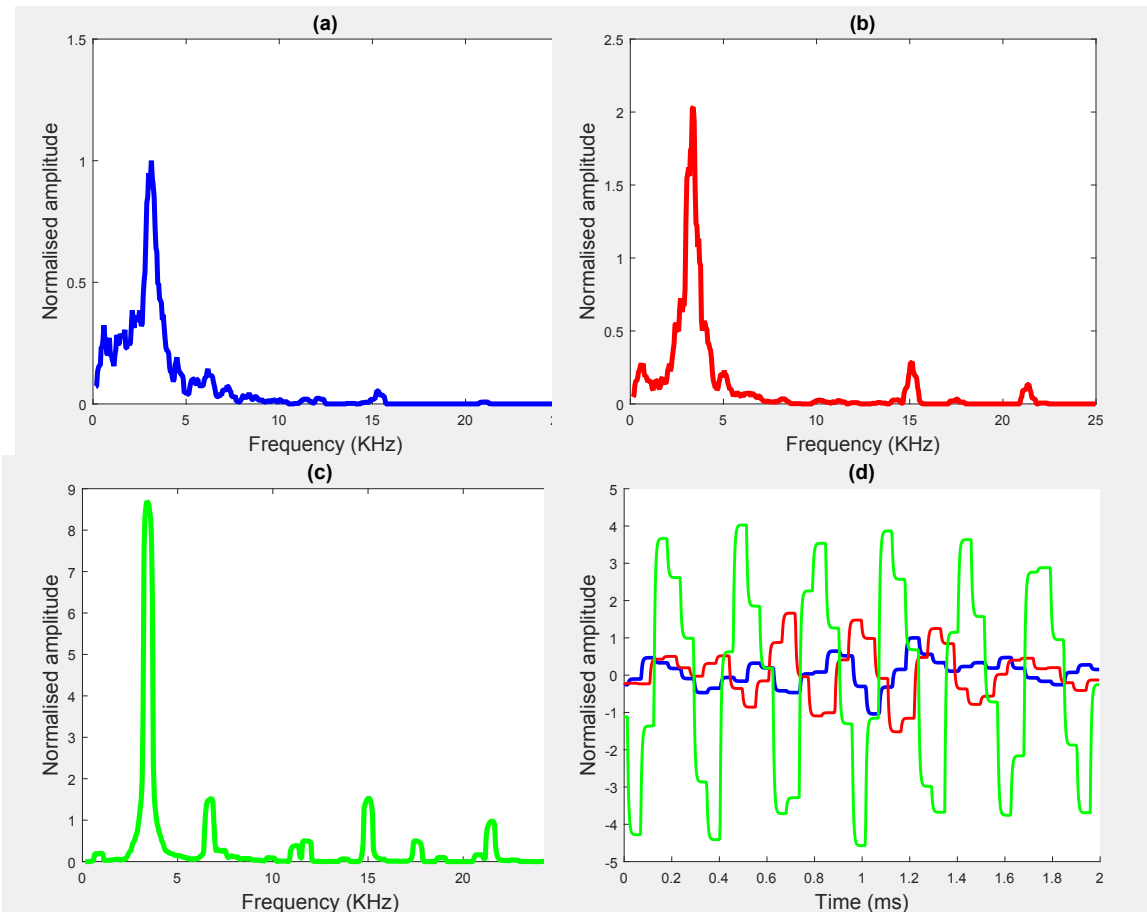


FIGURE 3.11: **(a)-(c)**: Fourier transform of the derivative signal of Fig. 3.8 (d) as a function of PID gain settings of the current controller. **(a)**: A low frequency component of around 2.8 kHz is visible for the parameters listed in table 3.3. This corresponds to the cut-off frequency of the external low-pass filter circuit that is used for signal conditioning the modulated-probe intensity. **(b)**: Keeping all other parameters same, the P gain was increased to 4 mA / V resulting in the onset of oscillations at 15 and 22 KHz. Also, the low frequency component increased. **(c)**: At  $P = 4$  mA / V,  $G = 1.5$ , the low frequency component gets stronger while small components at other frequencies are also induced. **(d)**: Time response of the error-signal for PID settings of ((a): blue), ((b): red) and ((c): green) respectively.

our TA Pro laser in the following way: the D2-repump laser is locked to the  $|^2S_{1/2}, F = 1\rangle \rightarrow |^2P_{3/2}\rangle$  line using saturated-spectroscopy. Treating the repump laser as the reference / master laser and the TA Pro as the slave laser, we mix the beams from the two lasers so as to get a ‘beat-signal’, which is the difference in frequency between the two lasers. By keeping the beat-frequency constant (using dedicated electronics), we can stabilize the frequency difference between the master and the slave lasers and since the master-laser is already frequency-locked, the slave-laser also gets locked at a constant frequency offset with respect to the master !! We now calculate the desired beat-frequency:

The atomic repump and cooling transition frequencies on the D2-line are given (using table 3.1), respectively, as:

$$\omega_{\text{R}}^{\text{D2}} = \omega_0^{\text{D2}} + 281.9 \text{ MHz} \quad (3.9)$$

$$\omega_{\text{C}}^{\text{D2}} = \omega_0^{\text{D2}} - 158.8 \text{ MHz} \quad (3.10)$$

We calculated the locked frequency of the repump laser in Eqn. 3.6 as:

$$\omega_{\text{R,laser}}^{\text{D2}} = \omega_0^{\text{D2}} + 201.9 \text{ MHz} - \delta_{\text{R}}^{\text{D2}} \quad (3.11)$$

where the factor  $\delta_{\text{R}}^{\text{D2}}$  accounts for the fact that the repump-laser is locked to the entire D2-manifold as opposed to any individual level.

The generation of cooling beams requires some considerations: cooling beams are generated for MOT and molasses stage with the resulting atomic temperatures being the function of both laser power and detuning (Eqn. 2.7). To have a flexible control over both laser power and frequency, we will use AOMs in a double-pass configuration, and take the positive order of the second pass as the cooling beam. Thus, the cooling beam will be up-shifted in frequency by an amount equal to twice the AOM carrier frequency. We typically set the AOM frequency at 80 MHz and thus, the cooling frequency would be up-shifted by 160 MHz with respect to the cooling-laser frequency. To compensate for this shift, we must lock the cooling-laser 160 MHz below resonance. Moreover, D2-cooling requires the beam to be red-shifted by some factor  $\delta_{\text{C}}^{\text{D2}}$ , the optimal value of which needs to be characterized experimentally. We can thus, write the cooling-laser frequency as:

$$\begin{aligned} \omega_{\text{C,laser}}^{\text{D2}} &= \omega_0^{\text{D2}} - 158.8 \text{ MHz} - 160 \text{ MHz} - \delta_{\text{C}}^{\text{D2}} \\ &= \omega_0^{\text{D2}} - 318.8 \text{ MHz} - \delta_{\text{C}}^{\text{D2}} \end{aligned} \quad (3.12)$$

Thus, the beat frequency  $\omega_{\text{beat}}$  which is equal to  $\omega_{\text{R,laser}}^{\text{D2}} - \omega_{\text{C,laser}}^{\text{D2}}$  can be calculated as:

$$\begin{aligned}\omega_{\text{beat}} &= \left( \left( \omega_0^{\text{D2}} + 201.9 \text{ MHz} - \delta_{\text{R}}^{\text{D2}} \right) - \left( \omega_0^{\text{D2}} - 318.8 \text{ MHz} - \delta_{\text{C}}^{\text{D2}} \right) \right) \\ &= 520.7 \text{ MHz} + (\delta_{\text{C}}^{\text{D2}} - \delta_{\text{R}}^{\text{D2}})\end{aligned}\quad (3.13)$$

It must be emphasized here that in Eqn. 3.13, the factor  $\delta_{\text{R}}^{\text{D2}}$  is due to the repump laser not precisely locked to the  $|F = 1\rangle \rightarrow |F = 2\rangle$  D2-line transition. The factor  $\delta_{\text{C}}^{\text{D2}}$  on the other hand, can be tuned externally by simply changing the beat frequency. The beat frequency can be varied by changing the reference frequency, which is a part of the electronics stabilization circuit and is discussed next.

The cooling laser has two outputs: the main amplified output beam with  $\approx 1.7$  W power and a small fraction of the seed laser beam with  $\approx 2.5$  mW power. We split the output from the seed laser into two: one part is used for wavelength-monitoring while the other part is mixed with the beam from the repump laser, in order to generate the beat-signal (see Fig. 3.12). The beat-signal is detected using a fast, 1 GHz bandwidth, Si-amplified photo-detector (**New Focus: 1601FC-AC, Courtesy: Dr. Davis lab**). The detector-output goes through a 5 V amplifier (**Minicircuits: ZX60103PL-N+**) and then to a phase-locked loop (PLL) evaluation-board. The PLL board (**Analog Devices: EVAL4007EBZ1**) consists of some internal frequency dividers and a phase-frequency detector IC (**Analog Devices: EVAL4007**). The board receives two inputs; the detected beat-frequency signal, which is applied at the  $\text{RF}_{\text{IN}}$  input and a reference signal (comes from **Novatech 409B**) which is applied at the  $\text{REF}_{\text{IN}}$  input (see Fig. 3.12). The two frequencies:  $\omega_{\text{beat}}$  of the beating signal and  $\omega_{\text{ref}}$  of the reference signal, are internally divided by 8 and 2 respectively. Both the frequency-divided signals are the inputs to the internal phase-frequency detector circuit which generates at the output ( $\text{CP}_{\text{OUT}}$ ), a signal proportional to the difference in phase and frequency of the two inputs. This output is zero when the input signals have the same frequency and phase. For the two signal inputs to the internal PLL chip to have the same frequency:

$$\begin{aligned}\frac{1}{8} \times \omega_{\text{beat}} &= \frac{1}{2} \times \omega_{\text{ref}} \\ \Rightarrow \omega_{\text{beat}} &= 4 \times \omega_{\text{ref}}\end{aligned}\quad (3.14)$$



The desired beat-frequency was calculated in Eqn. 3.13 and thus, the reference frequency should be  $130.175 \text{ MHz} + \Delta$ , where  $\Delta = \frac{1}{4} \times (\delta_C^{D2} - \delta_R^{D2})$ . By changing this reference frequency, we change the beat-frequency between the two lasers and thus, the frequency of the TA Pro laser itself. As the MOT cooling beams are derived from this laser (§. 3.6.1), the detuning of the cooling beams with respect to the  $|F = 2\rangle \rightarrow |F' = 3\rangle$  transition can be changed simply by varying the reference frequency. The **Novatech generator** has a 0.1 Hz resolution and hence, precise detunings can be achieved. *This highlights the power and flexibility of beatnote locking method: we can change the detuning of the cooling beams on the scale of few tens of MHz without having to change any of the associated double-pass AOM carrier frequencies (Fig. 3.2). This is quite essential in the initial stages of implementing the 3D-MOT and molasses: by varying the detuning of the cooling beams, we can characterize the number density of the trapped atomic cloud.*

The output from the PLL board is passed through a simple RC filter (**R** = 1 k $\Omega$ , **C** = 0.1  $\mu\text{F}$ ) and then goes as an input to a PID-controller (**New Focus: LB1005**). It is logical to think of the PLL-output as an error-signal since it is a function of the frequency (and phase) difference between the two inputs and hence by maintaining it around 0, we make our beat-frequency to satisfy the Eqn. 3.14. In this way, we frequency and phase lock our D2-cooling and repump lasers. Lastly, to close the feedback-loop, the output of the PID-controller is directed to the piezo-channel of the cooling laser. This is done by keeping the internal scan disabled and enabling the ‘analog remote control’ option in the *DLC-PRO* interface. This allows to scan the cooling laser externally via the servo controller output. We also use an analog function generator (**Dynascan Corporation 3020**) to add a sweep signal (of about 10 Hz) to the PID-output. When the PID loop is disabled, the output of the controller is only the sweep signal which then scans the cooling laser and we can monitor the error-signal as a function of the cooling-laser frequency. Our PID-controller also has the capability to shift the sweep center or to increase/decrease the sweep amplitude. This allows to locate the lock-point of interest. Upon enabling the PID-loop, the correction signal adds to the sweep signal in such a way so as to keep the relevant error-signal to zero. The locked beat-frequency is monitored by applying the MUX\_OUT signal of the PLL board, as an input to a frequency counter. Since the MUX output is weak, it needs to be pre-amplified (**Minicircuits: ZFL-500-BNC**) before it can be detected using the frequency counter (**STARTEK: ATH70**).

## 3.6 Optical Setup Revisited

This part is a logical continuation of Sections. 3.1 and 3.2 : here we calculate the frequencies for exciting the transitions shown in Fig. 3.1, and describe the stages in our optical setup that generates the laser beams with these frequencies. The complete optical setup is shown in Fig. 3.2.

### 3.6.1 Generation of D2-beams

The atomic repump transition frequency on the D2-line (Eqn. 3.9) is:

$$\omega_{\text{R}}^{\text{D2}} = \omega_0^{\text{D2}} + 281.9 \text{ MHz}$$

and the corresponding parent diode laser is locked to the frequency (Eqn. 3.6):

$$\omega_{\text{R,laser}}^{\text{D2}} = \omega_0^{\text{D2}} + 201.9 \text{ MHz} - \delta_{2\text{R}}$$

The repump transition is chosen from  $|F = 1\rangle \rightarrow |F' = 2\rangle$ . Our repump-laser is red-detuned to this transition by  $\sim 80$  MHz. To generate the repump beams for the 2D and 3D-MOT, we compensate this detuning by up-shifting the  $\omega_{\text{R,laser}}^{\text{D2}}$  frequency using an acousto-optic-modulator that is set at the carrier frequency of 80 MHz. These repump beams are derived from a single diode laser which is limited to 75 mW of power. To ensure sufficient power in these beams inside the 2D and 3D-MOT chambers, we amplify the parent laser beam using Toptica's external BoostA tapered amplifier. The same kind of amplifier unit is present inside the TA PRO cooling laser. We use BOOSTA to simultaneously amplify both the D2 as well as the D1 diode laser beams, before we opto-electronically manipulate their frequencies to generate the necessary transitions. As the amplifier can receive a maximum optical input of 40 mW, we send about 15 mW of D2 and 25 mW of D1 diode laser power.

As shown in Fig. 3.2, these beams are spatially combined using an interference-filter (with 90 % efficiency) before they are amplified. A typical tapered amplifier (TA) amplifies a single polarization state and if the incoming beam polarization is misaligned, it leads to reduced power and a poor spatial beam profile at the output. Hence, at the input stage of the BOOSTA, a half waveplate is placed to align the polarization of the incoming beams with that of the TA. The amplified beam at the BOOSTA output consists of both the D1 and D2 wavelengths, which must be spatially separated. This is done using another interference filter. Having spatially separated, this D2-beam is passed

through an acousto-optic modulator (AOM) operating at 80 MHz carrier frequency, that is aligned to get a higher efficiency in the positive first order. This in turn brings it closer to resonance with the repump transition. The up-shifted beam is then split into two parts using a polarizing beam-splitter: they are then fiber-coupled to 2D and 3D-MOT chambers. The AOM diffraction and the fiber coupling efficiency in this case are around 65-67 %.

We next describe the optical paths associated with the D2-cooling laser: these include generating cooling beams for the 2D and 3D-MOT, beams for optical-pumping, absorption-imaging and also the push-beam. The amplified output beam of the cooling laser has an elliptical profile and diverges along the vertical axis in the far-field while remains collimated along the horizontal direction. To keep the beam collimated, we use a telescopic arrangement of one plano-convex and another plano concave lens of focal lengths 100 and -50 mm respectively. The telescope acts as a beam reducer and keeps the vertical waist of the beam collimated while not significantly affecting the horizontal waist. The far-field measurement gave the beam waist as  $1.3 \mu\text{m}$  and  $1.9 \mu\text{m}$ , along the  $x$  and  $y$  axis respectively. Moreover, unlike the repump beams, we generate the cooling beams for 2D and 3D-MOT independently. This gives the flexibility to individually control the power as well as detuning of the cooling beam in the two MOT stages. To do this, the main output power is split into two paths: along one path, we generate the 2D-MOT, optical-pumping and the push beams; while along the second path, are generated the 3D-MOT and imaging beam.

First the 2D-MOT path is discussed: the cooling transition is chosen from  $|F = 2\rangle \rightarrow |F' = 3\rangle$  with the resonant frequency (Eqn. 3.10) of:

$$\omega_C^{\text{D2}} = \omega_0^{\text{D2}} - 158.8 \text{ MHz}$$

and our cooling laser is locked to the frequency (Eqn. 3.12):

$$\omega_{C,\text{laser}}^{\text{D2}} = \omega_0^{\text{D2}} - 318.8 \text{ MHz} - \delta_C^{\text{D2}}$$

It can be seen that the parent laser beam is  $160 + \delta_C^{\text{D2}}$  MHz red-detuned with respect to the said transition. To generate the cooling beam, a part of the parent beam is passed through a double-pass AOM configuration with the positive order of the second pass to be used as the 2D-MOT beam. Currently, the AOM is set at 80 MHz. This means the cooling beam is up-shifted by  $2 \times 80 = 160$  MHz at the end of the second pass. This leaves the cooling beam red-detuned by  $\delta_C^{\text{D2}}$  with respect to the cooling transition. Recall that this

detuning factor can be chosen via selecting the beat-frequency in Eqn. 3.13. Typically, it is chosen to lie between  $3\Gamma$  to  $6\Gamma$  [22], where  $\Gamma = 5.956$  MHz is the natural linewidth of  $^{39}\text{K}$ . Further, the zeroth order of the second pass is up-shifted by only 80 MHz with respect to the parent beam. We use this zeroth order for generating the optical-pumping beam. The zeroth order is passed through another AOM (single-pass) such that the positive order of this stage is taken for optical pumping. The carrier frequency of this single-pass AOM is chosen by considering the resonant frequency for  $|F = 2\rangle \rightarrow |F' = 2\rangle$  transition (from table. 3.1):

$$\omega_{\text{opt}}^{\text{D2}} = \omega_0^{\text{D2}} - 179.8 \text{ MHz}$$

Thus, the concerned zeroth order is  $59 + \delta_{\text{C}}^{\text{D2}}$  below resonance. If we chose,  $\delta_{\text{C}}^{\text{D2}} = 3\Gamma = 17.868$  MHz, we can set the AOM at 76.868 MHz carrier-frequency.

Next, the push beam is generated by passing some portion of the parent beam through another double-pass AOM configuration, and taking the positive order of the second pass. To choose the carrier frequency of this AOM, we note that the push-beam must be blue-detuned with respect to the cooling transition. Denoting the AOM-carrier frequency by  $\omega_{\text{AOM}}^{\text{opt}}$ , the condition for positive detuning requires:

$$\begin{aligned} 2 \times \omega_{\text{AOM}}^{\text{push}} &> 160 \text{ MHz} + \delta_{\text{C}}^{\text{D2}} \\ \Rightarrow \omega_{\text{AOM}}^{\text{push}} &> 80 \text{ MHz} + \frac{1}{2}\delta_{\text{C}}^{\text{D2}} \end{aligned}$$

Similar to the 2D-MOT beam, the cooling beam for the 3D-MOT chamber is taken as the positive order of the second pass, generated through another double-pass AOM configuration. By changing the factor  $\delta_{\text{C}}^{\text{D2}}$ , we simultaneously change the detuning of the two MOT beams with respect to the cooling transition. To change their detunings individually, we simply change the carrier frequencies of the respective AOMs, and this is where the advantage of using AOMs in a double-pass arrangement comes in: as seen in fig. 3.2, each double-pass configuration uses a plano-convex lens (focal length either 75 mm or 100 mm), placed in between the AOM and the retro-reflecting mirror. The spacing between the AOM and the lens as well as the lens and the mirror equals the focal length of the lens. Such an arrangement forms a 'cat-eye' reflector [36] and drastically improves the frequency-tuning range (bandwidth) of the double-pass configuration. This allows to span the AOM

carrier frequency over a broad range without significantly loosing the optical alignment. The range of detuning that can be achieved in this way is then twice the AOM-span range.

The absorption-imaging beam is generated by taking the zeroth order of the second pass from the 3D-MOT AOM and passing it through another AOM (single-pass). The resultant positive order can then be used for imaging the  $|F = 2\rangle \rightarrow |F' = 3\rangle$  transition.

### 3.6.2 Generation of D1-beams

To implement ‘Gray-Molasses’ cooling, we generate laser beams that are blue-detuned with respect to the  $F' = 2$  excited level on the D1 line. Unlike the D2 case, both the cooling and repump beams for the D1-transitions are derived from a single diode laser. This preserves the phase-coherence between the cooling and repump beams, which is essential to achieve the Raman-resonance condition during Gray-Molasses. The source laser is locked at 80 MHz below  $|^2S_{1/2}, F = 2\rangle \rightarrow |^2P_{1/2}, F' = 12\rangle$  transition using saturated spectroscopy. The locked laser frequency (Eqn. 3.8) is:

$$\omega_{\text{laser}}^{\text{D1}} = \omega_0^{\text{D1}} - 260.1 \text{ MHz}$$

The cooling and repump transitions are chosen to be from  $|F = 2\rangle \rightarrow |F' = 2\rangle$  and  $|F = 1\rangle \rightarrow |F' = 2\rangle$  respectively having transition frequencies of:

$$\omega_{\text{C}}^{\text{D1}} = \omega_0^{\text{D1}} - 152.3 \text{ MHz} \quad (\text{Cooling}) \quad (3.15)$$

$$\omega_{\text{R}}^{\text{D1}} = \omega_0^{\text{D1}} + 309.4 \text{ MHz} \quad (\text{Repump}) \quad (3.16)$$

This implies our source laser is 107.8 MHz and 569.5 MHz below the cooling and repump resonance respectively.

As discussed earlier, in order to have sufficient cooling and repump power, the D1 laser beam is amplified in conjunction with the D2 repump laser via BOOSTA, and then spatially separated by means of an interference filter. By using a telescopic arrangement consisting of a plano-convex ( $f = 100 \text{ mm}$ ) and a plano-concave ( $f = -50 \text{ mm}$ ) lens, we measured in the far-field, the beam width to be  $1.6 \mu\text{m}$  and  $2.1 \mu\text{m}$  respectively along the  $x$  and  $y$  axis. Next, the amplified D1 beam goes through an electro-optic modulator (EOM). The output beam from the EOM contains three frequency components: the (unshifted) center frequency at  $\omega_{\text{laser}}^{\text{D1}}$ , an upper sideband at  $\omega_{\text{laser}}^{\text{D1}} + \omega_{\text{EOM}}$  and

a lower sideband at  $\omega_{\text{laser}}^{\text{D1}} - \omega_{\text{EOM}}$ , where  $\omega_{\text{EOM}}$  is the resonant driving frequency of the EOM crystal, which is mechanically tunable. Using the Fabry-Perot interferometer, the sidebands were measured to have approximately  $(1/6)^{\text{th}}$  the power contained in the center frequency. It must be emphasized that these frequencies are not spatially separated. We further shift these frequencies using AOMs such that the center frequency can be used for cooling transition and the upper sideband for repump. As both the cooling and repump frequencies are present in one beam, the associated optics are simpler compared to the D2 setup.

As shown in Fig. 3.2, the D1 beam after passing through the EOM stage goes through an AOM (AOM1) in a double-pass configuration: the positive order of the second pass is taken to be used for cooling in the 3D-MOT chamber<sup>3</sup> while the zeroth order of the second pass goes through another AOM (AOM2) in a single-pass such that the positive diffracted order is taken to be used in the 2D-MOT chamber. We can write expressions for each of the cooling and repump frequencies for both the 2D and 3D-MOT cases:

$$\begin{aligned}\omega_{\text{C},3\text{D-MOT}}^{\text{D1}} &= \omega_{\text{laser}}^{\text{D1}} + 2\omega_{\text{AOM1}} \\ \omega_{\text{C},2\text{D-MOT}}^{\text{D1}} &= \omega_{\text{laser}}^{\text{D1}} + \omega_{\text{AOM1}} + \omega_{\text{AOM2}} \\ \omega_{\text{R},3\text{D-MOT}}^{\text{D1}} &= \omega_{\text{laser}}^{\text{D1}} + \omega_{\text{EOM}} + 2\omega_{\text{AOM1}} \\ \omega_{\text{R},2\text{D-MOT}}^{\text{D1}} &= \omega_{\text{laser}}^{\text{D1}} + \omega_{\text{EOM}} + \omega_{\text{AOM1}} + \omega_{\text{AOM2}}\end{aligned}$$

Here  $\omega_{\text{EOM}}$  is the driving radio-frequency of the EOM,  $\omega_{\text{AOM1}}$  and  $\omega_{\text{AOM2}}$  refer to the AOM carrier frequencies for the double and single-pass stage respectively. As discussed in Chapter 2, the lowest temperature is obtained when both the cooling and repump are blue-detuned equally with respect to the  $F' = 2$  level. We ensure this condition by choosing  $\omega_{\text{EOM}} = 461.7$  MHz, which is the ground hyperfine splitting in  $^{39}\text{K}$ . This leaves both the unshifted frequency (cooling) and the upper-sideband frequency (repump) to be 107.8 MHz from  $F' = 2$ . By operating the AOMs around 60 MHz, the beams get blue-detuned. The ‘cat-eye’ arrangement in the double-pass AOM case allows to span the carrier frequency range, making it possible to have wide detuning range for the D1 beams during the 3D-MOT stage and pure D1-molasses phase.

<sup>3</sup>It must be remembered that the MOT stages are implemented using D2-beams on the  $|F = 2\rangle \rightarrow |F' = 3\rangle$  transition. Following [15], we plan to shine D1-beams during the 2D and 3D MOT stages as this is intended to lead additional cooling cycles during the MOT stage itself. This would be followed by a pure D1-molasses with the D2 beams off.

The frequencies discussed in this section are summarized in table. 3.4. We must emphasize again that while talking about generation of D1-cooling and repump frequencies for the 2D and 3D-MOT, we do not mean that we are implementing a MOT stage on the D1-line. Both 2D and 3D-MOT stages in our experiment are implemented on the D2-line, and the presence of D1 cooling beams during these stages shall lead to additional cooling cycles, as reported in [15].

### 3.7 Magneto-Optical Traps

The sub-Doppler cooling schemes discussed in Chapter 2, rely on velocity-dependent damping forces to slow down atomic beams, by using 3 orthogonal pairs of counter-propagating laser beams. However, the 3D optical-molasses region created at the intersection of these laser beams has a narrow capture velocity range. Therefore, loading thermal atoms ‘directly’ into the molasses region gives inefficient cooling: most of the high velocity atoms in the Maxwellian distribution diffuse out of the molasses and hence cannot be cooled. Magneto-optical traps (MOT) use a combination of optical and magnetic fields to create a position-dependent force (‘trap’) in addition to the damping force. By choosing a proper polarization of the molasses beams and adding a magnetic field gradient to the system, we introduce a restoring force that always pushes the atoms towards the trap minimum. While an optical-molasses can be created using both linear and circular polarized beams (§. 2.3), a MOT requires counter-propagating beams of opposite circular polarizations ( $\sigma^+ - \sigma^-$ ). MOTs have higher capture velocities compared to the molasses technique and therefore, are usually loaded directly with warm atomic vapours. It must, however, be mentioned that both the cooling and trapping forces in a MOT come from radiation. While the magnetic field in a MOT is too weak to confine the atoms by itself, it creates position dependent Zeeman shifts in atoms, which in turn cause an imbalance in the scattering force of the laser beams.

In practical experiments with cold atoms, MOTs are used in the first stage of atom collection and cooling. It begins by loading hot atoms into a 2D-MOT, wherein, atoms are trapped and cooled radially, with no force along the transverse axis. This produces a collimated flux of atomic beam in the transverse direction. The 2D-MOT stage is followed by the 3D-MOT wherein atoms experience cooling and trapping in all six directions. The molasses-phase proceeds the 3D-MOT stage. In most of the alkali atoms, the same

cooling and repump beams are used to implement both the MOT and molasses phases, differing only in their detunings and intensities. For cooling  $^{39}\text{K}$ , the MOT beams are generated on the D2-line, as described in §. 3.6.1.

The position-dependent component of the optical force arises due to the magnetic field gradient, which is generally created by passing current in opposite directions in a pair of coils. The coils are then said to be in an ‘anti-Helmholtz’ configuration, and produce a quadrupole-magnetic field. At the center of the two coils, the magnetic fields are equal and opposite and hence cancel out. At small distances away from the center, there is a uniform gradient of the magnetic-field. In the presence of the magnetic-field, the  $2F+1$  fold degeneracy of the hyperfine levels is lifted and the energy-shift for each level, to first order perturbation, can be written as<sup>4</sup>:

$$\Delta E = \mu_B m_F g_F B \quad (3.17)$$

Here the magnetic moment of the atom is  $\hat{\mu} = -\frac{\mu_B g_F}{\hbar} \hat{F}$ ;  $\hat{F}$  is the total angular momentum operator;  $\mu_B$  is the Bohr-magneton;  $g_F$  is the Lande g-factor and  $m_F \hbar$  is the eigenvalue of the  $\hat{F}_z$  operator which is the projection of  $\hat{F}$  in the direction of the applied magnetic-field.

We next illustrate the working principle of a MOT by considering the atomic motion in one-dimension only. This can be easily extended to two and three dimensions.

### 3.7.1 Operating Principle: One-Dimensional Model

We consider two counter-propagating laser beams in a  $\sigma^+ - \sigma^-$  configuration, as shown in Fig. 3.13, that are red-detuned by  $\delta$  with respect to the  $|F = 0\rangle \rightarrow |F' = 1\rangle$  transition (chosen for simplicity). These lasers are red-detuned to give damping by the usual optical-molasses mechanism. The anti-Helmholtz configuration of the MOT coils result in zero magnetic-field at the center, that is,  $B = 0$  at  $z = 0$ . At small displacements from  $z = 0$ , the field increases linearly and can be written as:  $B(z) = B_0 z$ , where  $B_0$  is a scalar and, without the loss of generality, can be assumed positive. The applied  $B(z)$  lifts the degeneracy of the ground and excited hyperfine levels: there is one Zeeman sublevel  $m_F = 0$  in the ground state and three sublevels in the excited state:  $m_{F'} = 0, \pm 1$ . As a function of atomic position along  $z$ , the  $m_{F'} = 1$  sublevel is shifted upward (downward) in energy for  $z > 0$  ( $z < 0$ ), and vice versa for the  $m_{F'} = -1$  sublevel. For atoms moving along

<sup>4</sup>This is justified since the magnetic fields inside a MOT are weak.

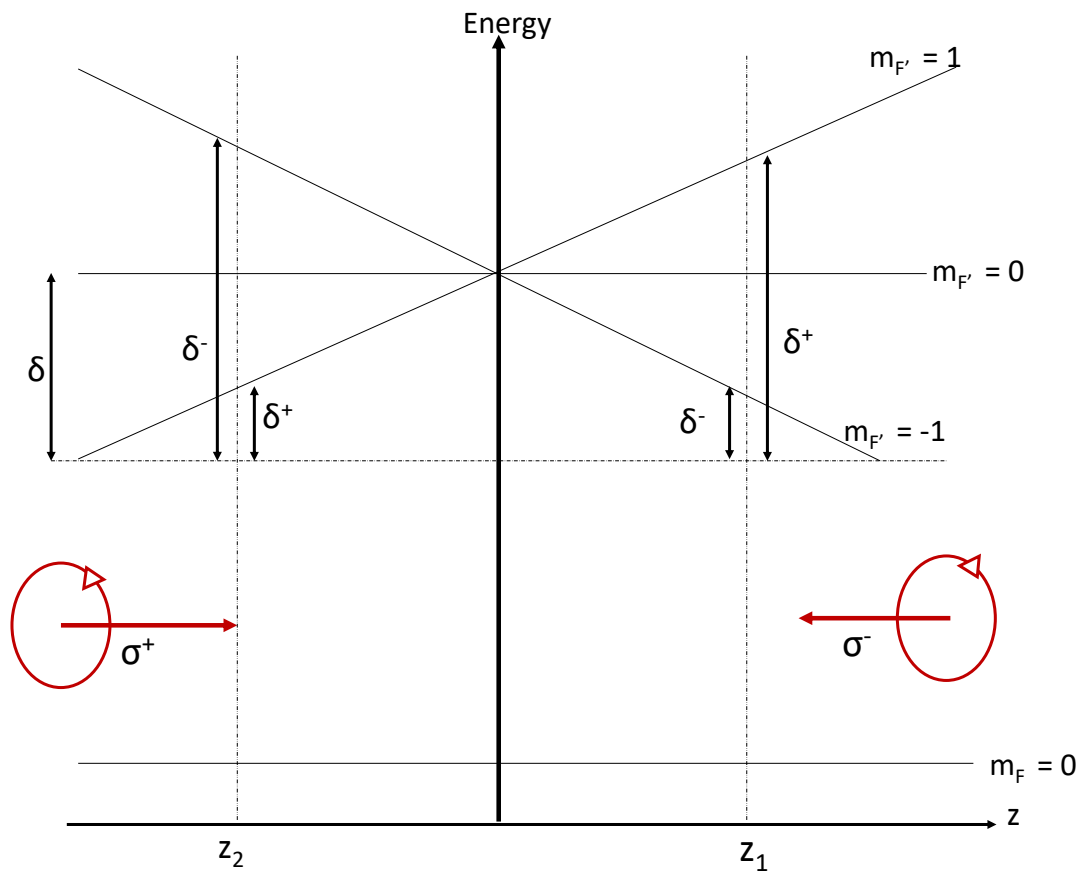


FIGURE 3.13: Operation of a MOT in 1-dimension for a hypothetical  $|F = 0\rangle \rightarrow |F' = 1\rangle$  transition. Adapted from [18]. The restoring force that pushes the atoms towards the center arises due to the imbalance in the scattering forces from the two laser beams that have opposite circular polarizations. The imbalance occurs due to the unequal Zeeman energy-shifts for the two beams. The magnetic-field is zero at the trap center. At small displacements from the center, the field varies linearly with position. Thus, the Zeeman splitting of the excited  $m_{F'} = \pm 1$  sublevels also vary with position of the atom with respect to the trap center. Two arbitrary positions right and left of the center are shown at  $z_1$  and  $z_2$  respectively. Atoms moving towards the right are more resonant with  $\sigma^-$  beam and thus, experience a net scattering force towards the left. Similarly, atoms that move towards  $z < 0$  are pushed towards the right as they are more resonant with  $\sigma^+$ .

$z > 0$ , the  $m_{F'} = -1$  gets closer to resonance while  $m_{F'} = 1$  is further detuned from resonance. Hence, an atom in the ground  $m_F = 0$  state is more likely to get excited to the  $m_{F'} = -1$  level by absorbing the counter-propagating  $\sigma^-$  beam, and are hence pushed towards  $z = 0$ . Similarly, atoms moving along  $z < 0$  see the  $m_{F'} = 1$  level closer to resonance and thus absorb more from the counter-propagating  $\sigma^+$  beam, thereby getting pushed towards the center.

As an example, we can calculate the effective detunings for the two laser beams, seen by an atom that is at some displacement  $z$  from the MOT center. In general, the effective resonant frequency due to Zeeman shift, can be written as:

$$\omega_{\text{Res}} = \omega_0 + (g_{F'}m_{F'} - g_F m_F)\mu_B B(z)/\hbar \quad (3.18)$$

where  $g_F, m_F$  are for ground state while  $g_{F'}, m_{F'}$  for excited state sublevels;  $\omega_0$  is the resonant frequency in the absence of the magnetic field when the levels are degenerate. In our specific example,  $m_F = 0$  and  $m_{F'} = \pm 1$ , and thus:

$$\omega_{\text{Res}}^{\pm} = \omega_0 \pm g_{F'}\mu_B B(z)/\hbar \quad (3.19)$$

where  $\pm$  indicates  $\sigma^{\pm}$ . Further, we denote the effective detunings of the  $\sigma^{\pm}$  beams as  $\delta^{\pm}$ . Consider an atom with velocity  $+v$  towards the positive  $z$ -axis. The Doppler-shift is taken as  $-\vec{k}\cdot\vec{v}$ , with  $\vec{k}$  being the wave-vector of the laser beam. Then, the atom 'sees' the  $\sigma^+$  beam at the detuning:

$$\begin{aligned} \delta^+ &= \omega_L - kv - \omega_{\text{Res}}^+ \\ &= (\omega_L - \omega_0) - kv - \frac{g_{F'}\mu_B B(z)}{\hbar} \\ &= \delta - kv - \frac{g_{F'}\mu_B B(z)}{\hbar} \end{aligned} \quad (3.20)$$

Here,  $\omega_L$  is the laser-frequency and  $\delta = \omega_L - \omega_0$  is the detuning from resonance in the absence of Zeeman splitting; for the same atom,  $\sigma^-$  appears to be detuned at:

$$\delta^- = \delta + kv + \frac{g_{F'}\mu_B B(z)}{\hbar} \quad (3.21)$$

As  $\delta < 0$ , we see that  $\delta^+$  gets more negative and hence  $\sigma^+$  is further detuned from resonance. On the other hand,  $\delta^-$  becomes less negative implying that  $\sigma^-$  shifts closer to resonance. The atoms therefore absorb more from  $\sigma^-$ , experiencing a net scattering force towards the left. Similar arguments can be made for atoms that move towards  $z < 0$ .

### 3.7.2 Getting the cooling beams into the MOT chambers

In our quantum-simulation setup, the MOT stages in two and three dimensions, are implemented in two separate chambers referred to as the ‘loading’ and ‘science’ chambers respectively. The loading / 2D-MOT chamber is maintained under high vacuum with pressure varying between  $10^{-8}$  to  $10^{-10}$  Torr. Collection of atomic flux from warm atomic-vapour is done in this chamber. The science chamber is to be used for all other stages of the experiment, namely, 3D-MOT; D2-D1 molasses; magnetic and optical-dipole trapping; evaporative-cooling; customizing interactions via spin-orbit coupling and feshbach resonance etc. The chamber is maintained under ultra-high vacuum with pressure  $\leq 10^{-12}$  torr. Differential pumping between the loading and science chamber helps in maintaining the two at different pressures. Our setup is designed to work with dual atomic species of  $^{87}\text{Rb}$  and  $^{39}\text{K}$  and a description of the UHV system; construction of 2D and 3D-MOT chambers; design of MOT coils; magnetic-field and current control for the MOT coils as well as the laser system for Rb, is done in [22].

Having discussed the lasers and optics for cooling  $^{39}\text{K}$ , we now briefly discuss how the D1 and D2 cooling (and repump) beams for  $^{39}\text{K}$  as well as the corresponding beams for  $^{87}\text{Rb}$  are introduced into the MOT chambers. For this purpose, customized fiber-beam splitters (**Evanescent Optics**) of 4 by 4 and 4 by 6 are used for 2D and 3D-MOT respectively, as shown in figures. 3.14 and 3.15. The fiber-splitters are polarization maintaining, intensity splitters type. Each splitter has four inputs: two for rubidium beams and 2 for potassium beams. For each species, there is one ‘master’ input for cooling (trap) beam and another input for repump beam. As laser-cooling K using gray-molasses requires cooling beams on both D2 and D1 lines, these beams are first combined in free space using interference filters (Fig. 3.2) before they are fiber-coupled. Moreover, as described in §. 3.6.2, the D1-cooling and repump frequencies are not spatially separated. Thus, the master-input for K consists of D2-cooling and D1 cooling + repump frequencies. The K-repump input, however, contains only the D2 repump frequencies since the corresponding D1 component is already present in the master input.

From each input, 0.5 % of the optical power is used for monitoring via separate fiber outputs. The monitored intensity can be used in conjunction with an electronic servo to maintain constant power in the cooling beams, as discussed in §. 3.8. The master input is equally divided into 4 and 6 outputs for the 2D and 3D-MOT respectively. The repump input in each case,

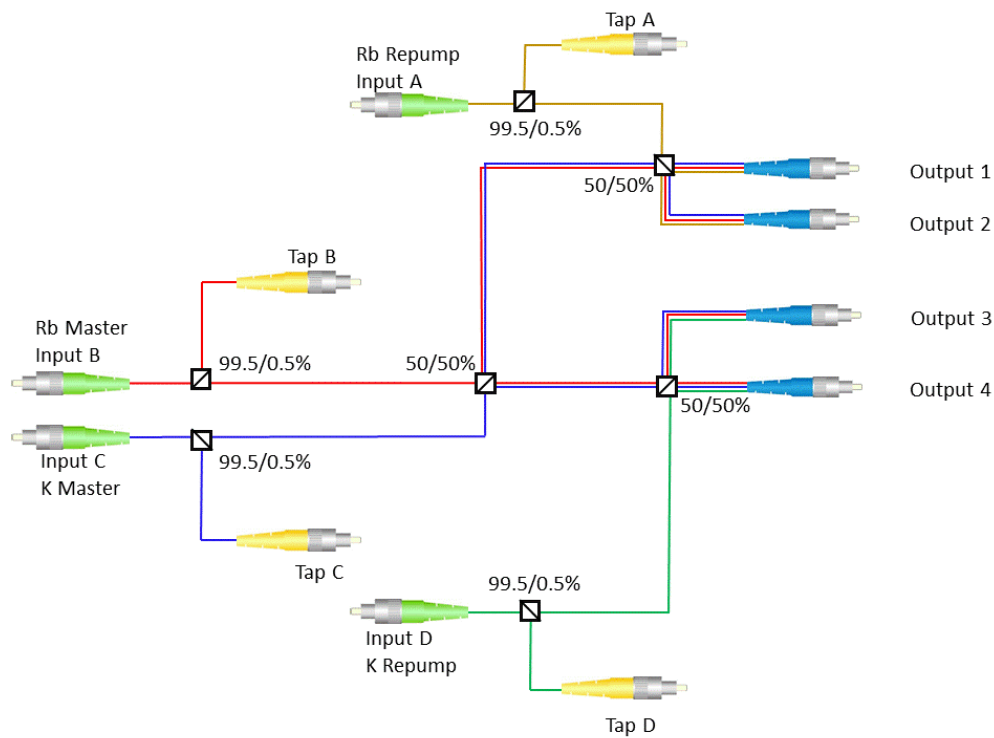


FIGURE 3.14: 4 by 4 fiber-beam-splitter for 2D-MOT. Image reproduced from [22]. The fibers are polarization-maintaining, normal beam-splitter fibers. They are customized to support both K and Rb experiments. Inputs labeled A and B contain cooling and repump frequencies respectively for D2 line (780 nm) in  $^{87}\text{Rb}$ . Input labeled C contains cooling frequencies for both D2 and D1 (767 and 770 nm) lines in  $^{39}\text{K}$ . The D1-repump frequency is also present. The D-input contains D2 repump frequency for K. The intensity split ratios are indicated.

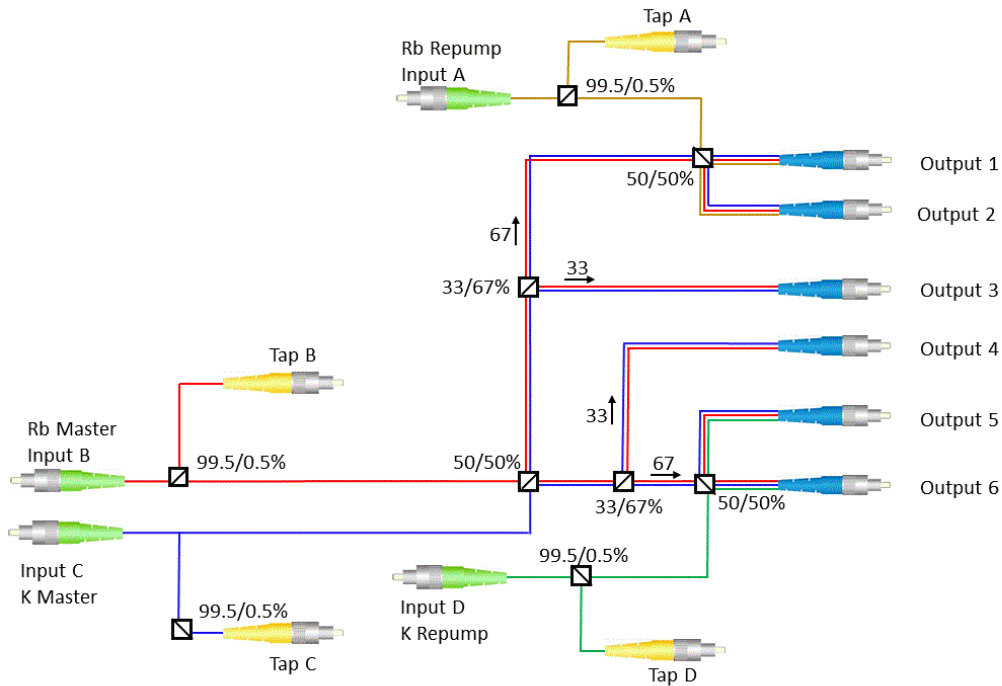


FIGURE 3.15: 4 by 6 beam-splitter for 3D-MOT. Image reproduced from [22]. The fibers are polarization-maintaining, normal beam-splitter fibers. They are customized to support both K and Rb experiments. Inputs labeled A and B contain cooling and repump frequencies respectively for D2 line (780 nm) in  $^{87}\text{Rb}$ . Input labeled C contains cooling frequencies for both D2 and D1 (767 and 770 nm) lines in  $^{39}\text{K}$ . The D1-repump frequency is also present. The D-input contains D2 repump frequency for K. The intensity split ratios are indicated.

is equally divided into two outputs. The four output beams, for the 2D-MOT, enter the loading glass chamber through four directions that are labeled as ‘Top’, ‘Bottom’, ‘North’, ‘South’ in our setup. The six output beams, for the 3D-MOT, enter the science chamber through six directions labeled, ‘Top’, ‘Bottom’, ‘North-East’, ‘South-East’, ‘North-West’ and ‘South-West’. The beams initially have linear polarization state and must be converted to circularly polarized, to be able to implement the MOT. Quarter-waveplates are used at each entry point of the glass windows for this purpose.

### 3.8 AOM based Laser Power Stabilization

We describe a standalone feedback electronic circuit that can be used to deliver constant laser power at various stages of our experiment. The feedback circuit implements a proportional-integral (PI) control logic inside a ‘field-programmable gate array (FPGA)’ chip. Since the feedback action is based on the power / intensity of the laser beams, it is independent of the laser

Parent Laser Frequency	Transitions ( $F \rightarrow F'$ )	$\Delta f$ (MHz) <sup>a</sup>	Generation
Trap Laser at 767 nm $(\omega_{C,\text{laser}}^{D2} = \omega_C^{D2} - 160 \text{ MHz} - \delta_C^{D2})$	2D-MOT Cooling ( $2 \rightarrow 3'$ ) 3D-MOT Cooling ( $2 \rightarrow 3'$ ) Optical Pumping ( $2 \rightarrow 2'$ ) Push Beam ( $2 \rightarrow 3'$ ) Imaging ( $2 \rightarrow 3'$ )	+ 160 + $(139 + \delta_C^{D2})$ > 160 + $(160 + \delta_C^{D2})$	+1 diffracted order of the second pass of a double-pass AOM, centered at 80 MHz. Generated in the same way as the 2D-MOT cooling beam, but independently. 0 <sup>th</sup> order of the second pass of 2D-MOT AOM passed through another AOM (single-pass) centered at 77 MHz. +1 order of the second pass of a double-pass AOM, centered at 90 MHz. 0 <sup>th</sup> order of the second pass of corresponding 3D-MOT AOM passed through another AOM (single-pass) centered at 98 MHz.
Repump Laser at 767 nm $\omega_{D2,\text{laser}}^{D2} = \omega_R^{D2} - 80 \text{ MHz} - \delta_R^{D2}$	3D / 2D-MOT ( $1 \rightarrow 2'$ )	+ 80	+1 diffracted order of a single-pass AOM centered at 80 MHz is taken and split into 2D and 3D-MOT repump beams.
Gray-Molasses Laser at 770 nm $(\omega_{\text{laser}}^{D1} = \omega_C^{D1} - 107.8 \text{ MHz})$	3D-MOT Cooling ( $2 \rightarrow 2'$ ) 3D-MOT Repump ( $1 \rightarrow 2'$ ) 2D-MOT Cooling ( $2 \rightarrow 2'$ ) 2D-MOT Repump ( $1 \rightarrow 2'$ )	> + 107.8 > + 570 MHz > + 107.8 MHz > + 570 MHz	+1 diffracted order of the second pass of a double-pass AOM, centered at 60 MHz. Present in the 3D-MOT cooling beam, however, is frequency shifted using an EOM that is operated at 461.7 MHz (the ground hyperfine splitting in 39K). 0 <sup>th</sup> order of the second pass of corresponding 3D-MOT AOM is passed through another AOM which is also centered at 60 MHz. The positive first order of this single pass is used for cooling during the 2D-MOT on the D2 line. Present in the 2D-MOT cooling beam, however, is up-shifted in frequency using EOM at 461.7 MHz.

TABLE 3.4: A summary of frequencies for exciting various transitions on the D2 and D1 lines. To fix the center-frequencies of push-beam, optical pumping and imaging AOMs, we chose  $\delta_C^{D2}$  to be  $3\Gamma$  which is  $\sim 18$  MHz. This can be done by locking the trap laser to a beat frequency of  $\sim 538$  MHz (Eqn. 3.13). Also, the  $>$  sign against a  $\Delta f$  indicates the frequency has to be blue-detuned from the corresponding transition.

<sup>a</sup>The values indicated are at the time of setting up the optics and might have to be changed during the optimization procedures when the cooling experiments are actually run. However, the change would not be too drastic from these set values.

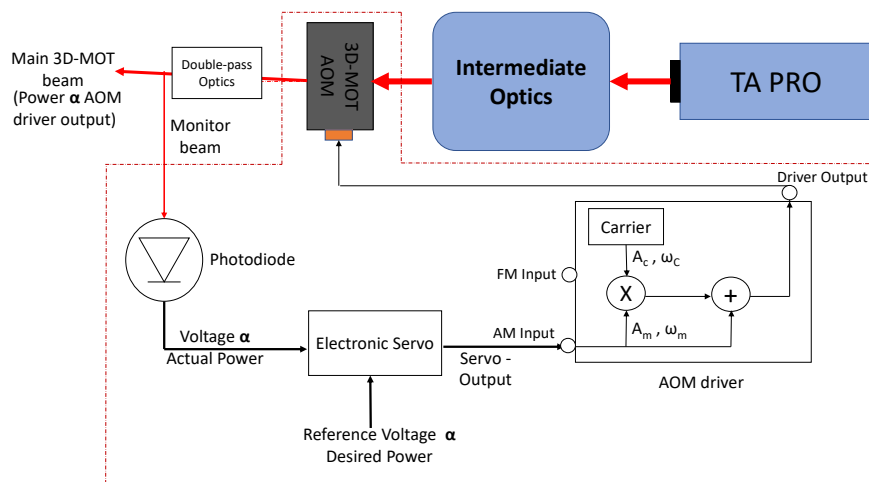


FIGURE 3.16: Feedback scheme for delivering constant power in the 3D-MOT cooling beam. The feedback servo is a standalone circuit that can be used at any stage of our experiment. The feedback loop consists of an AOM, a photodiode (PD), a proportional-integral (PI) controller and the AOM driver unit. The output of the PD is proportional to the actual power in the diffracted beam. Inside the servo loop, the PD signal is compared with a reference signal. The reference signal is provided externally and is proportional to the desired power. The difference between the two voltages give an error-signal. When the PD voltage equals the reference signal, the error-signal is zero and no correction is applied. A non-zero error-signal results in a corrective signal, that is applied at the AM input of the AOM driver. This input then changes the RF power that drives the AOM, in such a way, that the diffracted beam intensity matches with the reference intensity.

wavelength and hence, can be used with either K or Rb beams. It is important to mention here that our lasers by themselves are a source of constant power. However, to transport the laser beams at various stages of our experiment, we use fiber-couplers, and, it is quite common for the coupling efficiency of such fibers to change / degrade over time. This can occur due to fluctuation in either the intensity of the beam (traveling inside the fiber) or due to misalignment of the polarization axis of the incoming beam with the principal axis of the fiber. While we minimize the latter effect by using polarization-maintaining (PM) fibers in our setup, the former can still occur due to changes in external conditions such as temperature and stress. Hence, active intensity stabilization is needed.

One application where this circuit is used is shown in Fig. 3.16, where we want a constant laser intensity, in the D2-cooling beam, to be delivered to the 3D-MOT chamber. As discussed in §. 3.6.1, the cooling transition is generated

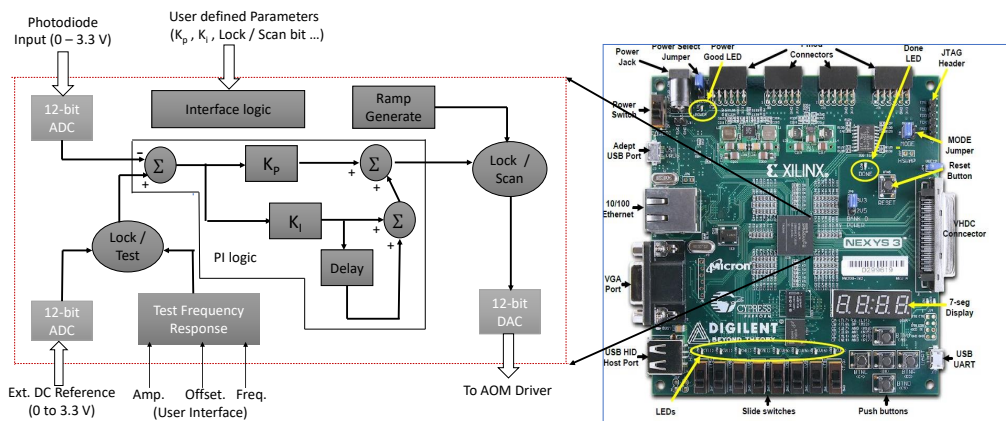


FIGURE 3.17: On the left is shown the feedback logic implemented inside an FPGA chip, which is a part of an evaluation board from Digilent Inc. The board is shown on the right (image taken from Digilent’s website). The shaded components are the HDL logic blocks that mimic the behavior of the required hardware device(s).  $K_P$  and  $K_I$  are the proportional and integral gains respectively which can be tuned by the user via C++ based GUI. The GUI can also enable / disable some modules so as to operate in three different modes that are described in text. When enabled, the output from the PI controller block goes to the AOM driver which in turn controls the power in the beam diffracted off the AOM.

by appropriately shifting the frequency of the laser beam using an ‘acousto-optic modulator’. The shifted frequency is contained in the diffracted order. The power of the diffracted beam is proportional to the amplitude of the RF signal that drives the AOM. This forms the basis of power stabilization: after being coupled to the 3D-MOT fiber, about 0.5 % of the main beam (Fig. 3.15) is tapped and used as a ‘monitoring beam’. This is then incident onto a photo-detector. The detector outputs a voltage that is proportional to the intensity of the incident light. This voltage is the ‘working signal’ which goes to the input of the PI servo-controller. The controller compares the photodiode voltage with a reference voltage (which is proportional to the desired laser intensity) to create an ‘error-signal’. Based on the magnitude and sign of this error-signal, the controller generates a correction signal which is the sum of two components: the first component is proportional to the amount of error signal at that instant of time, that is the current error, and is called the proportional component; the second component is the integrated value of error-signal upto the current instant of time, and is called the integral component. The PI correction is applied to the ‘amplitude-modulated (AM) input’ of the AOM driver. The output RF power of the driver is proportional to the amplitude of the AM input signal, which in turn controls the intensity of AOM-diffracted beam. In this way, a closed feedback loop is established.

The PI-controller is implemented as a digital logic inside an FPGA chip. A detailed description on the operation of FPGA logic and design is beyond the scope of this thesis. However, to put it briefly, such a chip consists of a matrix of 're-configurable logic blocks (CLB)' which are realized using transistors; logic gates (AND, OR, NAND, XOR etc.); n-input look up tables, flip-flops etc. and can be used to implement various combinational and sequential logic functions, that could range from a simple binary counter to a sophisticated microprocessor. There are several advantages of using FPGA based devices: firstly, they are re-configurable, that is, they can always be programmed to add or modify some functionality within an existing design, without the need of any additional hardware or soldering. All it requires is to 'burn' the new program inside the chip so as to replace the existing one. Secondly, they are concurrent in nature, that is different programmable blocks inside the chip are executed at the same time (parallel computing), and hence are faster compared to a microcontroller. Thirdly, these devices are inherently digital and thus better immune to noise, compared to an analog device.

Next, a brief technical description of the hardware and software components used is provided. The feedback logic is implemented inside an FPGA chip which is a part of an evaluation board from Digilent Inc. (**Digilent : Nexys3**). The on-board chip itself is manufactured by Xilinx (**Xilinx : Spartan 6**). The required hardware behavior of a proportional-integral control system is logically mapped inside this FOGA chip using a 'hardware description language (HDL)' called **VHDL**. To 'burn' the VHDL programs inside the chip, we use the design tool from Xilinx, called '**ISE WebPack 14.2**'. Shown in Fig. 3.17 are the various logic modules (shaded blocks), written in VHDL programming language, that are burned inside the spartan 6 chip. The input signals to the FPGA chip are the photodiode voltage and the reference signal. The reference voltage can either be provided using a computer or through an external stabilized power-supply. To bridge the gap between these analog signals and the digital FPGA chip, two analog-to-digital converters (ADC) are used. For this purpose, **AD7476 : Analog Devices**, a 12-bit unsigned ADC is used which receives an analog signal and converts it into a 12 bit binary sequence. The 12-bit data is then transferred inside the FPGA chip using a 3 wire 'serial peripheral interface (SPI)' protocol [37], that is implemented in a VHDL module. Likewise, the control signal generated inside the FPGA goes to the AOM driver after a digital-to-analog conversion (DAC). The DAC used is **DAC121S101 : Texas Instruments** which is a 12-bit unsigned DAC IC. SPI-protocol is used for data transfer from the Spartan 6 chip to the DAC.

The board as well as the ADC-DAC IC's are operated at 3.3 V and the input signals must not exceed this rating.

To be able to dynamically change the controller gains, we interface the FPGA chip with a computer, through a graphical-user interface (GUI) developed in **Visual C++**. The communication between the computer and the chip is done by implementing a 'universal-asynchronous-receiver-transmitter (UART)' system as outlined in [38]. Another utility of the GUI is to enable / disable certain logic modules inside the chip, thereby allowing us to operate the FPGA in different configurations: as for example, we can analyze the frequency response of the feedback logic by choosing the reference input as a DC offset and introducing small modulations around this offset point. The offset value, modulation-amplitude and modulation frequency are provided via GUI and the associated signal is internally generated. The idea behind this configuration is to test how fast the loop can respond to the changing reference and in turn, determine the bandwidth of the loop. Based on this, the loop bandwidth was determined to be around 12 kHz. In another configuration, we simply generate a ramp signal ranging from 0 to 3.3 V to be sent to the AOM driver and monitoring the photodiode signal. This can be used for calibrating the photodiode voltage as a function of AM input voltage and to find an appropriate value for the reference setpoint. Finally, the third configuration is when we want to close the loop and match the photodiode signal with the reference signal. The PI logic is enabled and the corresponding gains can be dynamically tuned via GUI. It must again be reiterated here that the shaded blocks in Fig. 3.17 are not the hardware components but 'logical' components that are mapped inside the FPGA upon burning the appropriate HDL code. In the feedback scheme discussed here, these blocks implement specifically, (1) the communication interface between the FPGA chip and ADC/DAC peripherals and between FPGA registers and the C++ based GUI (2) the proportional-integral control (3) frequency response analysis logic (4) generate a ramp signal in open-loop mode.

Lastly, we also use some additional hardware electronics (accessory circuits) at the input and output stages of the design, that are shown in Fig. 3.18. On the input side, we use two op-amp buffers that are of unity gain each, to transfer the analog signals from the photodiode and external reference source to the ADC chips. These buffers are realized using a dual op-amp IC **OP275**. The digital control voltage generated in the FPGA is converted into an analog signal via DAC chip. This analog signal ranges between 0 to 3 V. As the AM input of the AOM driver circuit can take a maximum of 1 V, the DAC output

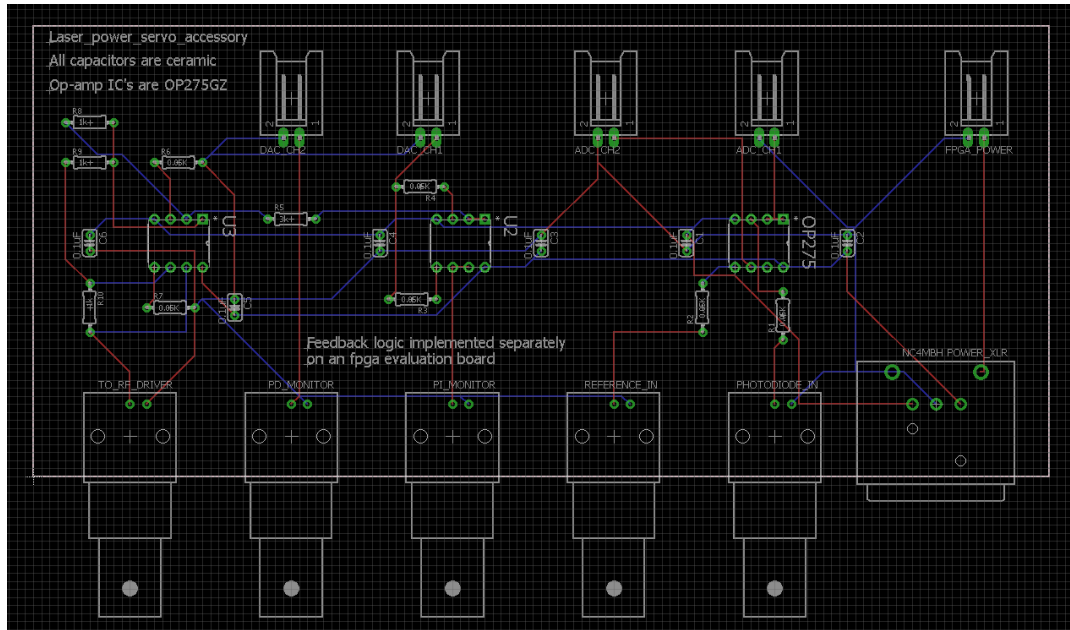


FIGURE 3.18: PCB board layout for the accessory circuits at the input and output stage of the feedback. The circuits include op-amp based difference amplifiers and buffers.

must be attenuated such that the signal going to the driver does not exceed 1 V. Also, we would like to monitor the following signals: (1) the actual control voltage generated by the feedback loop before it is attenuated and (2) the stabilized photodiode voltage. The DAC IC used in our design has two DAC channels: one of them is programmed to carry the signal straight from the photodiode ADC input and goes directly to the monitoring scope. The other DAC channel carries the control voltage and drives two op-amps. One op-amp is used in a unity gain buffer configuration to monitor this signal. The second op-amp attenuates this signal by a factor of  $1/3$  in an inverting feedback configuration. Since, the attenuated signal is inverted, it is passed through another inverting op-amp with a unity gain. The final output then goes to the AOM controller input.

## **Part II**

# **A Novel Quantum Memory Protocol**

# List of Symbols

Symbol	Meaning	Units if applicable
$ g\rangle,  s\rangle$	Two ground states of a 3-level atomic system	
$ e\rangle$	Excited state	
$\mu_{eg}$	Electric dipole moment between $ g\rangle$ and $ e\rangle$	
$\hat{P}$	Macroscopic polarization operator on $ g\rangle \rightarrow  e\rangle$ transition	
$\hat{S}$	Macroscopic spin-wave operator on $ g\rangle \rightarrow  s\rangle$ transition	
$\hat{E}$	Electric field operator describing the envelope of a quantum mechanical electric field	
$\Omega_C$	Rabi-frequency of control field	$2\pi \times \text{MHz}$
$\Gamma_{ge}$	Spontaneous emission rate between $ e\rangle$ and $ g\rangle$	$2\pi \times \text{MHz}$
$\gamma_{ge}$	Decay of coherence between $ e\rangle$ and $ g\rangle$	$2\pi \times \text{MHz}$
$\gamma_{gs}$	Decay of coherence between $ g\rangle$ and $ s\rangle$	$2\pi \times \text{MHz}$
$g$	Characterizes the atom-photon coupling strength	$s^{-2}$
$N$	Number of atoms in the ensemble	
$d$	Peak optical depth	
$\bar{d}$	Effective-optical-depth	
$F$	ATS-Factor	
$A_C$	Pulse area of control field	
$\tau_{\text{FWHM}}$	Duration of probe (signal) pulse at FWHM	ns
$B_{\text{FWHM}}$	Bandwidth of the signal pulse at FWHM	MHz
$\eta_F$	Memory efficiency in forward propagation	
$\eta_B$	Memory efficiency in backward propagation	
$\mu_{\text{abs}}$	Collective absorption probability of a single excitation by an atomic ensemble	
$\mu_{\text{re}}$	Collective re-emission probability of an ensemble	
$\mu_W, \mu_R$	Polarization mediated transfer efficiency during writing and reading stages	

## Chapter 4

# A broadband optical quantum memory based on Autler-Townes absorption

In this part of the thesis, I describe a novel quantum memory protocol that we came up with in our lab, which allows for the storage and on-demand retrieval of broadband light pulses, together with a high speed and robust signal processing capability. The storage and retrieval processes rely on the coherent absorption of a weak signal field in the presence of a strong control field via dynamically controlled ‘Autler-Townes Splitting (ATS)’. Both the signal and control fields are on resonance and are often termed as the probe and coupling fields, respectively. The ATS effect based on ac Stark light shifts, is a well-known optical phenomenon, yet, had been unexplored till now in its utility as a practical light storage mechanism. Our lab experimentally demonstrated a proof of principle of the ATS memory by storing nanoseconds long optical pulses upto a period of 1 microsecond, in a  $\Lambda$ -type three level system of cold Rb atoms [5]. In principle, it should be possible to implement this protocol in any three level system. The term ‘storage’ here implies the transfer of coherence from the optical signal field (photonic mode) to a collective ground state spin excitation, which is delocalized over all constituents in the storage medium (cold Rb atoms in our case). Conversely, the term ‘retrieval’ refers to the transfer of coherence from the stored spin excitation, back to the photonic mode. In both the processes, the coupling between the photonic and spin wave modes is mediated by the control field.

This chapter is organized as follows: In §. 4.1 we begin by listing some practical applications involving the use of quantum memories. At the heart of a quantum memory are the light-matter interactions and thus, several material media have been explored ranging from a single atom in a high Q-cavity to an ensemble of warm atomic vapor to laser-cooled and trapped

atoms to solid state systems with ‘atom like defects’. This is followed by a qualitative description of some popular light storage protocols (§. 4.2). As a preface to the ATS protocol, we briefly discuss the two different but confusingly similar EIT and ATS phenomena (§. 4.3). Finally, we discuss our newly proposed light storage scheme (the ‘ATS protocol’) based on the absorption of the input signal by the Autler-Townes absorption lines (§. 4.4). This description is adapted from our work in [5], where both the theoretical and the experimental demonstration of this scheme are presented. In this thesis, I describe my contribution towards the theoretical understanding of the ‘ATS-storage’ protocol. I present the results of numerical analysis of the Maxwell-Bloch equations in the ATS regime, which show the light storage and retrieval processes. These simulations enable us to relate the dynamics of our memory to certain phenomenological parameters, that are experimentally accessible. Hence, a careful choice of these parameters results in optimal memory efficiencies. We start with the simplified Maxwell-Bloch equations for a  $\Lambda$ -type three level system driven by a weak signal and an intense control field (§. 4.4.1) and study the performance of our memory based on different configurations of the control field (§. 4.4.2). Finally, we also discuss the factors that affect the efficiency of the ATS memory scheme (§. 4.4.3).

## 4.1 Quantum Memories

In order to avoid confusion between using light and photons, we note that in quantum optics, an electromagnetic field can be considered to be a set or collection of harmonic oscillators, with each oscillator defining a mode of the field. The energy of the field is then the total energy of all the modes comprising the field. The excitation of a mode is referred to as ‘a photon’.

A quantum memory serves as an interface between light and matter, in that it facilitates a coherent and reversible transfer of quantum information between the light field and the material. The ability to map the quantum state of light onto a long-lived excitation inside the medium (as for example, an ensemble of atoms) and an on-demand release of the same, makes a quantum memory, a viable synchronization tool for timing various processes occurring within a quantum processor, which are inherently probabilistic in nature and hence difficult to synchronise [39]. Similarly, quantum communication networks rely on light as the carrier of quantum information and make use of optical fibers for information transmission. Due to attenuation losses in such fibers, several trials are required to establish a successful link between two

nodes. This restricts quantum communication over short distances. This is not a serious issue in classical networks as the light pulse can be amplified using optical amplifiers or repeaters at intermediate distances. However, we cannot do the same for the quantum information as any act of measurement shall lead to its collapse. To mitigate this issue in quantum communication, researchers have developed ‘quantum repeaters’ [40, 41, 42], which are basically atomic quantum memories having long lifetimes to synchronize entangling operations over lossy networks. In nutshell, quantum memories shall play a key role in the implementation of future quantum technologies.

**Storage Media:** As stated earlier, writing or storing into the memory means transferring the photonic state onto some collective excitation state; similarly, reading out of the memory means reversibly mapping the earlier stored excitation back onto the photonic state. The most popular storage mechanisms involve writing the signal quantum state onto an atomic state. The success of writing into and reading out of the memory then depends on the strength of light-atom interactions. The interaction probability can be boosted, for example, by using a single atom trapped inside a high-finesse optical cavity [43]. In this case, the incident photon is reflected multiple times off the reflecting surfaces of the cavity thereby making multiple passes through the trapped atom, which in turn increases the absorption cross-section. Another approach that has become exceedingly popular is to increase the number of absorbers, that is, storing light in an atomic ensemble [44]. Researchers have investigated ensembles of warm atoms [45, 46], laser-cooled and trapped atoms [47] and even BECs [48]. What makes these ensembles fascinating is formation of a collective state: each atom in the ensemble has a finite probability of absorbing the incoming signal. The state of the optical excitation is thus delocalized over all atoms in the ensemble. Depending on the memory protocol used, this collective state can be a macroscopic spin excitation, that is, a superposition between the ground states over all atoms, as in the case of EIT and Raman based memories implemented on a three-level system. While the former is a dispersion-based memory and the latter is based on virtual absorption, in both the schemes there is no real absorption of the signal. Other techniques such as the ‘photon-echo’ based memories are primarily absorption based: here there is a collective absorption and a collective re-emission state, but no spin state. Photon-echo techniques are generally implemented in a medium that has a naturally large inhomogeneous broadening and as such solid state crystals doped with rare-earth ions [49] provide a suitable platform for such storage.

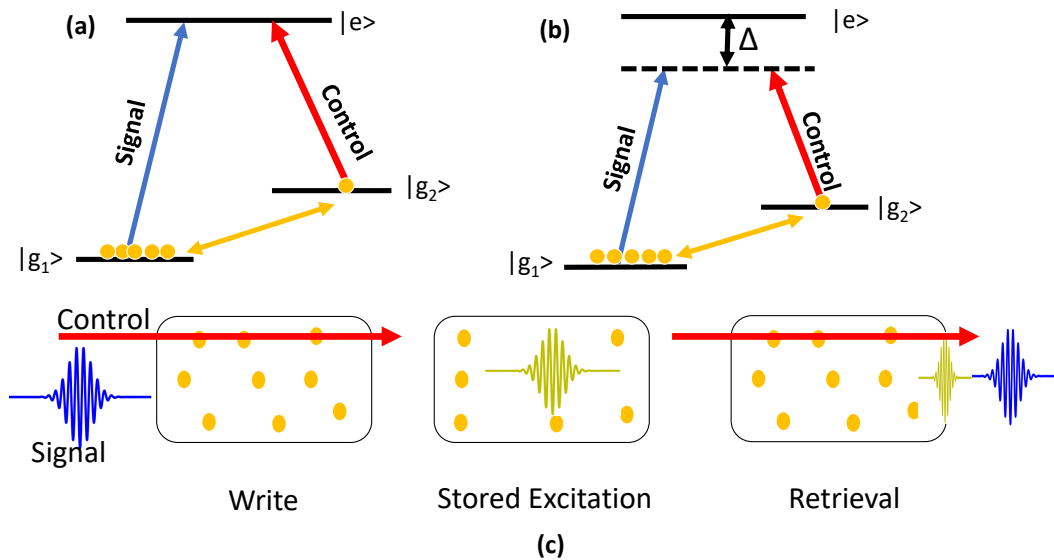


FIGURE 4.1: **(a)**: Electromagnetic induced transparency scheme in a three-level  $\Lambda$ -type atomic system, with a weak resonant probe and a strong resonant control field, coupling the two ground levels to a common excited level. The associated absorption and dispersion profiles of the probe signal are shown in figure. 4.2. **(b)**: Raman memory level scheme. The control and signal fields are far detuned with respect to the excited state. The control field induces a virtual excited level thereby causing a population transfer between the ground states. Note that in both cases, there is no actual excitation of atoms to the excited level  $|e\rangle$  and the population transfer from  $|g\rangle$  to  $|s\rangle$  occurs by adiabatic elimination of the excited level. The coupling between two ground states (spin coherence) is indicated by solid double arrow (yellow). **(c)**: Conceptual schematic of an EIT / Raman quantum memory. The control field mediates the mapping of the signal quantum state (blue) into a collective ground state coherence of the atoms inside the medium. Re-applying the control field after a certain storage time leads to re-mapping of the atomic coherence back into the optical field, resulting in re-emission of the signal.

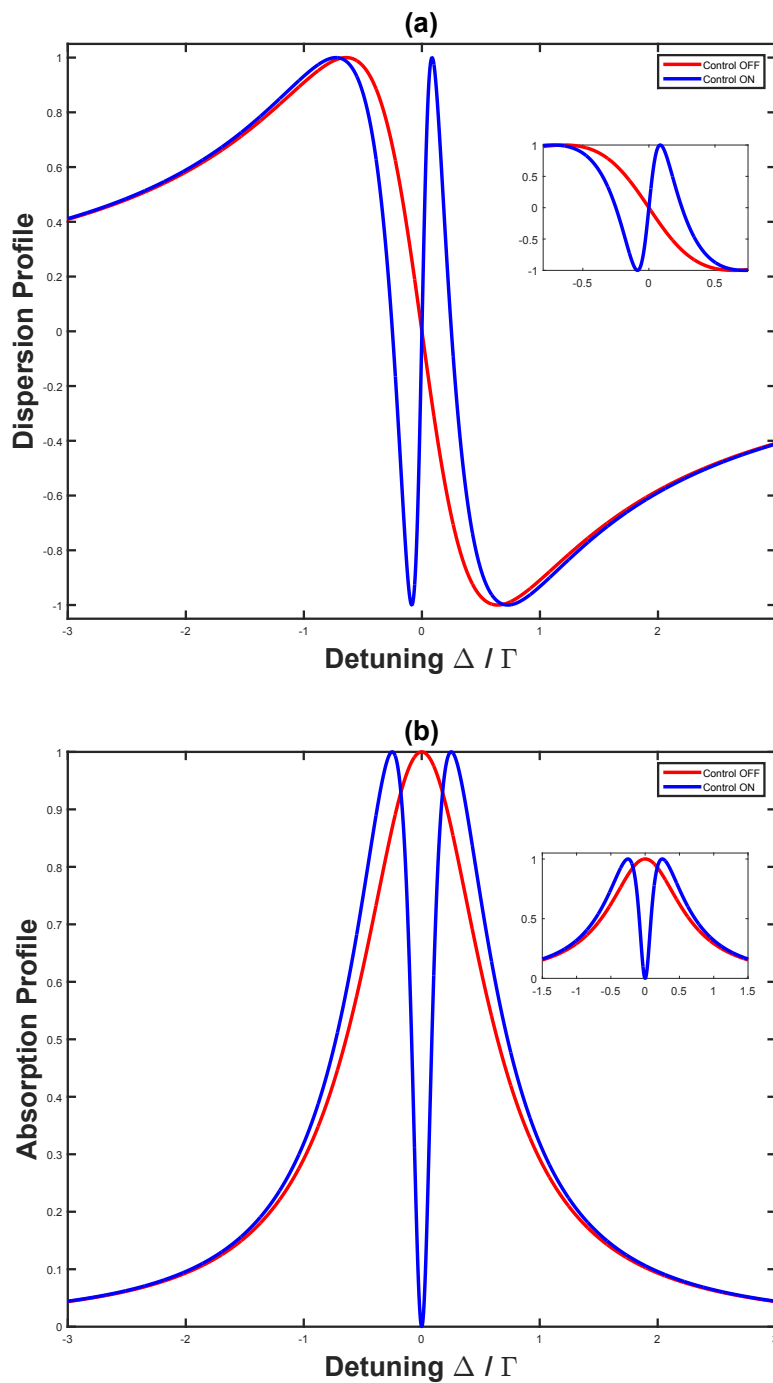


FIGURE 4.2: Dispersion and absorption profiles of a resonant probe passing through an optically active medium both with and without the control field. The presence of the control field renders the medium 'optically-transparent' and the resonant probe simply passes through it unattenuated. This is because the control field induces a narrow transparency window in the probe absorption spectrum. This is complemented by a steep change in the refractive-index of the medium, that reaches a value of unity at the center of the transparency window. The variation in the refractive index slows down the group velocity of the probe beam.

## 4.2 Popular Quantum Memory Protocols

A good review regarding the various experimental and theoretical works on different approaches to realizing a quantum memory can be found in [39]. In this section, we briefly describe some of the popular light storage schemes. Only a qualitative description is presented here<sup>1</sup>. They also serve the starting point for introducing the ATS protocol.

### 4.2.1 Electromagnetically Induced Transparency (EIT) based memory

First reported in [50], EIT is a non-linear optical effect whereby an absorbing medium becomes ‘transparent’ to a probe laser that is tuned on resonance to an atomic transition in the presence of a strong control laser field applied to the other transition (Fig. 4.1 (a)). In terms of using it as a light storage technique, we consider the three level  $\Lambda$  type system, whereby two ground states are coupled to the common excited state by a weak probe field (that carries the information to be stored) and a strong control field (that triggers the storage and readout processes). In the absence of the control field, the signal field is partially or completely absorbed in the medium. The presence of the control field induces a ‘transparency window’ and if the probe signal’s bandwidth fits inside this window’s frequency width, complete transmission is observed. Accompanied by this change in absorption is a large linear dispersion, which changes the refractive index of the medium, leading to a reduction in the group velocity [51] (Figure. 4.2 (a) - (b)). This is the famous ‘slow-light’ effect, which forms the basis of light storage: as the probe pulse enters the medium, it slows down, that is, gets spatially compressed, with the group delay inversely proportional to the control field intensity. By adiabatically switching off the control field, the group velocity is reduced to zero and the probe pulse gets mapped into the collective ground states spin coherence in the medium [52], often referred to as the spin wave. For retrieval, the control field is turned back on and the pulse resumes its propagation. It is important to emphasize that there is no excited state transition involved and the state of the optical excitation is directly mapped into the spin coherence.

---

<sup>1</sup>A rigorous description of these schemes is beyond the scope of this thesis.

### 4.2.2 Off-resonant Raman memory

The Raman memory scheme [53, 54] also requires a three-level system that is driven by a weak signal field and an intense control field. Both the probe and the control are (equally) far-detuned from the excited state transition, hence it is an off-resonant memory (unlike EIT where the fields are on resonance). In the absence of the control field, the probe signal is simply transmitted through the medium. In the presence of the control field, however, the atoms can absorb the probe signal via ‘virtual absorption’ and can be transferred to the other ground state via stimulated Raman scattering (Fig. 4.1 (b)). The resulting atomic population transfer leads to the spin-wave coherence between the two ground states. If the control field is now turned off, this excitation remains preserved inside the medium. Upon re-applying the control field, the spin wave is converted back into the photonic signal.

### 4.2.3 Photon-echo memory

Similar to EIT and Raman protocols, photon echo quantum memories also rely on transferring the coherence of the optical signal into a collective atomic coherence, however, unlike EIT and Raman, photon-echo memories are absorption-based and take advantage of the large inhomogeneous broadening of the medium. The broad absorption profile is composed of a large number of narrow absorption lines. Examples of such media include cryogenically cooled rare-earth ion doped crystals [55].

Photon-echo storage relies on absorbing the signal by an ensemble of atoms, each with slightly different transition frequency, followed by time reversing the absorption in a controlled manner, leading to re-emission of the signal. The re-emitted signal is known as the ‘echo’ [56]. A brief explanation is as follows [39]: we consider an ensemble of two-level atoms with ground and excited states given by  $|g\rangle$  and  $|e\rangle$  respectively. Assuming all atoms are initially pumped into the ground state, the initial state of the system is  $|\Psi_0\rangle = |g_1, g_2, \dots, g_N\rangle$ , where  $N$  is the number of atoms in the ensemble. An optical signal that enters the medium is delocalized to all atoms in the ensemble<sup>2</sup> and the collective state can be written as:

$$|\Psi(t)\rangle = \frac{1}{\sqrt{N}} \times \sum_j^N e^{i\delta_j t} e^{ikz_j} |g_1, \dots, e_j, \dots, g_N\rangle \quad (4.1)$$

<sup>2</sup>It means that each atom has an equal probability of absorbing the signal. Thus, there is no way to tell which atom would absorb it.

The summation runs over all atoms in the ensemble. Here  $z_j$  is the position of  $j^{\text{th}}$  atom;  $k$  is the wave vector of the signal field;  $\delta_j$  is the detuning of the transition frequency of the  $j^{\text{th}}$  atom with respect to the signal frequency. The superposition in Eqn. 4.1 accumulates different phases in time, since different atoms have different value of  $\delta$ . Atoms with detuning  $\delta_j$  acquire a phase of  $\delta_j t$  over a time interval  $t$ , and as such, the collective state begins to dephase. All photon-echo quantum memories employ some technique to rephase these states after some time so as to restore the atomic coherence, which then leads to a re-emission of the optical signal. Depending on the spectral distribution of the absorption lines within the broadened medium linewidth and the rephasing techniques used, photon-echo memory protocols can (broadly) be classified as: (1) Controlled Reversible Inhomogeneous Broadening (CRIB) protocol [57, 58] (2) Gradient Echo Memory (GEM) protocol [59, 60] and (3) Atomic Frequency Comb (AFC) [61, 62, 63].

### 4.3 Getting Started with Our Memory Scheme: The Autler-Townes Effect

Before we describe the ATS protocol itself, it is important to describe the fundamental basis of our memory scheme: the ‘Autler-Townes’ effect [64], also known as the ‘AC-Stark’ effect. We begin by highlighting the differences between two closely related physical processes that affect the transmission of a resonant probe field through an absorbing medium in the presence of an additional control or coupling field. The two physical processes are the ‘Electromagnetically Induced Transparency (EIT)’ (that was naively discussed in §. 4.2.1) and the ‘Autler-Townes Splitting (ATS)’.

In general, the two coherent processes can be described by considering a three-level  $\Lambda$ -type atomic system, as shown in Fig. 4.3 (a), which is resonantly driven on one transition (via ‘control’ field) and probed on the other (via ‘signal / probe’ field). The interaction of such a system has been studied in the ‘dressed-state’ picture where the basis states are the eigenstates of the ‘atom + radiation-field’ Hamiltonian [65, 66]. As the driving control-field is at a higher intensity than the signal probe, only the common excited level and the ground level that is addressed by the control are dressed / mixed, while the other ground level (addressed by the probe) remains ‘bare’, as shown in Fig. 4.3 (b). The states labeled  $|\pm\rangle$  in the figure are the superposition of bare

atomic states ( $|s\rangle$  and  $|e\rangle$ ) and are given by  $|\pm\rangle = \frac{1}{\sqrt{2}} (|s\rangle \pm |e\rangle)$ <sup>3</sup>. These are the eigenstates of the coupled atom-light system: the control field brings the energy of  $|s\rangle$  up to that of  $|e\rangle$  and the electric-dipole coupling lifts the degeneracy, splitting them  $\hbar\Omega_C$  apart, where  $\Omega_C$  is the Rabi frequency of the control field. This in-fact, is the manifestation of the AC-Stark effect. Hence, for a resonant control, the location of these dressed states in the frequency space is given by  $\delta \pm \Omega_C/2$ , where  $\delta$  is the detuning of the probe field with respect to  $|g\rangle \rightarrow |e\rangle$  transition.

Now, when the frequency of the weak probe field is swept such that it spans across the dressed state doublet (the  $|g\rangle \rightarrow |e\rangle$  transition in the bare atomic picture), two effects can affect the absorption-profile  $A(\delta)$  of the probe signal, depending on the splitting between the dressed states ( $\Omega_C$ ) relative to the dephasing / relaxation rates in the system. At low control intensities, the probe absorption vanishes at  $\delta = 0$ , exhibiting a sharp, narrow transparency window in the center. The transparency window is the result of destructive quantum interference between the transition amplitudes of the  $|g\rangle \rightarrow |+\rangle$  and  $|g\rangle \rightarrow |-\rangle$  transitions. The two transition pathways yield a net zero contribution to the dipole moment and hence there is no excitation. This is the EIT effect. At higher laser intensities (wide splitting between dressed state doublet), this interference effect is washed out and the probe absorption profile consists of two identical resonances that occur at the location of the two dressed states, that is  $\pm\Omega_C/2$  from  $\delta = 0$ . This is the ‘Autler-Townes’ effect.

To understand it mathematically, let us re-visit the three-level  $\Lambda$  type system, shown in Fig. 4.3(a). The two ground states  $|g\rangle$  and  $|s\rangle$  are dipole coupled to a common excited level  $|e\rangle$ , with dipole matrix elements  $\mu_{eg}$  and  $\mu_{es}$  respectively. The  $|g\rangle \leftrightarrow |e\rangle$  transition is excited through the probe signal (blue) and the  $|s\rangle \leftrightarrow |e\rangle$  transition through the control field (red) with Rabi frequencies  $\Omega_p \equiv |\mu_{eg}|E_p/\hbar$  and  $\Omega_C \equiv |\mu_{es}|E_C/\hbar$  respectively. Here  $E_p$  and  $E_C$  are the electric field amplitudes of the probe and control signal respectively. We further consider all atomic population to be in the ground state  $|g\rangle$ . This simply suggests that the atoms do not significantly affect the propagation of the strong control field which couples the  $|s\rangle \rightarrow |e\rangle$  transition. We want to look at how the absorption of the probe signal is modified in the presence of the control field as it propagates through the atomic medium. The macroscopic *response* of the atomic medium to this probe *stimulus*  $\vec{E}_p$

<sup>3</sup>The coefficients are  $\frac{1}{\sqrt{2}}$  only when the control-field is resonant, that is  $\delta_C = 0$ . More generic case is considered in references given in the text.

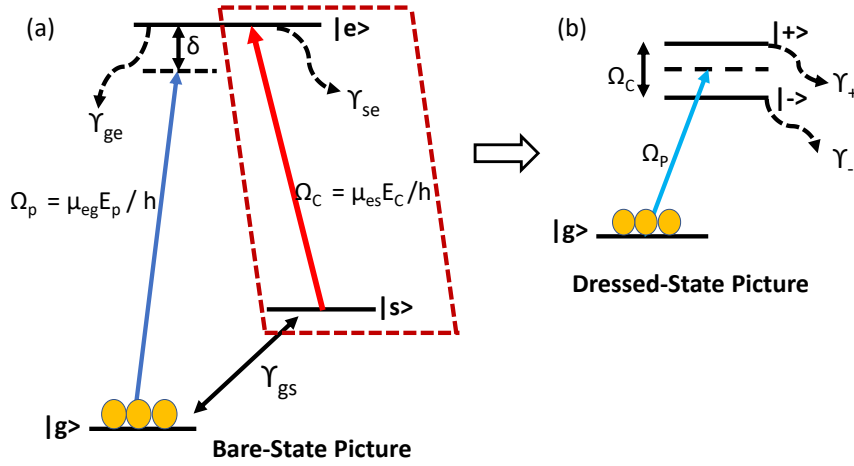


FIGURE 4.3: **(a)**: A three-level  $\Lambda$ -type atomic system with a weak probe (solid blue) and intense control (solid red) fields coupling the ground levels  $|g\rangle$  and  $|s\rangle$  to the excited level  $|e\rangle$ . The associated decay rates are indicated. **(b)**: Corresponding dressed-state picture. The strong control field creates a superposition of the bare atomic levels such that the new eigenstates occur at the probe-detuning and are separated by  $\Omega_C$ .

is given by the dielectric-polarization  $\vec{P}$ , and the mapping between this response polarization and stimulus field is given by the dielectric susceptibility  $\chi$  via:  $P(\vec{\delta}) = \epsilon_0 \chi(\delta) \vec{E}_p(\delta)$ , where the frequency dependence is due to frequency sweep of the probe signal. This linear relationship is valid at low probe intensities. The absorption-coefficient is then proportional to the imaginary part of this complex susceptibility, that is,  $A(\delta) \propto \text{Im}(\chi)$ . As an aside, we can also relate  $\vec{P}$  to the collective atomic coherence induced on the probe transition: this is because classically,  $\vec{P}$  is defined as the average dipole moment per unit volume. For a single atom, coupling between  $|g\rangle$  and  $|e\rangle$  via the probe field induces a dipole moment  $\mu_{eg} \equiv q \langle e | \hat{r} | g \rangle$ . If  $N$  is the number of such atomic dipoles per unit volume, the macroscopic polarization can be expressed as:  $\vec{P} = \sum_{i=1}^N \mu_{eg} \hat{\sigma}_{eg}(i) + h.c.$ . Here,  $\hat{\sigma}_{eg}$  is the projection operator defined as  $\hat{\sigma}_{eg} = |e\rangle \langle g|$  and  $h.c.$  stands for Hermitian conjugate. Infact, this is the basis for promoting polarization to a quantum-mechanical operator  $P \rightarrow \hat{P}$ , as done in §. 4.4.1.

The complex atomic polarization  $P(\delta)$  on the probe transition, as a function of probe detuning  $\delta$  is given as [67]:

$$P(\delta) = \frac{N \mu_{eg} \Omega_P (\delta - i \gamma_{gs})}{(\delta - i \gamma_{gs})(\delta - i \gamma_{ge}) - \Omega_C^2 / 4} \quad (4.2)$$

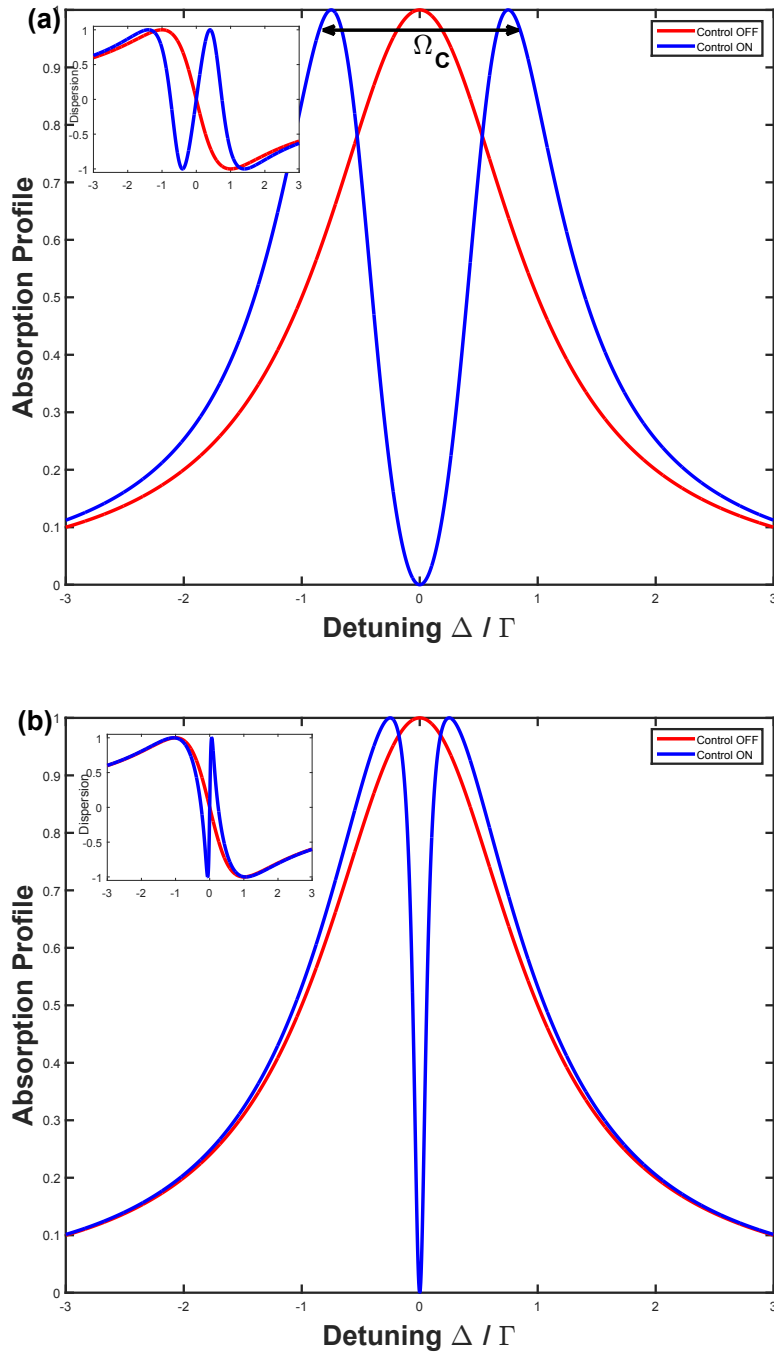


FIGURE 4.4: **(a)**: ATS: probe absorption as a function of detuning for control intensity  $\Omega_C = 1.5\Gamma_{ge}$ . The two Lorentzian peaks are separated by  $\Omega_C$ , and the sharp transparency is washed out. The inset shows the gradual variation in the refractive-index profile, and hence there is no slow-light effect involved. **(b)**: EIT: probe absorption as a function of detuning with (dotted blue) and without (dashed red) the control field when  $\Omega_C = 0.5\Gamma_{ge}$ . A narrow transparency window can be seen in the center. The inset shows the corresponding variation in the refractive-index of the medium. As can be seen, the slope of the refractive index is quite steep around the transparency window, which in turn decreases the group velocity of the probe.

Here  $N$  is the atomic density ;  $\gamma_{ge}$  is the polarization dephasing rate of the  $|g\rangle \leftrightarrow |e\rangle$  transition, which in the absence of other broadening mechanisms<sup>4</sup> is equal to half of the spontaneous decay rate ( $\Gamma_{ge}$ ).  $\gamma_{gs}$  refers to the non-radiative ground state spin decoherence rate: mechanisms such as stray magnetic fields, collisions, etc. can flip the spin states of the atoms. For the  $\Lambda$  type systems, in the absence of experimental instabilities,  $\gamma_{gs} \ll \gamma_{ge}$ . We have also assumed here that the control detuning is zero. Depending on the relative value of  $\Omega_C$  with respect to  $\gamma_{ge}$ , the complex polarization in Eqn. 4.2 can be written in different ways. For  $\Omega_C \gg \Gamma_{ge}$ , we have [68]:

$$P(\delta) \simeq \frac{N\mu_{eg}\Omega_P}{2} \left[ \frac{1}{\delta - \Omega_C/2 - i\gamma_{ge}} + \frac{1}{\delta + \Omega_C/2 - i\gamma_{ge}} \right] \quad (4.3)$$

The corresponding probe absorption-profile, given by  $Im(P) / \epsilon_0 E_P$  can be written as:

$$A(\delta) = \frac{N|\mu_{eg}|^2\gamma_{ge}}{2\hbar\epsilon_0} \left[ \frac{1}{(\delta - \Omega_C/2)^2 + \gamma_{ge}^2} + \frac{1}{(\delta + \Omega_C/2)^2 + \gamma_{ge}^2} \right] \quad (4.4)$$

Hence, for strong control fields, the probe absorption can be written as a sum of two well-separated Lorentzian profiles (Fig. 4.4 (a)), each having a width of  $\gamma_{ge}$  and centered at  $\pm\Omega_C/2$  with respect to the zero probe detuning. The frequency-separation between the two peaks is the control Rabi frequency  $\Omega_C$ . **This is the ‘Autler-Townes’ effect.** As the control field intensity is proportional to the Rabi frequency squared, it is also clear that the separation between the absorption peaks can be dynamically changed by varying the intensity of the control field, a feature that we have exploited in our memory scheme for broadband storage. Moreover, as seen from Eqn. 4.4, the absorption coefficient is a unitless quantity and we can measure it experimentally as  $A = \ln(I_0/I_T)$ , where  $I_0$  is the peak probe intensity and  $I_T$  is the transmitted intensity at a given detuning.

Similarly, in the weak control field limit, that is when  $\Omega_C \ll \Gamma_{ge}$ , the probe polarization and the absorption can be written as:

$$P(\delta) = N\mu_{eg}\Omega_P \left[ \frac{1}{\delta - i\gamma_{ge}} - \frac{(\Omega_C/\gamma_{ge})^2}{\delta - i(\gamma_{gs} + \Omega_C^2/\gamma_{ge})} \right] \quad (4.5)$$

$$A(\delta) = \frac{N|\mu_{eg}|^2}{\hbar\epsilon_0} \left[ \frac{\gamma_{ge}}{\delta^2 + \gamma_{ge}^2} - \frac{(\Omega_C/\gamma_{ge})^2(\gamma_{gs} + \Omega_C^2/\gamma_{ge})}{\delta^2 + (\gamma_{gs} + \Omega_C^2/\gamma_{ge})^2} \right] \quad (4.6)$$

<sup>4</sup>As for example, Doppler-broadening, power broadening etc.

As can be seen in Eqn. 4.6, the probe absorption in the weak control regime represents the difference between two Lorentzian profiles (Fig. 4.4 (b)), each centered at zero probe detuning (that is, the probe resonance frequency), with a broad and a narrow transition linewidth. **This is the EIT effect.** The narrow EIT linewidth is given by the second term in Eqn. 4.6.

So far, we have only considered one technical difference between the EIT and ATS processes, namely, the lineshape of the probe-absorption. As can be seen from the figures, both display a dip in absorption at the probe resonance (zero detuning), however, the dip in case of EIT, that is the transparency window, is sharp and narrow and is due to the destructive quantum interference between two transition pathways, whereas, in ATS, the AC-Stark effect widens this window and washes away the interference feature, thereby giving two broad resonances. Discerning whether an observed transparency feature is due to EIT or ATS (or hybrid) has been rather subjective [69]. Indeed, there are other subtle differences between them especially in the context of light storage and retrieval mechanisms, and we are currently working on a manuscript that systematically highlights these differences. In the next section, we introduce the light storage protocol using ATS.

## 4.4 The ATS Memory protocol

To understand the memory operation under the ATS regime, we consider the level scheme shown in Fig. 4.1 (a), however, as reported in [5], the storage can be implemented in other three level systems as well (eg: ladder-systems, optomechanical systems, superconducting circuits etc.) with some modifications. The ATS memory requires two optical fields: a weak and resonant probe (the signal field) to be stored, which couples the  $|g\rangle \leftrightarrow |e\rangle$  transition, and a strong, resonant control field, which couples the  $|s\rangle \leftrightarrow |e\rangle$  transition. The associated decay rates are also shown in the figure. Under the condition:  $\Omega_C > \gamma_{ge}$  and provided  $\gamma_{gs} \ll \gamma_{ge}$ , the probe transition exhibits an Autler-Townes splitting, where the frequency splitting between the absorption-peaks is  $\Omega_C$ . Note that in our experiments,  $\Omega_C(t) = \alpha \sqrt{P_C(t)}$ , where  $P_C(t)$  is the control field power and  $\alpha$  is the system specific proportionality constant. As detailed in §. 4.4.2, the bandwidth of our memory is determined solely by the peak value of  $\Omega_C(t)$  and hence, can be dynamically tuned by simply changing the control power.

### 4.4.1 Maxwell-Bloch Equations

The propagation of the signal field through the storage medium consisting of an ensemble of  $N$  atoms, in the presence of the control field is described using the Maxwell-Bloch equations (MBE) [70, 71]:

$$(\partial_t + c\partial_z)\hat{E}(z, t) = ig\sqrt{N}\hat{P}(z, t)n(z)\frac{L}{N} \quad (4.7)$$

$$\partial_t\hat{P}(z, t) = -\gamma_{ge}\hat{P}(z, t) + ig\sqrt{N}\hat{E}(z, t) + \frac{i}{2}\Omega_C(t)\hat{S}(z, t) \quad (4.8)$$

$$\partial_t\hat{S}(z, t) = -\gamma_{gs}\hat{S}(z, t) + \frac{i}{2}\Omega_C^*(t)\hat{P}(z, t) \quad (4.9)$$

In these equations, we restrict ourselves to the spatial variation only along the propagation direction of the optical fields, which is chosen along the  $z$  axis. The transverse dimensions are ignored. Here  $\hat{E}(z, t)$  is the electric-field operator for the signal field and represents the photonic mode of the system.  $\hat{P}(z, t)$  and  $\hat{S}(z, t)$  are the quantum mechanical operators describing the collective coherences associated with  $|g\rangle \leftrightarrow |e\rangle$  and  $|g\rangle \leftrightarrow |s\rangle$  transitions respectively [70]. Specifically,  $\hat{P}$  represents the ensemble operator for the macroscopic polarization generated by the signal via coupling to  $|g\rangle \rightarrow |e\rangle$  transition of all the atoms located within the optical beams. Similarly,  $\hat{S}$  is the ensemble operator for the collective spin excitation across all atoms interacting with the optical fields. The spin here refers to the two-photon coherence between the ground levels  $|g\rangle$  and  $|s\rangle$ , that is generated when the photonic state is transferred to the atomic state. The strength of the light-atom interactions is given by  $g\sqrt{N}$ . Here  $g \equiv \mu_{eg}\sqrt{\frac{\omega_0}{2\hbar\epsilon V}}$ , with  $\omega_0$  being the resonant frequency for  $|g\rangle \rightarrow |e\rangle$  transition and  $V$  is the interaction volume. Further, the peak optical depth  $d$  of the atomic ensemble is related to the atom-light coupling through  $d = 2g^2NL/\gamma_{ge}c$ . This parameter plays an important role in determining the efficiency of the memory operation. The atomic distribution along the length of the medium is given by the function  $n(z)$  and for a uniform distribution, the factor  $n(z)L/N$  is unity<sup>5</sup>. Moreover, we assume here that the control field is spatially uniform. This condition can be experimentally realized by choosing the size of the control field to be larger than the diameter of the atomic cloud. A uniform Rabi intensity eliminates additional ATS line broadening as detailed in the methods of [5]. Further, we assume both the control and signal fields have a slowly varying temporal envelope, so that we can write  $\partial_t\hat{E}(z, t) = 0$ . The polarization dephasing rate in

<sup>5</sup>These equations were simulated for different atomic distribution functions and the dynamics were found to be independent of the distribution.

Eqn. 4.8 is given by half of the spontaneous decay  $\Gamma_{ge}$ . It must be however, mentioned that in general, this dephasing is a complex quantity given by  $(\gamma_{ge} + \gamma_D) + i\delta$ ; here  $\delta$  is the detuning of the signal field with respect to the  $|g\rangle \rightarrow |e\rangle$  transition,  $\gamma_{ge} = \Gamma_{ge}/2$  and  $\gamma_D$  includes broadening due to other factors such as Doppler and / or power-broadening.

We next discuss the relevance of these equations in the context of light storage and recall. The storage and retrieval processes are the result of the time-reversal symmetry embedded in the structure of the MBE. The excitation of the polarization component  $\hat{P}$  is caused by the photonic mode  $\hat{E}$ . This polarization couples to the control field  $\Omega_C$  which then maps it into the spin wave coherence  $\hat{S}$ . Thus, the couplings  $\partial_t \hat{P} \sim \Omega_C \hat{S}$  and  $\partial_t \hat{S} \sim \Omega_C^* \hat{P}$  correspond to the signal storage / write stage whereby the optical coherence is mapped to the collective spin wave. We can thus interpret the  $\hat{S}$  operator as an annihilation operator, in that a photonic mode is annihilated to create a spin excitation [72]. During the retrieval process, which is the time reversed storage process, the control field couples to the stored ground spin wave and maps it into the polarization component involving the excited state. This then leads to the re-emission of the photonic mode into the signal channel.

To conclude this section, we note that although, there are different quantum memory protocols following different approaches to storage, all of them are governed by the same fundamental Maxwell-Bloch equations of (4.7),(4.8) and (4.9). The four important parameters in these equations include the control Rabi frequency  $\Omega_C$ , signal detuning  $\delta$ , polarization decay rate  $\sim \gamma_{ge}$  and the optical depth  $d$ . It turns out that varying one or more of these parameters can lead to completely different physical processes. These parameters define the operational regime where a particular quantum memory can function. Therefore, there are various metrics / performance specifications assigned to any quantum memory protocol such as storage time, memory bandwidth, efficiency and fidelity, each of which is affected by the above parameters. As stated earlier, we are working on a detailed comparison among the established memory schemes and the ATS protocol.

#### 4.4.2 ATS Memory Operation

In this section, we study the memory operation under different timing configurations of the control field, namely, the *constant field*; the *interrupted field* and the *pulsed field*. The pulsed control corresponds to the case of dynamically changing positions of the probe-absorption peaks in the frequency space.

In each of these configurations, we are mapping the coherence of the input signal (photonic) mode  $E_{\text{in}}(z, t) = \hat{E}(0, t)$  (that has a slowly varying temporal profile over a time interval  $[0, \tau]$ ) to a spin-wave excitation  $\hat{S}(z, t > \tau)$  and after a certain storage time  $T$ , map it back into the photonic mode  $\hat{E}(L, t > T)$ , which is the retrieved signal. The storage time  $T$  can be fixed (constant control) or chosen at will (interrupt and pulsed control). Thus, interrupt and pulsed fields provide on-demand storage and recall operations.

We first consider the case when the control intensity is *constant*, that is, the applied control field generates a fixed ‘Autler-Townes Splitting (ATS)’ for all times. A short gaussian signal pulse  $\hat{E}(0, t)$  enters the medium at  $t = 0$ , whose spectral profile covers the ATS-peaks. **For our ATS protocol, the bandwidth of the signal pulse  $B_{\text{FWHM}}$  is chosen to match the ATS splitting, which is also the Rabi frequency of the control field  $\Omega_C$ .** This means the following relation must always be held with regards to ATS memory scheme:  $\Omega_C/2\pi = B_{\text{FWHM}} \cong 0.44/\tau_{\text{FWHM}}$ , where  $\tau_{\text{FWHM}}$  is the signal duration at the full-width half maxima, and is related to the total pulse duration  $\tau$  as  $\tau = 2.25\tau_{\text{FWHM}}$ . As the ATS effect is dominant only when  $\Omega_C \gg \Gamma$ , the spectral matching condition makes the **ATS memory inherently broadband**, that is, ideally suited for storing short (in temporal domain) pulses. As the signal pulse propagates through the medium, it is partially or completely absorbed and mapped into the spin mode over the duration  $\tau$ . Immediately after this mapping is complete, the pulse is coherently recovered and re-emitted between  $\tau < t < 2\tau$ . A partial storage results in some part of the input signal being transmitted through the medium. An important factor governing the storage and recall processes is the pulse area of the control field during each of the storage and recall stages:

$$A_C(t) = \int_0^\tau \Omega_C(t) dt \quad (4.10)$$

where  $\tau$  defines the timescale for the occurrence of these processes. As  $\Omega_C$  is constant for this configuration, we can compute  $A_C(t)$  to be:

$$\begin{aligned} A_C(t) &= \Omega_C \tau & (4.11) \\ &= (2\pi B_{\text{FWHM}}) \times 2.25\tau_{\text{FWHM}} \\ &= 2\pi(0.44/\tau_{\text{FWHM}})(2.25\tau_{\text{FWHM}}) \\ &= 2\pi \end{aligned}$$

The dynamics of the ensemble-light system is contained in the time-evolution

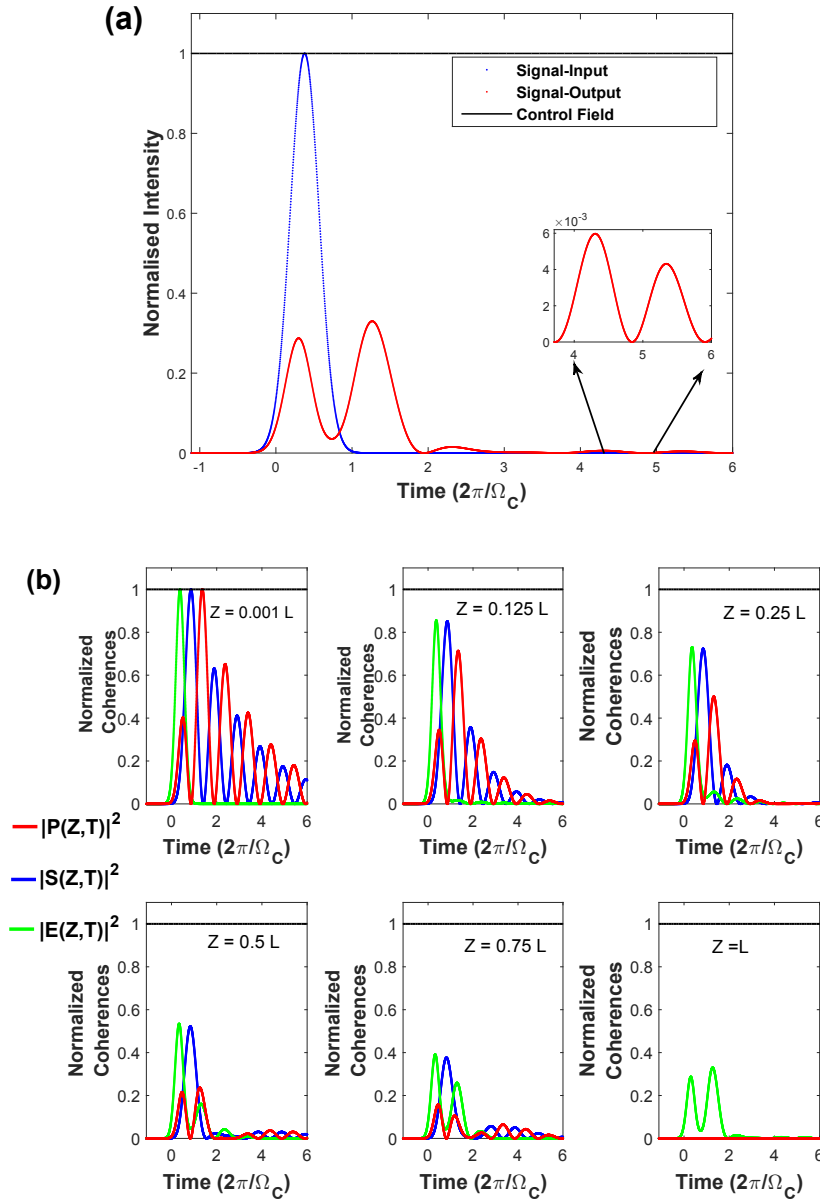


FIGURE 4.5: **(a)**: A control field that is on at all times (dashed black) generates a fixed separation between the probe absorption peaks, given by  $\Omega_C$ . In these simulations, the probe signal (dotted blue) has a bandwidth  $B_{\text{FWHM}} = \Omega_C/2\pi = 11$  MHz. This corresponds to the Rabi period  $2\pi/\Omega_C = 90$  ns. Other parameters are:  $\Omega_C = 7\Gamma$ ,  $d = 13$ ,  $\gamma_{gs} = 0$ . Due to partial storage, some amount of the signal is simply transmitted (the part of output that is overlapping in time, with the probe signal). The signal that gets absorbed is re-emitted multiple times at fixed delays of  $2\pi/\Omega_C$  (inset). The retrieval efficiency of first order echo was  $\sim 36\%$ . **(b)**: Time evolution of  $|S(z,t)|^2$  (blue),  $|P(z,t)|^2$  (red) and  $|E(z,t)|^2$  (green) modes (normalized) at different spatial positions inside the medium. They exhibit an oscillatory behavior with a period equal to  $2\pi/\Omega_C$ . Complete transfer from photonic to spin mode and vice versa occurs when the control pulse area equals  $2\pi$ . The spatial locations are indicated in each case in terms of medium length  $L$ . **Also note that the spin and photonic modes are 180 degrees out of phase with each other**, which is in stark contrast to an EIT based memory.

of the spin  $|S(z, t)|^2$ , polarization  $|P(z, t)|^2$  and photonic  $|E(z, t)|^2$  coherences, that also describe the storage and recall processes. The storage and recovery relies on the oscillatory exchange of coherence between the spin and photonic modes with oscillations occurring at the Rabi period :  $2\pi/\Omega_C$ , as shown in Fig. 4.5. Similar observations were also made in [73], where the authors proposed a photon-echo based GEM storage via ATS absorption. Moreover, the reversible exchange between the two modes is mediated by the dipole-polarization coupling. Specifically, the initial coherence of the signal reversibly evolves into the spin and photonic modes inside the medium and gets mapped into the delayed output-photonic mode  $\hat{E}(L, t > T)$  for those times when the control pulse area  $A_C(t) = 2n\pi$ , where  $n$  is an integer. As an example, in the first cycle ( $n = 1$ ), the coherence in  $\hat{E}(0, t)$  is transferred to the spin excitation  $\hat{S}(z, t > \tau)$  inside the medium (absorption / storage) and in the second cycle ( $n = 2$ ), the stored excitation is converted back into the photonic mode at the output (re-emission / retrieval). The time interval (delay) between the two processes is  $2\pi/\Omega_C$ . Also, as shown in figure 4.5, some coherence remains as spin inside the medium after the first recall, and hence, is retrieved as smaller intensities at the output, with delays of Rabi period. The signals retrieved after the first recall are referred to as ‘multiple-orders’.

Next we consider the interrupted timing configuration where the control field, that was initially ‘ON’, is switched off just before the onset of first recall. We refer to this stage as the ‘writing-stage’, where the optical coherence is transferred to the spin mode during the  $2\pi$  pulse area of the ‘write-control’ field ( $A_C^W$ ). Immediately, after this mapping is complete, the control field is turned off and the spin wave remains preserved inside the medium (provided there is no decoherence). After a certain storage time  $T$ , the control field can be turned back on, which transfers the spin coherence between the two ground levels, back into the output photonic mode, when the pulse area of the read-out control field ( $A_C^R$ ) reaches  $2\pi$ . This configuration therefore, converts the fixed delay operation into an on-demand retrieval process (Fig. 4.6).

In the third timing configuration (figure.4.7), we show the ATS memory operation in the pulsed mode, that is, when we have a time varying control power, both during the writing and reading stages. Since  $\Omega_C(t)$  is proportional to the square root of control power, we get a dynamic ATS. It is important to mention, that the dynamics of storage and readout processes depend only on the pulse areas of the respective control fields ( $A_C^W, A_C^R$ ) and not the specific time-dependence of  $\Omega_C(t)$ . Hence, the mapping of coherence

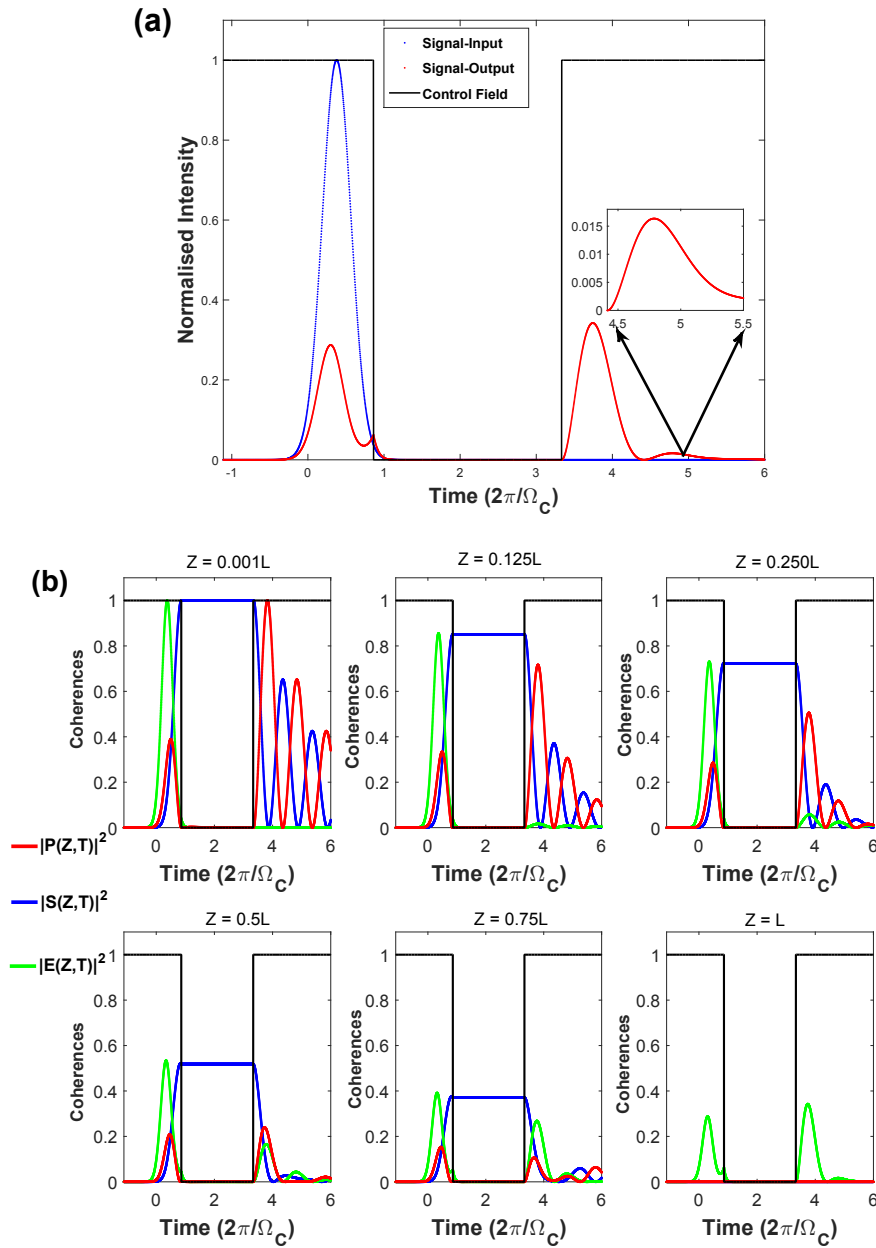


FIGURE 4.6: **(a)**: Storage and retrieval can be achieved on demand by using a control field that is turned off just before the first recovery (write-operation) and then turned on again after the desired storage time (read-out operation). Similar parameters as stated in Fig. 4.5 were used for simulation. The first-order efficiency, as before, is 36 %. **(b)**: Temporal evolution of spin, photonic and polarization coherences (all normalized), at different positions inside the medium. During the write stage, the polarization mode mediates the transfer from the signal photonic mode to the atomic spin mode. This spin remains preserved inside the medium when the control field is turned off (zero decoherence assumed here). Turning the control field back on resumes the transfer from the spin to the output photonic mode, again mediated by the polarization component.

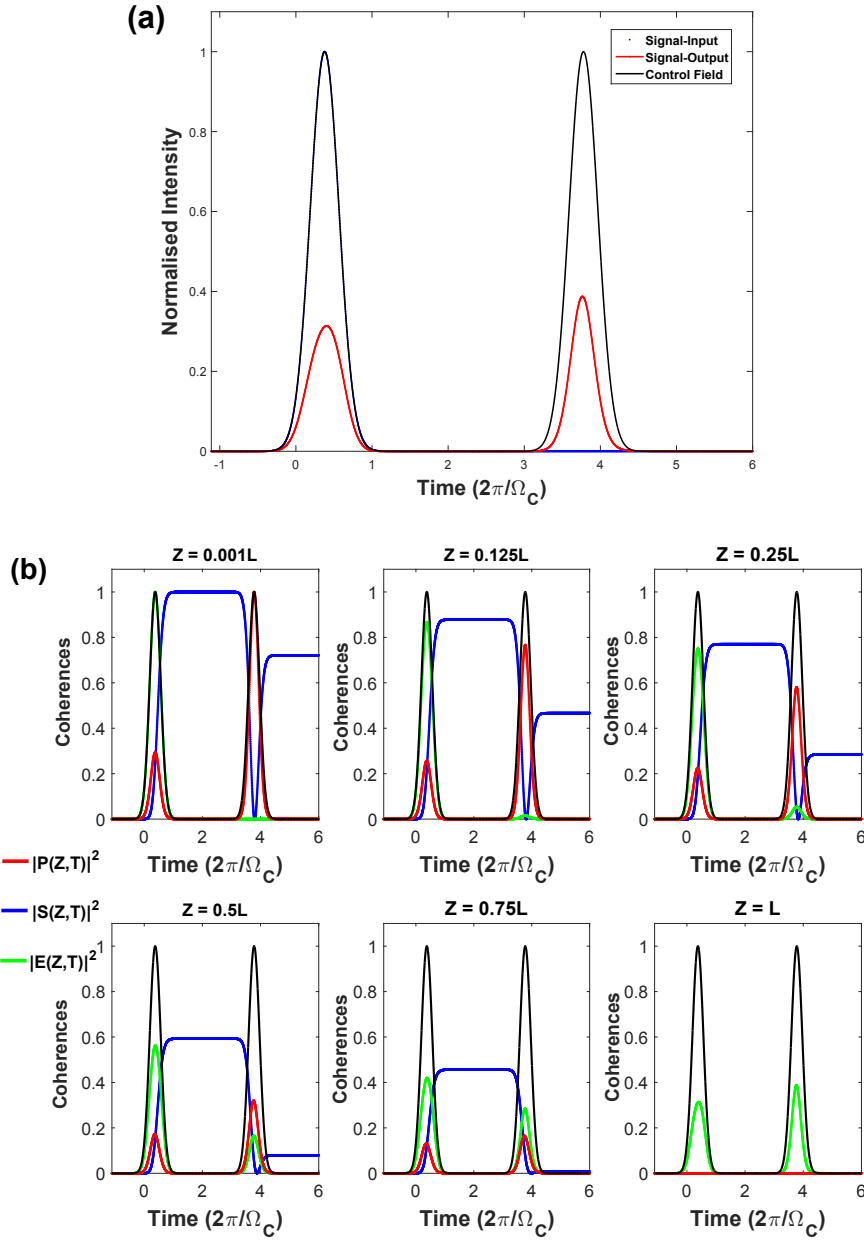


FIGURE 4.7: **(a)**: The memory operation achieved by using pulsed control fields at the writing and reading stages. Both the probe and control fields are gaussian and have the same temporal profile. Like the constant and interrupted timing configurations, the write and read dynamics only depend on the  $2\pi$  pulse areas of the write and read control fields. For the gaussian control fields, the peak Rabi frequency  $\Omega_{C,\text{Gaussian}}^{\text{peak}} = 1.5 \times \Omega_{C,\text{Constant}}$ , to ensure the  $2\pi$  pulse area. This means for the simulation parameters stated earlier,  $\Omega_{C,\text{Gaussian}}^{\text{peak}} = 10.5 \Gamma$ . **(b)**: Time evolution of various coherences at different positions inside the medium. Also note that due to the pulsed nature of the control field, we do not get multiple orders of the photonic mode at the output.

from the photonic (spin) mode to spin (photonic) mode takes place whenever  $A_C^W$  ( $A_C^R$ ) equals  $2\pi$ . Note that for the pulsed case,  $A_C^W = \int_0^\tau \Omega_C^W(t)dt$  and  $A_C^R = \int_0^\tau \Omega_C^R(t)dt$ . Hence, we implement the pulsed operation by using the control fields of same temporal profile as the input signal. In [5], we have used the pulsed-ATS scheme to manipulate light pulses such as pulse shaping (temporal stretching or compression) and temporal beam-splitting to demonstrate the preservation of coherence in the storage and recall processes.

### 4.4.3 ATS memory efficiency

The total efficiency of the ATS memory operation can be defined as:

$$\eta = \frac{\int_T^\infty |E(L, t)|^2 dt}{\int_0^\tau |E(0, t)|^2 dt} \quad (4.12)$$

which is the ratio of the energy carried by the retrieved pulse  $E(L, t > T)$  (the output photonic mode) to the energy carried by the input signal  $E(0, t < \tau)$  (the input photonic mode). As before,  $(T; \tau)$  are the memory storage time and the signal pulse duration respectively. Based on the ATS memory operation described in §. 4.4.2, we can write the total efficiency as a product of three factors:

$$\eta = \eta_s \eta_r \eta_d \quad (4.13)$$

Here,  $\eta_s$  is the ratio of the stored excitations in the spin-wave mode to the mean number of photons in the input signal mode, and is called the storage efficiency. Thus,  $\eta_s$  is determined during the storage / writing stage. Similarly,  $\eta_r$  is the ratio of the mean number of photons in the outgoing (output) mode to the stored spin excitations, and is called the retrieval efficiency, and determined during the read-out stage. The spin-wave survival efficiency during the storage time  $T$  is represented by  $\eta_d$  and incorporates the effects due to decoherence, that arises in practical settings. As can be seen from Eqn. 4.13, the effect of decoherence is to reduce the overall memory efficiency and hence precise experimental control is required to avoid the loss of coherence from the system. In the ideal case of no or negligible decoherence,  $\eta_d$  approaches unity.

We now analyze the storage and retrieval efficiencies: as stated earlier, the reversible exchange of coherence between the spin and photonic modes is mediated by the collective excitation on the  $|g\rangle \rightarrow |e\rangle$  transition, which describes the polarization mode. In the writing stage, the input photonic mode

first excites this polarization mode (that is, the probe signal gets absorbed by the medium), which is then simultaneously mapped, onto the collective spin coherence, by the control field. The storage efficiency, thus, depends on two factors: the collective absorption ( $\mu_{\text{abs}}$ ) which is the coherent sum of absorption probabilities of the input signal by all the atoms in the ensemble, and is a function of  $d$ ,  $\Omega_C^W$  and  $\Gamma$ . The parameters  $\Omega_C^W$  and  $\Gamma$  appear due to the fact that the two ATS absorption lines are generated by the ‘strong’ control field ( $\Omega_C > \Gamma$ ), and are spectrally separated by  $\Omega_C$ , with the linewidth of each peak as  $\Gamma/2$ . The second factor ( $\mu_w$ ) relates to the efficiency of the polarization mediated reversible exchange between the photonic and spin modes, and is determined by the pulse area of the write-control field ( $A_C^W$ ). A close-to-unity value of  $\mu_w$  at the end of writing stage, would imply a complete transfer from the polarization to the spin mode.

The time-reversal symmetry of the Maxwell-Bloch equations suggests similar treatment for the read-out efficiency. The read control field maps the atomic spin coherence to the atomic polarization coherence which then simultaneously emits photons into the output photonic mode. The retrieval efficiency thus, depends upon the collective re-emission probability ( $\mu_{\text{re}}$ ) and the efficiency of the polarization mediated transfer between the stored spin and the output photonic mode ( $\mu_r$ ).  $\mu_{\text{re}}$  is the coherent sum of emission probabilities of the output photonic mode by all atoms in the ensemble, and is a function of  $d$ ,  $\Omega_C^R$  and  $\Gamma$ . In analogy with  $\mu_w$ ,  $\mu_r$  is determined by the pulse area of the read-control field  $A_C^R$ .

Based on the above discussion and assuming negligible decoherence ( $\eta_d \sim 1$ ), we can expand  $\eta_s$  and  $\eta_r$  to write the total memory efficiency as (also see Fig. 4.8):

$$\eta = \mu_{\text{abs}}(d, \Gamma, \Omega_C^W) \times \mu_w(A_C^W) \times \mu_{\text{re}}(d, \Gamma, \Omega_C^R) \times \mu_r(A_C^R) \quad (4.14)$$

For the complete mapping of atomic polarization component to either of the spin or photonic mode, the control pulse area should be equal to  $2\pi$ , that is  $A_C^W = 2\pi = A_C^R$  (see figures 4.5, 4.6 and 4.7). In that case,  $\mu_w = \mu_r = 1$ . Thus, the overall efficiency simplifies to:

$$\eta = \mu_{\text{abs}}\mu_{\text{re}} \quad (4.15)$$

and is solely determined by the collective absorption and re-emission processes. In fact, this expression puts the ATS memory into the league of absorption-based quantum memories such as the CRIB and AFC. Hence, we can use

similar analytic expressions that describe the memory efficiency of these protocols [62]:

$$\eta_F = \tilde{d}^2 \exp(-\tilde{d}) \mu_d \quad (4.16)$$

$$\eta_B = \left(1 - \exp(-\tilde{d})\right)^2 \mu_d \quad (4.17)$$

Here,  $\eta_F$  and  $\eta_B$  are the overall memory efficiencies for the cases when the control and the probe fields are co-propagating ('forward propagation') and counter-propagating ('backward propagation') respectively.  $\tilde{d}$  is the effective optical depth (explained below);  $\mu_d$  is the survival probability of the collective polarization from dephasing during the writing and reading stages. Here the forward retrieval implies that the output photonic mode is emitted in the 'propagation direction' of the input signal, that is, if the input mode entered the atomic media at  $z = 0$ , the output photonic mode is retrieved at  $z = L$ . For the backward propagation, collective re-emission occurs at the input side of the medium, that is, the output mode is retrieved at  $z = 0$ .

A physical definition of  $\tilde{d}$  is as follows: if a resonant probe beam with peak intensity  $I_0$  passes through an atomic medium of length  $L$ , we can write the intensity of the transmitted beam using 'Beer-Lambert' law as:  $I_T = I_0 \exp(-\alpha L)$ , where  $\alpha$  denotes the absorption coefficient of the medium. The peak optical density  $d$  of the medium is then defined as  $d \equiv \alpha L = \log_e(I_0/I_T)$ , and corresponds to the distribution of atoms being concentrated around the absorption frequency of the center line. Assuming a Lorentzian lineshape and no inhomogeneous broadening, the linewidth of absorption frequency is given by its spontaneous decay rate  $\Gamma$ . In the ATS memory scheme, we split this absorption line into two peaks: the linewidth of each peak is  $\Gamma/2$  and the separation between them is  $\Omega_C$ . Thus, the 'effective' optical density of the medium is reduced by a factor that is given by the ratio of separation between the two peaks and the width of each peak. Thus,  $\tilde{d} = \frac{d}{(2\Omega_C/\Gamma)}$ . We define another phenomenological parameter  $F$  or the 'ATS-factor' as  $\Omega_C/\Gamma$ , such that  $\tilde{d} = d/2F$ . The ATS-factor defined here is analogous to the 'finesse parameter' of a spectral atomic frequency comb [62]. The role of  $(\tilde{d}, F)$  in the efficient storage and retrieval processes is discussed below.

Optimal storage and recall requires the ATS absorption lines to span the probe signal bandwidth  $B_{\text{FWHM}}$ . As the ATS peaks are separated by control Rabi frequency, we fulfill the above condition by ensuring that  $B_{\text{FWHM}} = \Omega_C/2\pi$ . This spectral matching effectively relates the ATS factor to be proportional to the signal bandwidth to be stored:  $F = B_{\text{FWHM}}(\text{MHz}) / \Gamma(\text{MHz})$ .

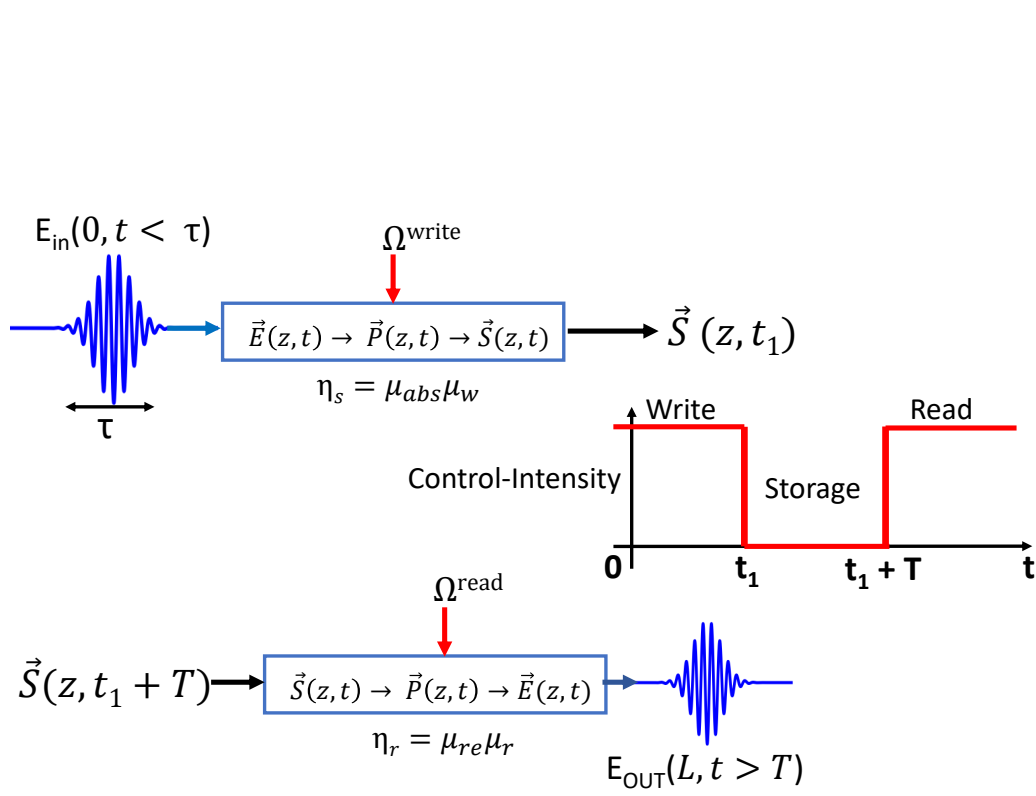


FIGURE 4.8: A simple block-diagram showing the storage and retrieval efficiencies in the ATS memory. The overall efficiency is the product of the two and is given in 4.14. Zero decoherence is assumed here. Specifically, storage occurs when an incoming signal mode  $\hat{E}_{\text{in}}(t)$  with a pulse-duration of  $\tau$  is mapped to a spin-wave mode  $\hat{S}$ , at some time  $t > \tau$ . The efficiency of this transfer is determined by  $\mu_{\text{abs}}\mu_{\text{w}}$ . The retrieval process is the time-reversed storage process where a stored spin mode is mapped back onto the photonic mode  $\hat{E}_{\text{out}}(t)$ , at some time  $t > T$ , where  $T$  defines the time interval over which the incoming signal was stored as a spin-wave-mode. This transfer efficiency is determined by  $\mu_{\text{re}}\mu_{\text{r}}$ .

We also reiterate that this spectral matching condition is equivalent to saying that the control pulse area equals  $2\pi$ , as was also shown in §. 4.4.2. Now, as the absorption and re-emission occur through the ATS lines,  $\tilde{d}$  is an increasing function of optical depth ( $d$ ) and the linewidth of the ATS peaks ( $\Gamma/2$ ) while a decreasing function of separation between the peaks ( $\Omega_C$ ). Next, the factor  $\mu_d$  in equations. 4.16-4.17 account for the dephasing of the polarization due to the finite width of the ATS lines and is determined by the inverse-Fourier transform of an ATS line over the complete duration of the input signal. The effect of dephasing is to reduce the amplitude of the re-emitted output signal. As the ATS lines are Lorentzian, their inverse Fourier transform gives  $\mu_d = \exp(-\Gamma\tau)$ , where  $\tau$  is the total duration of the probe pulse. For the gaussian probe,  $\tau = 2.25t_{\text{FWHM}} = 2.25 * 0.44/B_{\text{FWHM}} = 1/B_{\text{FWHM}}$ . By substituting  $\tau$  and applying the  $2\pi$  pulse area condition, we get  $\mu_d = \exp(-1/F)$ . Here, we see that the effect of dephasing decreases as we go towards storing larger bandwidth signals (increasing  $F$ ). This again shows that our memory operation favors the broadband regime. Finally, we can now write the analytic efficiency expressions as:

$$\eta_F = (d/2F)^2 \exp(-d/2F) \exp(-1/F) \quad (4.18)$$

$$\eta_B = \left(1 - \exp(-d/2F)\right)^2 \exp(-1/F) \quad (4.19)$$

The analytically calculated efficiency values are in good agreement with those obtained through the numerical solution of the Maxwell-Bloch equations, as shown in Figures. 4.9 and 4.11, where the efficiency is plotted for a range of  $d$  and  $F$  values. The inset of each figure shows the numerical efficiency as a function of the effective optical depth and provides useful insight into the above equations. Let us qualitatively look at the terms appearing in Eqn. 4.18 for the forward propagating output mode: the first term is the square of the effective optical depth and represents the collective absorption and re-emission probability. A high value of  $\tilde{d}$  means a greater number of atoms participate in the storage and retrieval processes, thereby providing higher overall efficiency. The second term is a decaying exponential and represents the loss of emitted signal due to re-absorption by atoms, during the memory readout. The re-absorbed light remain in the medium as stored spin excitation, and can be re-emitted as higher order echoes (Figures. 4.5 and 4.6). Finally, the third term is the polarization de-phasing factor.

Now, as shown in Fig. 4.9, for a given  $F > 1$  (equivalently  $\Omega_C > \Gamma$ ), the

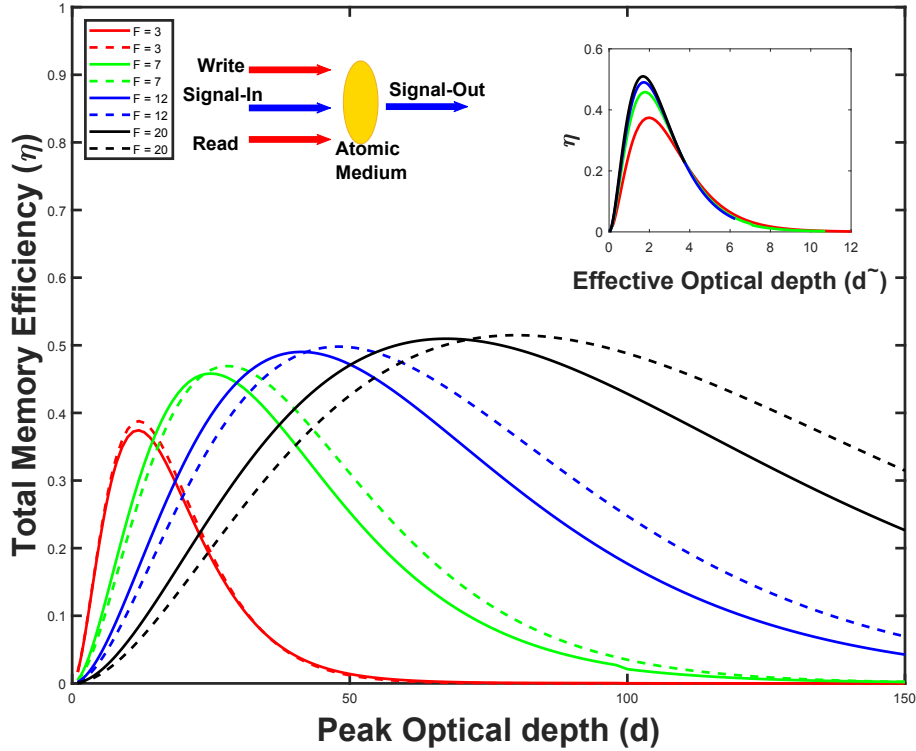


FIGURE 4.9: Theoretical efficiency as a function of peak-optical-depth for the ATS based storage and retrieval when the signal-control fields are co-propagating (forward-retrieval). Solid curves correspond to values obtained numerically while the dashed curves correspond to the analytic expression in Eqn. 4.18, showing they are in good agreement with each other. In each case, the curves correspond to different  $F = \Omega_C/\Gamma$  values. The calculations are done for pulsed ATS memory with  $A_C^W = A_C^R = 2\pi$ . The maximum efficiency in the forward mode is limited to 54%. **Inset** Efficiency as a function of effective optical depth  $\tilde{d} = d/2F$  for different  $F$  values. Maximum efficiency for a given  $F$  is achieved when  $\tilde{d} \simeq 1.75$  and decreases thereafter.

memory efficiency increases until  $\tilde{d} \simeq 1.75$  (**the optimal effective OD**). In this regime, the first term of Eqn. 4.18 dominates. As the optical depth is further increased, the re-absorption (loss) term dominates the first term. Consequently, the maximum efficiency in the forward retrieval is limited to 54 %, which is achieved when  $\tilde{d}$  is optimal at 1.75 and  $F$  is large (larger signal bandwidth). The re-absorption term is eliminated in the backward propagation (Eqn. 4.17 and 4.19). Here, the efficiency is an increasing function of  $\tilde{d}$  and for a given finesse, tends to saturate at  $\tilde{d} \simeq 3$ . Further, the efficiency is a strong function of the ATS factor, in that, the  $F$  is embedded in all the terms of equations 4.18 and 4.19. As  $F$  directly determines the polarization dephasing, for a given  $\tilde{d}$ , the efficiency increases as  $F$  increases (increase in  $F$  is equivalent to saying that the absorption linewidth effectively decreases; this reduces the polarization decay rate). Near-unity efficiency is thus possible in the backward configuration for  $\tilde{d} \geq 3$  and  $F \gg 1$ . Also shown are the spatial and temporal evolution of spin ( $|S(z, t)|^2$ ) and photonic ( $|P(z, t)|^2$ ) coherences in figures.4.10 and 4.12, during the storage and readout processes. These are calculated for the signal and control fields co-propagating (forward mode) and counter-propagating (backward mode) respectively. The parameters chosen for calculation correspond to  $\eta = 0.5$  (forward mode) and 0.9 (backward mode).

To conclude the discussion, we note that the maximum efficiency for a given bandwidth (or  $F$ ) is achieved when  $\tilde{d}$  is optimal. This optimal value, as seen from the efficiency plots, is 1.75 and 3 respectively for the forward and backward configurations. In this optimal regime, the pulse area for both the write and read control pulse is  $2\pi$ , which makes the polarization mediated reversible transfer between the spin and photonic modes as unity. In other words, the factors  $\mu_W, \mu_R$  are unity, and the expression in Eqn. 4.14 gets simplified. It must be recalled that  $A_C = 2\pi$  implies that  $\Omega_C/2\pi = B_{FWHM}$ . However, upto a certain extent, the requirement of  $2\pi$  control pulses can be relaxed for the non-optimal  $\tilde{d}$ . This can be seen from the definitions of  $\tilde{d}$  and  $F$  in terms of the control Rabi frequency:  $F = \Omega_C/\Gamma$  and  $\tilde{d} = (\Gamma d)/\Omega_C$ . Consider the forward retrieval case: if, for a given  $(d; B_{FWHM})$ ,  $\tilde{d} < 1.75$ , we can effectively increase it by choosing  $\Omega_C/2\pi < B_{FWHM}$  which in turn means  $A_C < 2\pi$ . While the reduced pulse area increases the absorption and re-emission probabilities ( $\mu_{abs}\mu_{re}$ ), it reduces  $\mu_W\mu_R$ , and thus, there is a trade-off as to how much we can deviate from optimum  $2\pi$  condition. In the low- effective-optical-depth regime, we observed optimal efficiencies for

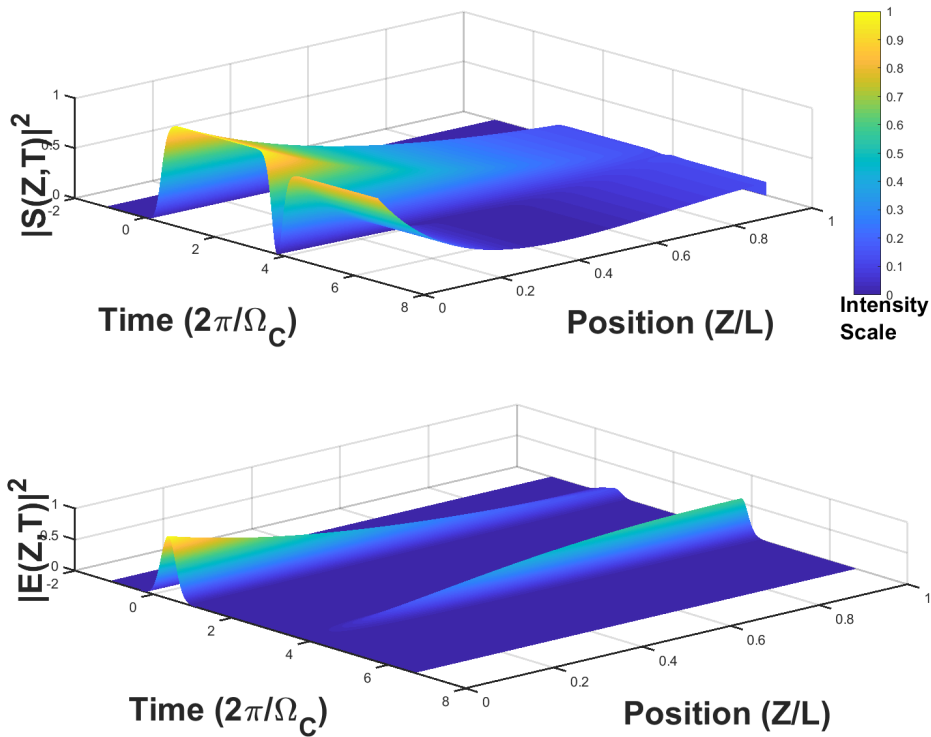


FIGURE 4.10: Calculated temporal dynamics of spin (**top**) and photonic (**bottom**) modes at all positions inside the medium, for the forward retrieval. The calculations are done for the  $2\pi$  write and read control pulses. As stated in the text, a  $2\pi$  control pulse provides complete transfer from the polarization mode to either of the spin (storage) or photonic (retrieval) modes. The simulation parameters are:  $d = 40$ ,  $F = 12$  and  $\eta = 0.5$ . Due to re-absorption of the emitted photons, a significant portion of energy remains stored as spin wave inside the medium, during the readout stage.

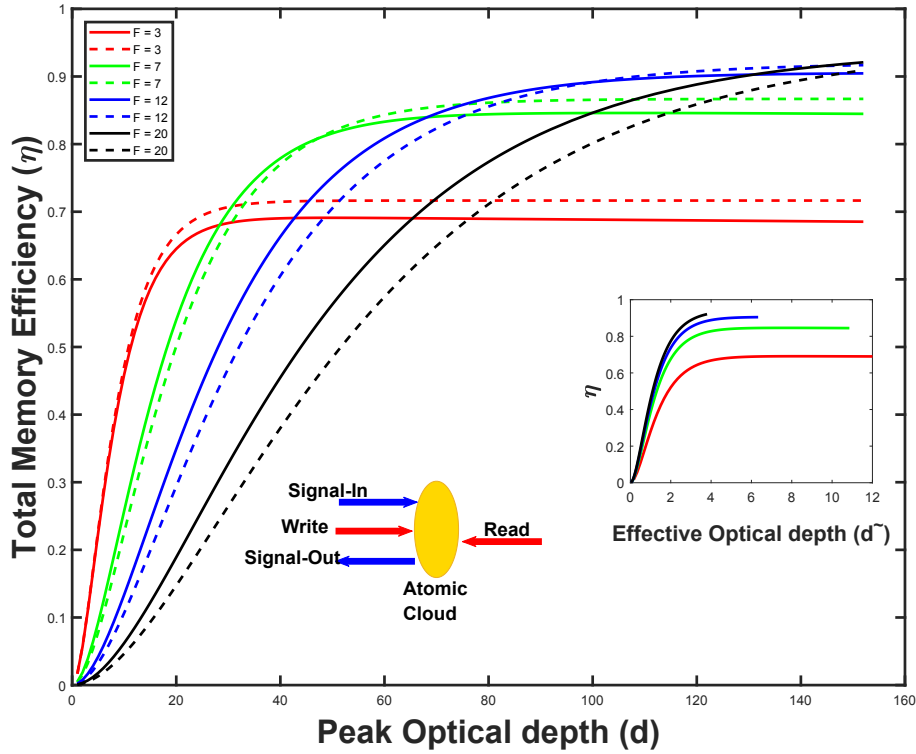


FIGURE 4.11: Theoretical efficiency as a function of peak-optical-depth for the ATS based storage and retrieval when the read-control field is counter-propagating to the signal field (backward-retrieval). Solid curves correspond to values obtained numerically while the dashed curves correspond to the analytic expression in Eqn. 4.19, showing they are in good agreement with each other. In each case, the curves correspond to different  $F = \Omega_C/\Gamma$  values. Near unity efficiency is achieved at finesse values  $\gg 1$ . The calculations are done for pulsed ATS memory with  $A_C^W = A_C^R = 2\pi$ . **Inset** Efficiency as a function of effective optical depth  $\tilde{d} = d/2F$  for different  $F$  values. For a given  $F$ , the efficiency saturates at  $\tilde{d} = 3$ .

pulse areas upto  $1.6\pi$ . Similarly, when we are in the high-effective-optical-depth regime ( $\tilde{d} > 1.75$ ), we can lower  $\tilde{d}$  by choosing higher control power such that  $A_C > 2\pi$ . We observed good efficiency upto  $2.2\pi$ . Again, we cannot increase the control power indefinitely due to the compromise between increasing  $\mu_{\text{abs}}\mu_{\text{re}}$  and decreasing  $\mu_W\mu_R$ .

**To summarize:** the total efficiency of the storage and recall processes can approach close to unity, as shown in Fig. 4.11. It is clearly seen that in both the forward and backward modes of retrieval, the efficiency increases as we move towards higher finesse ( $F$ ) values. As the finesse parameter is linked to the signal bandwidth, our ATS memory is inherently suitable for broadband storage. Of course, storing a higher bandwidth would require higher

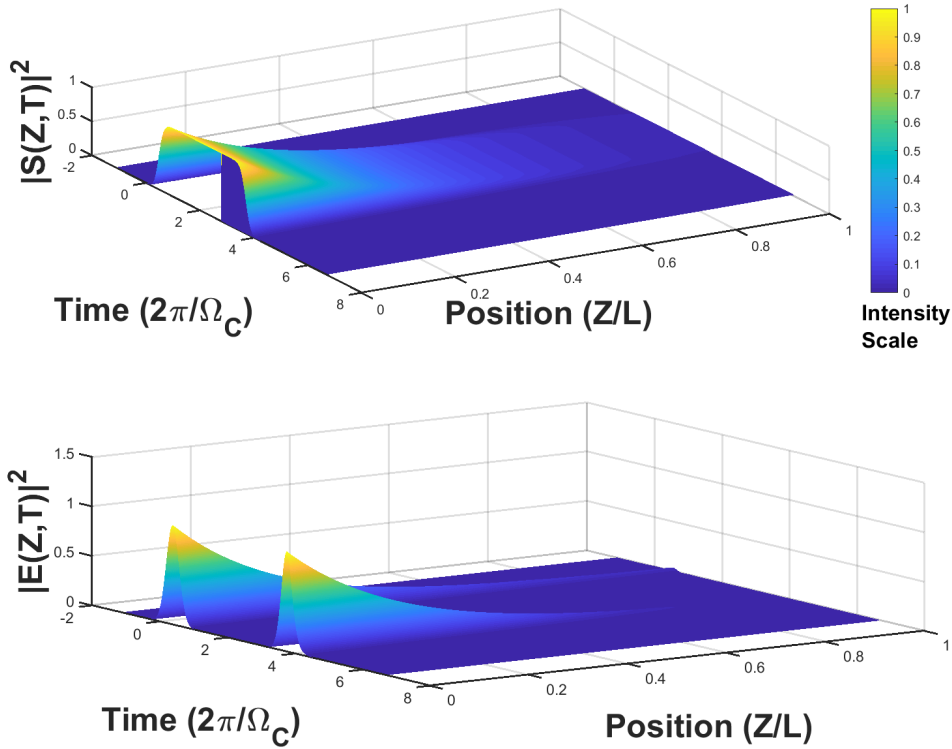


FIGURE 4.12: Calculated temporal dynamics of spin (**top**) and photonic (**bottom**) modes at all positions inside the medium, for the backward retrieval. The calculations are done for the  $2\pi$  write and read control pulses. The simulation parameters are:  $d = 85$ ,  $F = 12$  and  $\eta = 0.9$ . As can be seen, no spin excitation remains in the medium after the recall process, since there is no re-absorption.

control power, so as to get the  $2\pi$  pulse area. Further, as seen in the efficiency curves, maximum efficiency, for a given  $F$ , occurs at the optimal effective optical depth. This implies higher bandwidth storage also requires higher optical depth. In fact, to achieve the same overall efficiency at different signal bandwidths, the ATS memory bandwidth scales *linearly* with respect to the optical depth and *quadratically* with the control power ( $\Omega_C \propto \sqrt{P_C}$ ). The absolute requirements on the optical depth and the control power, are however, quite moderate when compared to EIT and Raman based memories<sup>6</sup>, thereby, making the ATS protocol attractive over a wide range of platforms.

<sup>6</sup>We make this claim on the basis of our recent findings that are not reported in this thesis.

## Chapter 5

# Summary and Future Directions

In conclusion, we have built an optical setup which is expected to achieve efficient sub-Doppler cooling of  $^{39}\text{K}$  atoms by generating cooling and repumping laser frequencies that are blue-detuned on the D1-transition and operate near Raman resonance in a  $\Lambda$ -type configuration. This ‘Gray-Molasses’ cooling, as it is called, aided by the formation of dark or nearly-dark states, is expected to give temperatures that are lower by a factor of 4-5 than what one typically gets in the conventional red-detuned D2-line cooling of K [15, 17]. The enhanced cooling shall lead to an increased phase-space density which is crucial for future stages of evaporative-cooling for achieving quantum degeneracy.

With the optical setup built and characterized, the first imminent task is installing the K-source (K-ampoule) into the ultra-high-vacuum system. For this purpose, parts needed for holding the sealed glass-ampoule and breaking-off the seal into the vacuum chamber, have been machined (courtesy: Logan Cooke and Greg Popovich). The next task shall be to perform the laser-cooling operation, for which we have planned the following sequence: D2-line 2D-MOT (D1-beams ON)  $\rightarrow$  D2-line 3D-MOT (D1-beams ON)  $\rightarrow$  Compressed 3D-MOT (D1 beams ON)  $\rightarrow$  D2-molasses (optional)  $\rightarrow$  Pure D1-molasses. Temperature and optical density of the atomic cloud at the end of each stage in the above sequence would be characterized via fluorescence imaging, so that necessary optimization can be done.

To create a BEC of  $^{39}\text{K}$  atoms, the laser cooling operation shall be followed by loading the atoms into magnetic and optical dipole traps (in that order) where further cooling can be achieved via rf-induced evaporation. The optics for loading into the dipole trap is already in place and is being used to trap and cool  $^{87}\text{Rb}$  atoms [22]. However, unlike  $^{87}\text{Rb}$  or  $^{23}\text{Na}$ , direct evaporative cooling in  $^{39}\text{K}$  is difficult due to its un-favourable collisional properties and hence is done either by cooling it sympathetically using  $^{87}\text{Rb}$  [74] or by magnetically tuning the interatomic interactions via Feshbach resonance

[75]. In our quantum simulation setup, we would have the flexibility of trying both the approaches. Finally, the main goal of the K-project is performing experiments with ultracold K atoms in a Bose-Einstein-Condensate state: in particular, creating many-body-order in this coherent macroscopic state using spin-orbit-coupling (SOC) [76] (created via optical and microwave fields) as well as using magnetically tunable interactions [4] (created via Feshbach resonances). By working in a regime where there is a competition between the two kinds of many-body-order such that one degree of freedom dominates over other, we can study how different phases— magnetic, superfluid or novel types— emerge and evolve among the quantum particles [23].

In this thesis, we have also described a novel quantum memory scheme for storing (and retrieving on-demand) broadband pulses of light, based on coherent absorption of the optical pulse via dynamic ‘Autler-Townes’ absorption. We showed the numerical-modeling of the ‘ATS-protocol’ in a three-level  $\Lambda$ - type atomic system, however, this scheme can be applicable to other three-level systems as well such as Rydberg atoms (having a cascaded or ladder-type structure), opto-mechanical systems and superconducting circuits. We have shown that our memory protocol is inherently suited for storing wideband pulses ( $B_{\text{FWHM}} > \Gamma$ ) and the memory bandwidth scales linearly with optical depth<sup>1</sup>. Further, we also discussed strategies for getting maximum efficiency for a given bandwidth based on the optimal effective-optical-depth ( $\tilde{d}_{\text{Forward}} = 1.75$  and  $\tilde{d}_{\text{Backward}} \geq 3$ ) and control-pulse area ( $A_C(t) = 2\pi$ ). We showed that an overall efficiency at close to unity is possible at moderate optical depths and control power, which significantly relaxes the resource requirements compared to other established memory platforms such as EIT and Raman memories.

As an immediate follow-up on our ATS-protocol introduced in [5], we are currently working on the following: a detailed technical comparison among the EIT, Raman and ATS based memories in terms of the following metrics: efficiency and optical-depth scaling for a given signal bandwidth; efficiency and control-power scaling for a given bandwidth; memory-bandwidth scaling with respect to optical depth and control power for a given efficiency; and finally, robustness to decoherence as a function of storage time. Such comparisons shall be supported by theory as well as experiments. We are also working on highlighting the underlying physical processes that govern the storage mechanisms in each of the three memories: dispersion / slow

<sup>1</sup>We just touched upon the bandwidth vs optical-depth scaling, but it will be discussed in detail in the upcoming manuscripts.

light effect in EIT; adiabatic elimination of excited state in Raman; absorption or excitation of the polarization coherence in ATS (and photon-echo type memories) and studying if a smooth cross-over or transition exists among the memory regimes.

In [5], we have experimentally demonstrated the signal processing capability of the ATS scheme by temporal-pulse-compression / stretching and temporal-beam-splitting operations. We plan to extend this by implementing wavelength-conversion, that is, storing pulse at one frequency and retrieving on the other. The wavelength-conversion experiments shall pave the way for advanced quantum-transduction experiments, involving conversion between optical and microwave photons and hence can be readily used in quantum communication systems. Further, on the basis of our understanding of the EIT and ATS protocols, we are working on developing a hybrid storage protocol where we can efficiently store a long temporal pulse (smaller bandwidth) and retrieve a short pulse (larger bandwidth) with nearly the same efficiency. The hybrid approach seeks to take advantage of both EIT (that is inherently suitable for storing long temporal pulses) memory and ATS memory (which is inherently suited for storing short temporal pulses) and hence can achieve bandwidth-conversion. Our initial simulation results show a bandwidth conversion factor of up-to 1000 is possible. Further, we also plan to study the multimode storage capacity of ATS memory in relation to other photon-echo memories (AFC, CRIB) as well as adiabatic memories (EIT, Raman). Finally, as a means of integrating the quantum simulation and quantum memory experiments, we also aim to perform ATS-light storage experiments in a BEC of  $^{87}\text{Rb}$  atoms as it would offer a lot of advantage in terms of high optical-densities and increased coherence time.

# Bibliography

- [1] C. Chin et al. “Feshbach resonances in ultracold gases”. In: *Reviews of Modern Physics* 82.2 (2010), p. 1225.
- [2] I. Bloch, J. Dalibard, and S. Nascimbene. “Quantum simulations with ultracold quantum gases”. In: *Nature Physics* 8.4 (2012), p. 267.
- [3] W. S. Cole et al. “Bose-Hubbard models with synthetic spin-orbit coupling: Mott insulators, spin textures, and superfluidity”. In: *Physical review letters* 109.8 (2012), p. 085302.
- [4] C. D’Errico et al. “Feshbach resonances in ultracold 39K”. In: *New Journal of physics* 9.7 (2007), p. 223.
- [5] E. Saglamyurek et al. “Coherent storage and manipulation of broadband photons via dynamically controlled Autler-Townes splitting”. In: *arXiv preprint arXiv:1710.08902* (2017).
- [6] H. J. Metcalf and P. Van der Straten. *Laser cooling and trapping*. Springer Science & Business Media, 1999.
- [7] P. D. Lett et al. “Optical molasses”. In: *JOSA B* 6.11 (1989), pp. 2084–2107.
- [8] D. S. Weiss et al. “Optical molasses and multilevel atoms: experiment”. In: *JOSA B* 6.11 (1989), pp. 2072–2083.
- [9] C. Salomon et al. “Laser cooling of cesium atoms below 3  $\mu\text{K}$ ”. In: *EPL (Europhysics Letters)* 12.8 (1990), p. 683.
- [10] B Sheehy et al. “Magnetic-field-induced laser cooling below the Doppler limit”. In: *Physical review letters* 64.8 (1990), p. 858.
- [11] T. Tiecke. “Properties of potassium”. In: (2003).
- [12] M. E. Gehm. “Properties of  $6\text{Li}$ ”. In: (2013).
- [13] J. Dalibard and C. Cohen-Tannoudji. “Laser cooling below the Doppler limit by polarization gradients: simple theoretical models”. In: *JOSA B* 6.11 (1989), pp. 2023–2045.

- [14] A Aspect et al. "Laser cooling below the one-photon recoil energy by velocity-selective coherent population trapping". In: *Physical Review Letters* 61.7 (1988), p. 826.
- [15] G. Salomon et al. "Gray-molasses cooling of 39K to a high phase-space density". In: *EPL (Europhysics Letters)* 104.6 (2014), p. 63002.
- [16] D. R. Fernandes et al. "Sub-Doppler laser cooling of fermionic 40K atoms in three-dimensional gray optical molasses". In: *EPL (Europhysics Letters)* 100.6 (2012), p. 63001.
- [17] F. Sievers et al. "Simultaneous sub-Doppler laser cooling of fermionic Li 6 and K 40 on the D 1 line: Theory and experiment". In: *Physical Review A* 91.2 (2015), p. 023426.
- [18] C. J. Foot. *Atomic physics*. Vol. 7. Oxford University Press, 2005.
- [19] S. Chu et al. "Three-dimensional viscous confinement and cooling of atoms by resonance radiation pressure". In: *Physical Review Letters* 55.1 (1985), p. 48.
- [20] P. D. Lett et al. "Observation of atoms laser cooled below the Doppler limit". In: *Physical Review Letters* 61.2 (1988), p. 169.
- [21] A. Aspect et al. "Laser cooling below the one-photon recoil energy by velocity-selective coherent population trapping: theoretical analysis". In: *JOSA B* 6.11 (1989), pp. 2112–2124.
- [22] T. Hrushevskiy. "Quantum Gas Apparatus for Bose Einstein Condensate of 87 Rb". 2017.
- [23] L. J. LeBlanc. *Ultracold Gases for Quantum Simulation and Quantum Information*. 2013.
- [24] M Landini et al. "Sub-Doppler laser cooling of potassium atoms". In: *Physical review A* 84.4 (2011), p. 043432.
- [25] V. Gokhroo et al. "Sub-Doppler deep-cooled bosonic and fermionic isotopes of potassium in a compact 2D+–3D MOT set-up". In: *Journal of Physics B: Atomic, Molecular and Optical Physics* 44.11 (2011), p. 115307.
- [26] J. Sebastian et al. "Two-stage magneto-optical trapping and narrow-line cooling of Li 6 atoms to high phase-space density". In: *Physical Review A* 90.3 (2014), p. 033417.
- [27] D. McKay et al. "Low-temperature high-density magneto-optical trapping of potassium using the open 4 S → 5 P transition at 405 nm". In: *Physical Review A* 84.6 (2011), p. 063420.

- [28] A Burchianti et al. "Efficient all-optical production of large Li 6 quantum gases using D 1 gray-molasses cooling". In: *Physical Review A* 90.4 (2014), p. 043408.
- [29] A. T. Grier et al. " $\Lambda$ -enhanced sub-Doppler cooling of lithium atoms in D1 gray molasses". In: *Physical Review A* 87.6 (2013), p. 063411.
- [30] D. Nath et al. "Quantum-interference-enhanced deep sub-Doppler cooling of 39 K atoms in gray molasses". In: *Physical Review A* 88.5 (2013), p. 053407.
- [31] D. W. Preston. "Doppler-free saturated absorption: Laser spectroscopy". In: *American Journal of Physics* 64.11 (1996), pp. 1432–1436.
- [32] R. S. Williamson. "Magneto-optical trapping of potassium isotopes". PhD thesis. University of Wisconsin–Madison, 1997.
- [33] M Weel and A Kumarakrishnan. "Laser-frequency stabilization using a lock-in amplifier". In: *Canadian journal of physics* 80.12 (2002), pp. 1449–1458.
- [34] K. H. Ang, G. Chong, and Y. Li. "PID control system analysis, design, and technology". In: *IEEE transactions on control systems technology* 13.4 (2005), pp. 559–576.
- [35] T. Photonics. "DLC PRO, Digital Laser Controller Manual". In: (2015).
- [36] E. Donley et al. "Double-pass acousto-optic modulator system". In: *Review of Scientific Instruments* 76.6 (2005), p. 063112.
- [37] D. Inc. "SPI Reference Digilent INC". In: (). URL: <https://reference.digilentinc.com/learn/fundamentals/communication-protocols/spi/start>.
- [38] P. P. Chu. *FPGA prototyping by VHDL examples: Xilinx Spartan-3 version*. John Wiley & Sons, 2011.
- [39] A. I. Lvovsky, B. C. Sanders, and W. Tittel. "Optical quantum memory". In: *Nature photonics* 3.12 (2009), p. 706.
- [40] L.-M. Duan et al. "Long-distance quantum communication with atomic ensembles and linear optics". In: *Nature* 414.6862 (2001), p. 413.
- [41] N. Sangouard et al. "Quantum repeaters based on atomic ensembles and linear optics". In: *Reviews of Modern Physics* 83.1 (2011), p. 33.
- [42] Y.-A. Chen et al. "Memory-built-in quantum teleportation with photonic and atomic qubits". In: *Nature Physics* 4.2 (2008), p. 103.

- [43] H. P. Specht et al. "A single-atom quantum memory". In: *Nature* 473.7346 (2011), p. 190.
- [44] K. Hammerer, A. S. Sørensen, and E. S. Polzik. "Quantum interface between light and atomic ensembles". In: *Rev. Mod. Phys.* 82 (2 2010), pp. 1041–1093.
- [45] B. Julsgaard et al. "Experimental demonstration of quantum memory for light". In: *Nature* 432.7016 (2004), p. 482.
- [46] D. F. Phillips et al. "Storage of Light in Atomic Vapor". In: *Phys. Rev. Lett.* 86 (5 2001), pp. 783–786.
- [47] D. Matsukevich and A. Kuzmich. "Quantum state transfer between matter and light". In: *Science* 306.5696 (2004), pp. 663–666.
- [48] L. V. Hau et al. "Light speed reduction to 17 metres per second in an ultracold atomic gas". In: *Nature* 397.6720 (1999), p. 594.
- [49] M. Afzelius et al. "Photon-echo quantum memory in solid state systems". In: *Laser & Photonics Reviews* 4.2 (2010), pp. 244–267.
- [50] K.-J. Boller, A. Imamoglu, and S. E. Harris. "Observation of electromagnetically induced transparency". In: *Physical Review Letters* 66.20 (1991), p. 2593.
- [51] M. Fleischhauer and M. D. Lukin. "Quantum memory for photons: Dark-state polaritons". In: *Physical Review A* 65.2 (2002), p. 022314.
- [52] I. Novikova, R. L. Walsworth, and Y. Xiao. "Electromagnetically induced transparency-based slow and stored light in warm atoms". In: *Laser & Photonics Reviews* 6.3 (2012), pp. 333–353.
- [53] A. Kozhekin, K. Mølmer, and E. Polzik. "Quantum memory for light". In: *Physical Review A* 62.3 (2000), p. 033809.
- [54] J. Nunn et al. "Mapping broadband single-photon wave packets into an atomic memory". In: *Physical Review A* 75.1 (2007), p. 011401.
- [55] E. Saglamyurek. "Broadband Waveguide Quantum Memory for Quantum Communication". PhD thesis. University of Calgary, 2013.
- [56] I. D. Abella, N. A. Kurnit, and S. R. Hartmann. "Photon Echoes". In: *Phys. Rev.* 141 (1 1966), pp. 391–406.
- [57] M. Nilsson and S. Kröll. "Solid state quantum memory using complete absorption and re-emission of photons by tailored and externally controlled inhomogeneous absorption profiles". In: *Optics communications* 247.4-6 (2005), pp. 393–403.

- [58] A. Alexander et al. "Photon echoes produced by switching electric fields". In: *Physical review letters* 96.4 (2006), p. 043602.
- [59] G. Hétet et al. "Multimodal properties and dynamics of gradient echo quantum memory". In: *Physical review letters* 101.20 (2008), p. 203601.
- [60] G Hétet et al. "Photon echoes generated by reversing magnetic field gradients in a rubidium vapor". In: *Optics letters* 33.20 (2008), pp. 2323–2325.
- [61] M. Afzelius et al. "Demonstration of atomic frequency comb memory for light with spin-wave storage". In: *Physical review letters* 104.4 (2010), p. 040503.
- [62] M. Afzelius et al. "Multimode quantum memory based on atomic frequency combs". In: *Physical Review A* 79.5 (2009), p. 052329.
- [63] N. Sinclair et al. "Spectral multiplexing for scalable quantum photonics using an atomic frequency comb quantum memory and feed-forward control". In: *Physical review letters* 113.5 (2014), p. 053603.
- [64] S. H. Autler and C. H. Townes. "Stark Effect in Rapidly Varying Fields". In: *Phys. Rev.* 100 (2 1955), pp. 703–722.
- [65] A Imamoglu and S. E. Harris. "Lasers without inversion: interference of dressed lifetime-broadened states". In: *Optics letters* 14.24 (1989), pp. 1344–1346.
- [66] Y.-q. Li and M. Xiao. "Observation of quantum interference between dressed states in an electromagnetically induced transparency". In: *Physical Review A* 51.6 (1995), p. 4959.
- [67] L. Giner et al. "Experimental investigation of the transition between Autler-Townes splitting and electromagnetically-induced-transparency models". In: *Phys. Rev. A* 87 (1 2013), p. 013823.
- [68] X. Lu et al. "Transition from Autler–Townes splitting to electromagnetically induced transparency based on the dynamics of decaying dressed states". In: *Journal of Physics B: Atomic, Molecular and Optical Physics* 48.5 (2015), p. 055003.
- [69] P. M. Anisimov, J. P. Dowling, and B. C. Sanders. "Objectively discerning Autler-Townes splitting from electromagnetically induced transparency". In: *Physical review letters* 107.16 (2011), p. 163604.
- [70] A. V. Gorshkov et al. "Photon storage in  $\Lambda$ -type optically dense atomic media. II. Free-space model". In: *Physical Review A* 76.3 (2007), p. 033805.

- 
- [71] W.-T. Liao, C. H. Keitel, and A. Pálffy. “All-electromagnetic control of broadband quantum excitations using gradient photon echoes”. In: *Physical review letters* 113.12 (2014), p. 123602.
- [72] P. Michelberger. “Room temperature caesium quantum memory for quantum information applications”. PhD thesis. Balliol College, Oxford, 2015.
- [73] W.-T. Liao, C. H. Keitel, and A. Pálffy. “All-Electromagnetic Control of Broadband Quantum Excitations Using Gradient Photon Echoes”. In: *Phys. Rev. Lett.* 113 (12 2014), p. 123602.
- [74] L De Sarlo et al. “Collisional properties of sympathetically cooled K 39”. In: *Physical Review A* 75.2 (2007), p. 022715.
- [75] M. Landini et al. “Direct evaporative cooling of 39 K atoms to Bose-Einstein condensation”. In: *Physical Review A* 86.3 (2012), p. 033421.
- [76] V. Galitski and I. B. Spielman. “Spin–orbit coupling in quantum gases”. In: *Nature* 494.7435 (2013), p. 49.